

**HYPERSPECTRAL IMAGE PROCESSING OF EO-1 HYPERION DATA
FOR LITHOLOGICAL AND MINERALOGICAL MAPPING**

**A THESIS SUBMITTED TO
THE GRADUTAE SCHOOL OF NATURAL AND APPLIED SCIENCES
OF
MIDDLE EAST TECHNICAL UNIVERSITY**

BY

BEKİR TANER SAN

**IN PARTIAL FULFILLMENT OF THE REQUIREMENTS
FOR
THE DEGREE OF DOCTOR OF PHILOSOPHY
IN
GEOLOGICAL ENGINEERING**

SEPTEMBER 2008

Approval of the thesis:

**HYPERSPECTRAL IMAGE PROCESSING OF EO-1 HYPERION DATA
FOR LITHOLOGICAL AND MINERALOGICAL MAPPING**

submitted by **BEKİR TANER SAN** in partial fulfillment of the requirements for
the degree of **Doctor of Philosophy in Geological Engineering**
Department, Middle East Technical University by,

Prof. Dr. Canan Özgen
Dean, Graduate School of **Natural and Applied Sciences** _____

Prof. Dr. Dr. Vedat Doyuran
Head of Department, **Geological Engineering** _____

Assoc. Prof. Dr. M. Lütfi Süzen
Supervisor, **Geological Engineering Dept., METU** _____

Examining Committee Members:

Prof. Dr. Can AYDAY
Satellite and Space Res. Sci. Ins., Anadolu University _____

Assoc. Prof. Dr. M. Lütfi Süzen
Geological Engineering Dept., METU _____

Prof. Dr. Vedat Toprak,
Geological Engineering Dept., METU _____

Assoc. Prof. Dr. Nuretdin Kaymakçı
Geological Engineering Dept., METU _____

Dr. Arda Arcasoy
Arcasoy Consulting and Engineering Co. _____

Date: 05. 09. 2008

I hereby declare that all information in this document has been obtained and presented in accordance with academic rules and ethical conduct. I also declare that, as required by these rules and conduct, I have fully cited and referenced all material and results that are not original to this work.

Name, Last name: Bekir Taner SAN

Signature :

ABSTRACT

HYPERSPECTRAL IMAGE PROCESSING OF EO-1 HYPERION DATA FOR LITHOLOGICAL AND MINERALOGICAL MAPPING

SAN, Bekir Taner

Ph.D., Department of Geological Engineering
Supervisor: Assoc. Prof. Dr. Mehmet Lütfi SÜZEN

September 2008, 142 pages

Hyperspectral data is a powerful tool for mineral explorations and lithological discriminations. EO1-Hyperion is a space borne hyperspectral system for hyperspectral imaging which is capable of 220 spectral image channels within the range of 400 to 2500 nm wavelengths. It has advantages over airborne systems such as data cost and coverage area. Although it has many advantages, much more uncertainty exists in application period, of which this uncertainty does exist in all processing stages starting from the data preparation to the end of analysis stages.

The aim of this thesis is to state the potential use of Hyperion data for lithological and mineralogical discriminations to further develop new hyperspectral image processing approach, and to improve existing preprocessing method in literature.

The proposed algorithm is mainly based on atmospheric corrections and cross track illumination correction of Hyperion data. In order to achieve this, two test sites were selected. Site 1 located on the Central Anatolia, (Ekecek test site) is used for lithological discrimination and Site 2 located on West Anatolia (Biga test site) is used for mineralogical discrimination. The obtained results were compared and assessed with the field verifications, spectral measurements and existing spectral libraries.

In the end of the study it is found that when proposed approach is followed hyperspectral data is proven to be a useful tool for mineralogical discrimination in mono minerallic outcrops and valuable for lithological mapping in relatively homogenous un-covered outcrops.

Keywords: Hyperspectral, EO-1 Hyperion, atmospheric correction, smile effect, cross track illumination, geologic remote sensing

ÖZ

LİTOLOJİK VE MİNERALOJİK HARİTALAMA İÇİN EO-1 HYPERION VERİSİNİN HİPERSPEKTRALGÖRÜNTÜ İŞLEMESİ

SAN, Bekir Taner

Doktora, Jeoloji Mühendisliği Bölümü
Tez Yöneticisi: Doç. Dr. Mehmet Lütfi SÜZEN

Eylül 2008, 142 sayfa

Maden aramacılığı ve litolojik ayırtlama için Hiperspektral veri güçlü bir araçtır. EO1-Hyperion 400 - 2500 nm dalga boyu aralığında 220 spektral görüntü bandına sahip, uzaydan hiperspektral görüntüleme sistemidir. Havadan hiperspektral görüntüleme sistemlerine göre veri fiyatı ve kapsama alanı gibi avantajlara sahiptir. Her ne kadar bir çok avantajı olsa da, uygulama periyodunda bir çok belirsizliği bulunur ki bu belirsizlik veri hazırlamadan başlayıp analiz aşamasına kadar tüm işlem aşamalarında mevcuttur.

Bu tezin amacı litolojik ve mineralojik ayırt etme için Hyperion verisinin potansiyel kullanımını belirlemek için yeni hiperspektral görüntü işleme yaklaşımı ve literatürde mevcut ön işlem metotlarını geliştirmektir.

Önerilen algoritma esasen Hyperion verisinin atmosferik düzeltmesi ve uçuşa dik yönlü aydınlanma düzeltmesi temeline dayanır. Bunu gerçekleştirebilmek için, iki test alanı seçilmiştir. Orta Anadolu'da (Ekecek test alanı) bulunan Alan 1 litolojik ayırım için kullanılmış, Batı Anadolu'da (Biga test alanı) bulunan Alan 2 mineralojik ayırtlama için kullanılmıştır. Elde edilen sonuçlar arazi doğrulamaları, spektral ölçümler ve mevcut spektral kütüphaneler ile karşılaştırılmış ve değerlendirilmiştir.

Çalışmanın sonunda önerilen yaklaşım izlendiğinde, hiperspektral verinin mono mineralik mostralarda mineralojik ayırtlama için kullanışlı bir araç olduğu ve görelî homojen açık mostralarda litolojik haritalama için çok değerli girdi olduğu ispatlanarak bulunmuştur.

Anahtar Kelimeler: Hiperspektral, EO-1 Hyperion, atmosferik düzeltme, gülümseme etkisi, uçuşa dik aydınlanma, jeolojik uzaktan algılama

To My Wife

ACKNOWLEDGEMENTS

I would like to thank Assoc. Prof. Dr. M. Lutfi SÜZEN for his continuous support, insight, and guidance during my study, and his caring to my thesis writing process.

Thanks to Prof. Dr. Can AYDAY, Prof. Dr. Vedat TOPRAK, Assoc. Prof. Dr. Nuretdin KAYMAKCI and Dr. Arda ARCASOY for their suggestions, evaluations and assistance in technical areas to improvement of the study.

I am indebted to my colleagues Murat KORUYUCU, Serkan OZTAN, Okan ZIMITOGLU, Ahmet TÜRKECAN, Dr. Engin SUMER, Dr. Bora GURCAY, Kerem AVCI, Hakan NEFESLİOĞLU, Gonca GÜRLER, and Sultan PAKER for their valuable supports.

I would like to thank to General Directorate of Mineral Research and Exploration for giving the opportunity to do research and I would also thank to my manager Dr. Erol TİMUR from MTA for their patience throughout my study.

I cordially would like to express my sincere gratitude my family for their affection and moral support. Finally, I would like to show my very special thanks to my wife Dilek KOC SAN for her continuous motivation, technical supports, patience and endless trust during my doctorate program.

TABLE OF CONTENTS

ABSTRACT	iv
ÖZ.....	vi
ACKNOWLEDGEMENTS	ix
TABLE OF CONTENTS	x
LIST OF TABLES.....	xiv
LIST OF FIGURES	xv
CHAPTER	
1. INTRODUCTION.....	1
1.1. Purpose and Scope	1
1.2. Data	3
1.3. Test Sites.....	4
1.4. Used Software in the Study	5
1.5. The Chapters in the Thesis.....	5
2. BACKGROUND STUDY.....	7
2.1. Principles and Definitions.....	7
2.2. History of Imaging Spectrometer Systems.....	11
2.3. EO-1 Hyperion Data.....	12
2.4. Pre-processing of Hyperspectral Data	13
2.4.1. Absolute Atmospheric Correction Techniques	14
2.4.1.1. Atmospheric CORrection Now (ACORN).....	15
2.4.1.2. ATmospheric CORrection (ATCOR2 and 3)	16
2.4.1.3. Fast Line-of-sight Atmospheric Analysis of Spectral Hypercubes (FLAASH).....	16
2.4.2. Relative Atmospheric Correction Techniques.....	17
2.5. Techniques for Mineral Mapping.....	20

2.5.1. Conventional Methods for Spectral Analysis	21
2.5.1.1. Color Composites	21
2.5.1.2. Band Ratios	21
2.5.1.3. Statistical Transforms	22
2.5.1.3.1. Principle Component Analysis.....	22
2.5.1.3.2. Minimum Noise Fraction.....	23
2.5.1.3.3. Selective Principle Component Analysis	23
2.5.2. Feature Mapping and the Identification of Minerals.....	24
2.5.2.1. Binary Encoding.....	26
2.5.2.2. Waveform Characterization	26
2.5.2.3. Spectral Feature Fitting.....	28
2.5.2.4. Spectral Angle Mapping.....	29
2.5.2.5. Spectral Un-mixing	30
2.5.2.6. Constrained Energy Minimization	32
2.5.2.7. Classification.....	33
2.5.2.8. Cross Correlogram Spectral Matching.....	34
3. DATA PREPARATION	36
3.1. Elimination of Un-calibrated Bands and Spatial Subset.....	38
3.2. Geometric Correction.....	39
3.3. Masking Operations.....	42
4. ATMOSPHERIC CORRECTION	44
4.1. Atmospheric CORrection Now (ACORN).....	45
4.2. ATmospheric CORrection (ATCOR2 and 3)	45
4.3. Fast Line-of-sight Atmospheric Analysis of Spectral Hypercubes (FLAASH)	46
4.4. Water Absorption Bands Removal.....	46

4.5. The Comparison of Atmospheric Correction Techniques.....	48
4.5.1. The Cross Correlations between Image Data and Field Spectra Data for Each Atmospheric Correction Algorithm ...	49
4.5.2. The Comparison between Image Data and Field Spectra Data for Each Atmospheric Correction Algorithms Using Absorption Wavelength.....	58
4.6. Choosing the Optimum Atmospheric Correction Technique	60
4.7. Bad Band Removal.....	61
5. CROSS TRACK ILLUMINATION CORRECTION.....	62
5.1. Minimum Noise Fraction (MNF) Transformation	62
5.2. The Cross Track Illumination Correction (CTIC) / Spectral Smile Correction	66
5.3. The Cross Track Illumination Effect on SAM Rule Images	71
6. RESULTS AND DISCUSSIONS.....	76
6.1. CTIC Effect of Hyperspectral Thematic Mapping.....	76
6.2. Hyperspectral Classification of Ekecek Image	79
6.3. Spectral Angle Mapper (SAM) Classification of Ekecek Image.....	80
6.4. Hyperspectral Classification of Biga Image.....	86
6.5. Spectral Angle Mapper (SAM) Classification of Biga Image	87
6.6. Cross Correlations and Performance Evaluation	90
6.7. Spectral Mixture Analysis (SMA).....	93
6.8. Discussion	103
6. CONCLUSIONS AND RECOMMENDATIONS	106
REFERENCES.....	108
APPENDICES	
APPENDIX A.....	120
APPENDIX B.....	121
APPENDIX C.....	122

APPENDIX D.....	123
APPENDIX E.....	127
APPENDIX F.....	134
VITA	137

LIST OF TABLES

TABLE

1.1. Used EO-1 Hyperion Data in the study	4
4.1. The correlation coefficient of samples for full wavelength spectrum and regions of spectrum. The maximum values are underlined	56
4.2. The main absorption wavelength of the reference spectra and the comparison of the corresponding region of atmospherically corrected image spectra. Blue shows all the correction techniques are correctly detected and the red shows none of the atmospheric correction techniques detected the absorption wavelength.....	59
5.1. Eigen values of MNF transformation (no CTIC applied).....	65
5.2. Eigen values of MNF transformation (third order CTIC) for Ekecek Image data	71
6.1. Spectral un-mixing results showing the mineral ratios of the corresponding samples.....	95
6.2. Spectral un-mixing results show the mineral ratios of the corresponding samples using minerals from XRD results.....	96
F.1. Used Minerals Spectra from USGS Spectral Library	134

LIST OF FIGURES

FIGURES

1.1. Locations of test sites.....	4
2.1. Gaussian profile with a full width at half maximum (FWHM)	9
2.2. Atmospheric transmittance, mid-infrared is compared to scaled grey-body spectra. Most of the absorption is due to water. Carbon dioxide has a strong 15- μ m band, and the dotted line shows the increased absorption due to doubling CO ₂ . Also shown is the black-body emission at 288 K and the grey-body emission from water and a sandstone scaled to fit on this transmittance scale. The water and sandstone curves were computed from reflectance data using: 1 - reflectance times a black-body at 288 Kelvin. (Clark, 1999)	11
2.3. Continuum and continuum removal spectra of the kaolinite (Van der Meer, 2004).....	25
2.4. Absorption parameters; wavelength, absorption depth, absorption width, absorption symmetry. (Van der Meer, 2004).....	28
2.5. Reference and test spectrum of a two band image. The same material is represented by vectors connecting the origin (Kruse, et. al., 1993.b)	30
2.6. Reflectance spectra of alunite, jarosite and mixtures of them. Two different mixture which are aerial and intimate are shown (Clark, 1999)	32
3.1. The flow chart of proposed approach for Hyperion image data processing	37
3.2. EO1-Hyperion Level 1 image data and its calibrated channels.....	38

3.3. The locations of collected ground control points on the raw Hyperion image for Ekecek test site.....	41
3.4. NDVI image (a) and Area of interest (b) is used for analysis in the study area of Ekecek	43
4.1. Spectral curve of one pixel sample on raw image (a), ACORN corrected image (b), ATCOR2 corrected image (c) ATCOR3 corrected image (d), and FLAASH corrected image (e). The wavelength region A (1296 nm to 1467 nm) and B (1740 nm to 1992 nm) are eliminated during the analysis stage due to water vapor absorption	48
4.2. Spectral samples collected from the field and Hyperion Image data for Ekecek test site.....	51
4.3. Spectral curve of the samples A1, A2, A3, A4, A6 and A7 (Black: reference spectra, blue: raw image spectra, green: ACORN corrected image spectra, orange: ATCOR2 corrected image spectra, violet: ATCOR3 corrected image spectra, red: FLAASH corrected image spectra)	53
4.4. Spectral curve of the samples A8, A9, B2, B5, B10 and B12 (Black: reference spectra, blue: raw image spectra, green: ACORN corrected image spectra, orange: ATCOR2 corrected image spectra, violet: ATCOR3 corrected image spectra, red: FLAASH corrected image spectra)	54
4.5. Spectral curve of the samples B13, B17, and B20 (Black: reference spectra, blue: raw image spectra, green: ACORN corrected image spectra, orange: ATCOR2 corrected image spectra, violet: ATCOR3 corrected image spectra, red: FLAASH corrected image spectra)	55
4.6. Correlations of each sample between reference spectra and atmospherically corrected images for full wavelength range.....	57
5.1. MNF eigen value bands of The ACORN corrected Ekecek image	64

5.2. Graphical representation of the eigen values versus eigen numbers for the ACORN corrected image for Ekecek test site. A region shows high eigen indicating mainly image data and B region shows low eigen values indicating possible noise.....	64
5.3. ACORN corrected image for Ekecek test site; the first MNF component (a), the second MNF component (b), the third MNF component (c), and the forth MNF component (d)	67
5.4. Cross-Track Illumination of MNF which transformed from whole image channels	68
5.5. The first MNF component with varying degrees of CTIC correction.....	69
5.6. Cross-Track Illumination (CTI) of MNF images	70
5.7. RGB color composite representation of MNF bands of no CTIC applied (a), first order CTIC applied (b), second order CTIC applied (c) for Biga image	72
5.8. Negative rule images of field samples (1 - 4) are generated from no CTIC applied and second order CTIC applied images, and the differences of them with the location of samples.....	73
5.9. Negative rule images of field samples (5 - 8) are generated from no CTIC applied and second order CTIC applied images, and the differences of them with the location of samples.....	74
6.1. Band correlation image generated from the experimental data of AVIRIS image, (Chen and Wang, 2007). The horizontal and the vertical axes show the bands of AVIRIS data	77
6.2. Unsupervised classification results with 10 classes; using first 20 MNF bands (a), using first 20 MNF bands applied first additive CTIC (b), using first 20 MNF bands applied second additive CTIC (c), and using first 20 MNF bands applied third order CTIC	79
6.3. 1: 100 000 scaled simplified Geological map (Atabey, (1989) and Kara, (1991)) and image boundary of Hyperion data.....	81

6.4. RGB color composite representation of negative SAM rule images for Gabbro, Granite, and Granodiorite from John Hopkins University (JHU) spectral library and photo on the same location from the field study. A and B shows the location and appearance of altered granite and granite, respectively. C is taken from Ekecek Mountain.....	83
6.5. RGB color composite representation of negative SAM rule images for olivine, kaolinite, and orthoclase from USGS spectral library. The rule image of the olivine endmember is assigned to red channel. Kaolinite endmember is directly related with the altered granite (A) and rule images of the sample is assigned to green channel. Orthoclase endmember is also related with the granite body and it is assigned to blue channel	84
6.6. RGB color composite representation of SAM rule images for sample B13, sample A03, and sample B20 from Field Samples Spectra. The rule image of the sample B13 endmember is assigned to red channel. The sample A03 endmember is taken from the altered granite (A) and rule images of the sample is assigned to green channel. sample B20 endmember is also related with the granite body and it is assigned to blue channel	86
6.7. False color representation of ASTER and Hyperion images of Çan area.....	87
6.8. Collected samples on true color representation of Hyperion image	89
6.9. RGB color composite of rule images derived from the USGS spectral library. Three different color composite images are (a) RGB: Hematite-Illite-Halloysite, (b) RGB: Hematite-Kaolinite-Halloysite, and (c) RGB: Hematite-Kaolinite-Quartz	89
6.10. Cross correlation coefficients (r) between before CTIC and after CTIC for different rule images of endmembers	91

6.11. Slope values (a) between before CTIC and after CTIC for different rule images of endmembers.....	91
6.12. VAF values of endmembers between before CTIC and after CTIC for different rule images of endmembers	92
6.13. Spectral Mixture Analysis for sample 1 from Biga test site.....	95
6.14. Field sample spectra and their matched corresponding mixtures. Sample 1 and mixture 1 to sample 8 and mixture 8 are shown from (a) to (h).	97
6.15. Field sample spectra and their corresponding mixtures using minerals from XRD result. Sample 1 and mixture 1 to sample 8 and mixture 8 are shown from (a) to (h).....	99
6.16. Correlations between SAM rule images of Field Spectra (x axis) and SAM rule images of corresponding mixture spectra (y axis). Figure (a) to (h) stands for mixture 1 to 8. (r stands for the correlation coefficient).....	100
6.17. Correlations between SAM rule images of Field Spectra (x axis) and SAM rule images of corresponding mixture spectra (y axis) from XRD analysis results. Figure (a) to (h) stands for mixture 1 to 8. (r stands for the correlation coefficient).....	102
A.1. ACORN software interface and input parameters for Ekecek Study Area.....	120
B.1. ATCOR2 software interface and input parameters for Ekecek Study Area.....	121
C.1. FLAASH software interface and input parameters for Ekecek Study Area.....	122
C.2. Acquired header information from Hyperion data.....	122
D.1. Samples A and B are collected from Ekecek and Biga test sites, respectively	123
E.1. Cross correlation between rule image of no CTIC and rule image of second order CTIC applied data for Halloysite mineral form USGS spectral library	127

E.2. Cross correlation between rule image of no CTIC and rule image of second order CTIC applied data for Hematite mineral form USGS spectral library	128
E.3. Cross correlation between rule image of no CTIC and rule image of second order CTIC applied data for Illite mineral form USGS spectral library	129
E.4. Cross correlation between rule image of no CTIC and rule image of second order CTIC applied data for Kaolinite + Smectite mineral form USGS spectral library.....	130
E.5. Cross correlation between rule image of no CTIC and rule image of second order CTIC applied data for Kaolinite mineral form USGS spectral library	131
E.6. Cross correlation between rule image of no CTIC and rule image of second order CTIC applied data for Opal mineral form USGS spectral library	132
E.7. Cross correlation between rule image of no CTIC and rule image of second order CTIC applied data for Quartz mineral form USGS spectral library	133

CHAPTER 1

INTRODUCTION

1. 1. Purpose and Scope

Human being can only see 400 to 700 nm wavelength region of the electromagnetic spectrum (EMS), the visible range which is also called light. The longer and the shorter wavelengths can only be sensed by humans by the help of technological sensors. The basis of passive remote sensing is the interaction of EMS with the target, of which in geological remote sensing it is primarily the reflection of incident radiation by different lithologies or by minerals which constitute them. Passive remote sensing is based on interaction of EMS with different materials such as minerals. Using these interaction differences, lithological or mineralogical discrimination can be done. In other words, each mineral or surface composition has their own spectral reflectance patterns which are called spectral signatures. In the early years of remote sensing, images were acquired only in a limited number of channels with broader band widths, resulting in very discrete few channels especially in visible and near-infrared wavelength regions. The locations of these bands were chosen according to the project mission, economical and physical constraints. Even the successful Landsat TM sensor systems, designed for earth observation have only 7 channels, 3 of them located in visible region, 3 in short wave infrared (SWIR) region and 1 of them in thermal infrared region. The presence of SWIR bands enabled differentiation

and detection of clay mineral groups. With further developments in remote sensing technology, ASTER sensor systems are developed and successfully deployed to the orbit with the improvement of the sensor technologies in year 2000. ASTER having 14 spectral bands has more and narrower spectral channels that enabled detection and mapping of individual clay minerals (such as alunite and kaolinite) rather than mineral groups.

Although ASTER images have largely improved the mapping and discrimination of individual mineral types, however, this success is limited to only certain minerals and mineral groups.

Hyperspectral imaging can be divided into categories as airborne and space borne according to their platforms. Although airborne systems have many advantages over the space borne platforms, like their flexible flight paths, higher spatial resolution and are less effected from atmosphere. Despite their advantages their footprints on earth are negligibly small, as all of them are acquired for special projects with great acquisition costs. Nevertheless, the publicized space borne hyperspectral sensors are cheap alternatives for airborne systems, whereas the space borne sensors suffer from atmospheric effects.

EO1-Hyperion is a space borne hyperspectral system for hyperspectral imaging which is capable of 220 spectral image channels having 30 m spatial resolution within the range of 400 to 2500 nm wavelengths. EO1-Hyperion data needs some pre-processing steps to polish the data before the main analysis stage. As expected, atmospheric correction is vital for hyperspectral image processing, whereas, there are no any perfect and standard correction technique developed up to now. Furthermore, not only atmospheric effects but also smile effect is directly related with the quality of the results of EO1-Hyperion data.

Most of the theoretical and experimental works of hyperspectral image processing that had been published are carried out in a very well mapped, near vegetation sterile environment with mappable size of mono mineralic outcrops at Nevada, USA, and Australia. However in the operational cases it is nearly impossible to maintain all these test site specifications.

The purpose of this study is to understand and experiment the mapping capabilities of space borne hyperspectral sensors while further developing necessary image processing techniques and generating a flowchart for lithological and mineralogical mapping. In order to fulfill this aim, the hyperspectral space borne sensor system EO-1 Hyperion coupled with ultraspectral ASD field spectrometer were used to experiment lithological and mineral mapping on two different test sites in Turkey during the study.

1. 2. Data

Data used in the study are categorized into three groups which are hyperspectral data (two EO-1 Hyperion imageries), the ASD field spectrometer measurements of 23 samples collected from the field, and ancillary data containing various geological maps prepared by General Directorate of Mineral Research and Exploration (MTA) and topographical base maps prepared by General Command of Mapping.

Hyperion has total 242 spectral channels having 30 m spatial resolution within 400 to 2500 nm wavelength region. The near infrared region and short wave infrared region contain 35 and 172 bands, respectively (Beck, 2003). During the study, archive Hyperion image data sets were used for digital image processing and analysis. Table 1. 1. shows center coordinates and acquisition dates of the Hyperion data.

Table 1. 1. Used EO-1 Hyperion Data in the study.

Image Scene ID	Area Tag	Scene Center		Acquisition Date
		Latitude	Longitude	
EO1H1760332002321110PY	Ekecek	38.719	34.115	November 17, 2002
EO1H1810322002324110PZ	Biga	40.034	27.004	November 20, 2002

1. 3. Test Sites

The study is carried out for two different test sites with differing geological and environmental conditions. First one is located on the Kırşehir and Aksaray Provinces, Central Anatolia, whereas the other one is located at Çan county of Çanakkale province, North West Anatolia. In the first test area, which is called called Ekecek Area (1) here forth, has extensive granite and gabbro outcrops which were treated as targets for lithological discriminations with very sparse vegetation cover. The other area is called Biga Area (2) which contains the largest kaolinite open pit mine of Turkey hence the target is primarily kaolinite mineral in Çan area while the rest of the image is densely covered with vegetation (Figure 1. 1).

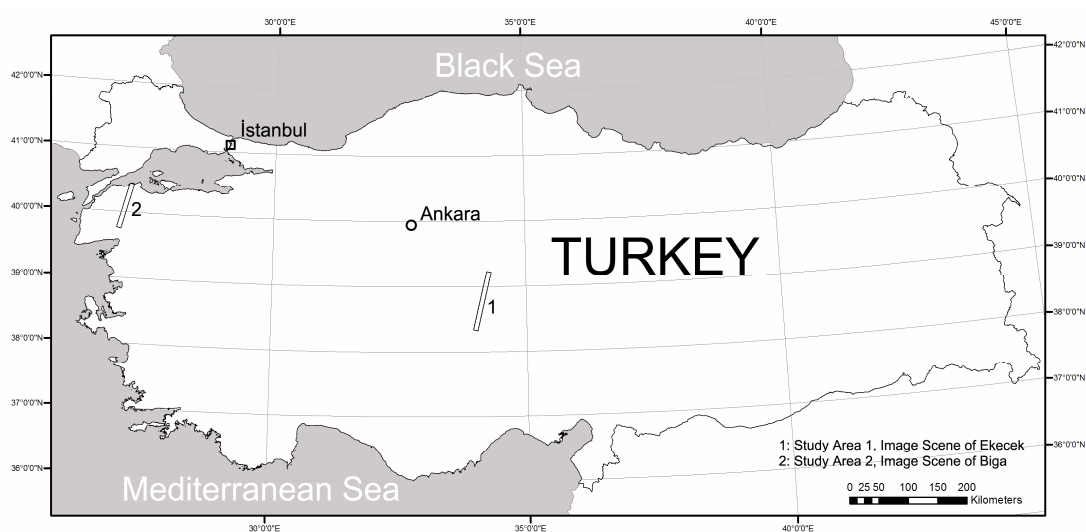


Figure 1.1. Locations of test sites.

1.4. Used Software in the Study

Four main groups of software were used in the study. The first group is related about image processing and analysis software that are ENVI (version 4.4), PCI Geomatica (version 10.0), and Erdas Imagine (version 8.5). The second group of software which are ACORN (Atmospheric CORrection Now), ATCOR 2 – 3 (ATmospheric CORrection), and FLAASH (Fast Line-of-sight Atmospheric Analysis of Spectral Hypercubes) are directly related about atmospheric correction of the hyperspectral data. The third group of software is used for spectral measurements, spectral filtering, spectral analysis and spectral un-mixing. These are listed as ASD FieldSpecPro, Adjust ASD, ASD ViewSpecPro (version 3.03), and SPECMIN – PRO (version 3.1). The last group is composed auxiliary / supplementary software which are TextPad for reading and editing header information of image data and preparing input files of atmospheric correction modules and MS Excel for normalizing spectral curves of targets and MS Word to document this study.

The most of the image processing and analyses were carried out using ENVI. Erdas Imagine was used for orthorectification process. ATCOR 2 - 3 and FLAASH are the modules of PCI Geomatica and ENVI, respectively. ACORN atmospheric correction module is the only stand-alone atmospheric correction software used in this study.

1. 5. The Chapters in the Thesis

This thesis consists of seven chapters. In the first chapter, introduction is given with the used data, test sites and software. Chapter 2 comprises brief information about principles and application techniques for hyperspectral image pre-processing and processing with the related literature review.

The applied methodology with the flowchart is given in chapter 3 which mainly contains data preparation and some ordinary pre-processing steps. Un-calibrated bands elimination, geometric correction, and masking operations are explained in detail.

Chapter 4 mainly contains the application and the comparison of atmospheric correction techniques which are Atmospheric CORrection Now (ACORN), Atmospheric CORrection Now (ACORN), and Fast Line-of-sight Atmospheric Analysis of Spectral Hypercubes (FLAASH). The cross correlation and the comparison using absorption wavelengths of them are also given in this chapter.

In chapter 5, Minimum Noise Fraction (MNF) transformation and Cross Track Illumination Correction which is proposed for EO-1 Hyperion image processing are given with their application results.

In chapter 6, the obtained results are presented for the hyperspectral classification of test sites and spectral mixture analyses are given. These results are discussed in detail using graphical interpretations and correlations. Finally, discussion part is provided concerning all of the issues throughout the study.

Finally, conclusions and recommendations of the study are given in chapter 7.

CHAPTER 2

BACKGROUND STUDIES

In this chapter, principles and methods of imaging spectroscopy are presented. Then, information about airborne and space borne imaging spectrometer systems, atmospheric correction techniques, techniques for mineral mapping, methods for spectral analysis, feature mapping and identification of minerals are explained briefly.

2. 1. Principles and Definitions

Human being can only be sense the wavelength region between 400 nm and 700 nm which is known as visible region. Remote sensing sensors are capable of acquiring information from other portion of electromagnetic spectrum (EMS). Even though some of the materials such as minerals cannot be identified in visible range, they can be defined in other portions of EMS.

Remote sensing is based on relationship between photons and surface materials. Different materials have different interaction with the electromagnetic spectrum (EMS) in different wavelength regions. Rocks and minerals generally absorb certain wavelength region of EMS depend on their chemical composition and form (Van der Meer, 1999). When the reflectance of the material plotted over a range of wavelengths, the curve is generated by

connecting those reflectance responses. The obtained curve is called *spectral signature* of the material which is unique for that material. The detail of the spectral signature directly depends on the observation detail, narrower channels (higher spectral resolution) would definitely yield in detailed and realistic spectral signatures, where characteristic absorption wavelengths and features are sought.

The ratio of the reflected and incident EMS intensity on an object is called as reflectance. The reflectance of an object is measured by a spectrometer, which records reflectance values in different wavelength regions. In other words, spectrometer can be defined as a hyperspectral sensor that measures reflectance of a material over continuous wavelength region of EMS.

Electronic Transition and Charge Transfer Processes are related with transitional metal ions and absorption features of the spectra of the minerals (Van der Meer, 2001). Crystal structure and chemical composition of the minerals affect the absorption features which are wavelength position, depth, shape, width and asymmetry (Van der Meer, 1999). Not all of the minerals in nature are pure form; they are mixtures of the pure minerals.

Spectrometer specification can be described by using four parameters; spectral range, spectral bandwidth, spectral sampling and signal-to-noise ratio (Clark, 1999). Spectral range is important to differentiate materials such as, visible-near infrared (VNIR) range used for vegetation having chlorophyll and transition metals especially iron and rare earth elements, short wave infrared (SWIR) region is used to distinguish carbonate, hydrate and hydroxide minerals, and thermal infrared (TIR) region is mainly used for quartz and feldspar discrimination (Rowan, and Mars, 2002).

The width of an individual spectral band in the spectrometer is its spectral bandwidth. The narrower the spectral bandwidth, the narrower the absorption feature the spectrometer can measure accurately (Clark, 1999). In order to

differentiate minerals and mineral groups, absorption wavelengths should be defined, and then high spectral resolution is required. When comparing spectral separability between Landsat TM and ASTER images having 7 and 14 spectral channels respectively, clay mineral groups can be discriminated in Landsat TM data, however, other detailed clay minerals such as alunite, kaolinite and montmorillonite can be defined in ASTER data. Therefore, if the number of spectral channels increase, the better the discrimination of individual minerals are achieved and analyzed in a spatial context (Pieters and Mustard, 1988).

In addition to the number of bands and band width, another important criterion is bandpass profile shape. Bandpass profile shape of most of the spectrometers is assumed to have Gaussian distribution. The width of bandpass is usually defined as the width in wavelength of the half response level of the function which is called *full width at half maximum* (FWHM) (Clark, (1999), Borengasser et.al., (2008)) in Figure 2.1.

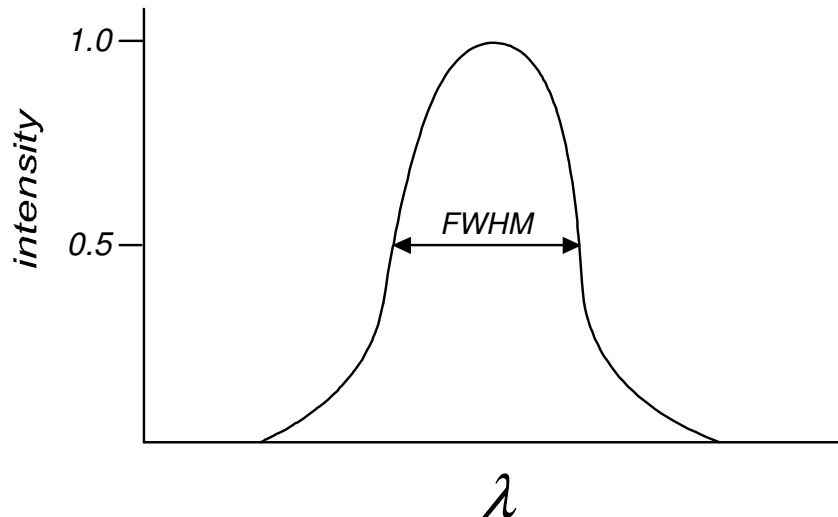


Figure 2.1. Gaussian profile with a full width at half maximum (FWHM).

The distance in wavelength between the spectral bandpass profiles for each channel in the spectrometer is called as spectral sampling which is a function

of wavelength. The term, spectral sampling, sometimes confused with bandpass (Clark, 1999).

The last parameter is the signal to noise ratio (S/N) which depends on the detector sensitivity, spectral bandwidth, and the intensity of the reflected or emitted electromagnetic energy from the surface (Clark, 1999).

Apart from the instrumental matters another important issue in hyperspectral remote sensing is atmospheric effects. Some of the EM energy is absorbed by the atmosphere which contains atmospheric gases and aerosols. Therefore, space borne remote sensing is only possible with the wavelength that is transmitted by the atmosphere (Figure 2. 2), through atmospheric transmission windows. Due to the particle size of the atmosphere and ozone absorption, any wavelength shorter than 0.35 μm of light could not be observed by the sensors. At the position of 0.76 and 9.6 μm wavelength region oxygen (O_2) and ozone (O_3) absorb the light. Carbon dioxide (CO_2) absorbs at 2.01, 2.06, and a weak doublet near 1.6 μm . (Clark, 1999). The light approximately at 0.94, 1.14, 1.38 and 1.88 μm wavelength regions are also absorbed by atmospheric water vapor (Van der Meer, 1999).

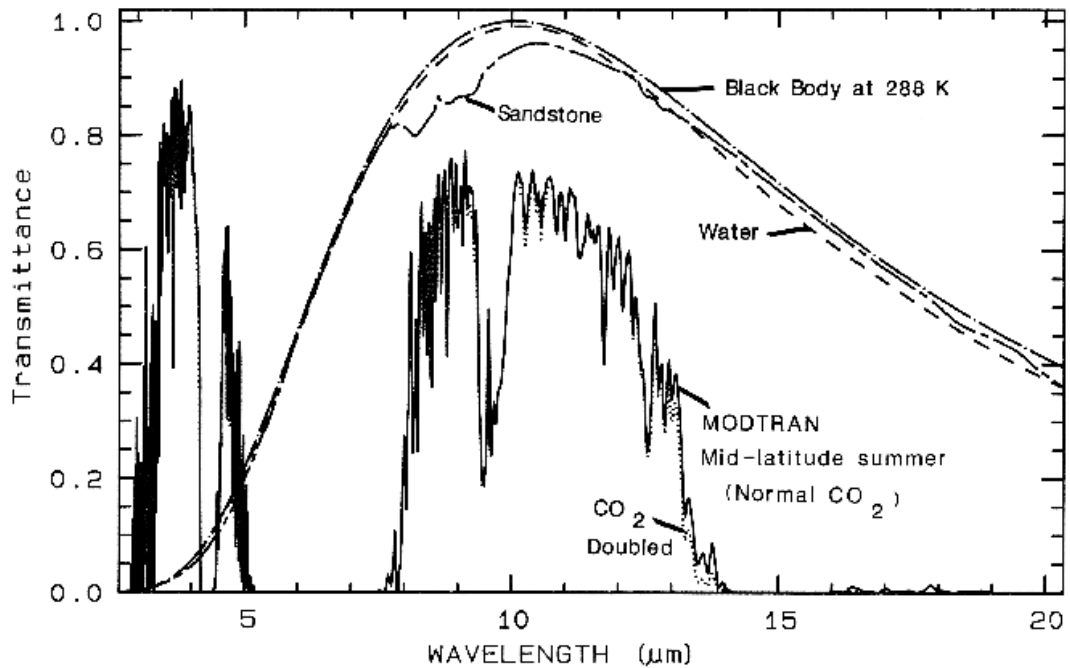


Figure 2.2. Atmospheric transmittance, mid-infrared is compared to scaled grey-body spectra. Most of the absorption is due to water. Carbon dioxide has a strong 15- μm band, and the dotted line shows the increased absorption due to doubling CO_2 . Also shown is the black-body emission at 288 K and the grey-body emission from water and a sandstone scaled to fit on this transmittance scale. The water and sandstone curves were computed from reflectance data using: 1 - reflectance times a black-body at 288 Kelvin. (Clark, 1999).

2. 2. History of Imaging Spectrometer Systems

Imaging spectroscopy is the term that is used as its synonyms; hyperspectral imaging, ultraspectral imaging in the remote sensing. By the improvement of the technology, to provide identification of surface materials, hyperspectral imaging devices which has more than hundreds of spectral channels having narrow band widths from near ultraviolet to short wave infrared is developed (Mazer et. al., 1988). Hyperspectral remote sensing is used to produce detailed maps for unmapped areas and to supplement existing geologic mapping (Kruse et. al., 1990).

Vane and Goetz (1988) presented the Airborne Imaging Spectrometer (AIS) which is developed at the NASA Jet Propulsion Laboratory. This instrument acquired data in 128 spectral bands in the range of 1.2 to 2.4 μm . By using AIS, mineral mapping of hydrothermally altered rocks in the Northern

Grapevine Mountains, Nevada and California, was performed (Kruse, 1988). Kruse (1988) used AIS to map two type of alteration; quartz-sericite-pyrite and argillic alteration on this area.

NASA prepared an improved version of AIS called the Airborne Visible/Infrared Imaging Spectrometer. The AVIRIS scanner provide the collections of images in 224 contiguous bands resulting in a complete reflectance spectrum of each pixel with ground resolution of 20 x 20 m pixel in the 0.4 to 2.5 μm region with a sampling interval of 10 nm (Kruse et. al., 1993.a.).

After the success of the AVIRIS in the mining and petroleum industries, Geophysical and Environmental Research Corporation (GER) developed a 63 channels hyperspectral airborne sensor called Geophysical and Environmental Research Imaging Spectrometer (GERIS). GERIS channels covers 0.4 to 2.5 μm wavelength region. It is used to identify the alunite, kaolinite, buddingtonite, and hematite minerals (Kruse et. al., 1990).

2. 3. EO-1 Hyperion Data

NASA planned under New Millennium Program the Earth Observation (EO-1) Mission. This program was focused on new sensor and spacecraft technologies that could directly reduce the cost of Landsat and related Earth Monitoring Systems (Pearlman et. al., 2000, Cudahy et. al., 2002). It is one of the sensor systems on EO-1 satellite platform. Hyperion has total 242 spectral channels having 30 m spatial resolution within 0.4 to 2.5 μm wavelength region. 35 channels located on visible region, another 35 channels located on the near infrared region and 172 bands are located on short wave infrared region (Beck, 2003, URL1).

EO-1 Hyperion acquires image at 10:00 a.m. local time similar to most of descending (sun-synchronous) passive sensor systems. EO-1 is having

almost the same orbit with Landsat 7 satellite and there is a 1 minute time difference with each other. The swath width of the Hyperion is 7.5 km and one image scene covers 7.5 x 100 km as a narrow strip (Beck, 2003). Due to the limited coverage area, more image data are needed for mapping of large aerial extend.

There are different levels of products for Hyperion data, the level 1 product contains radiometrically corrected but geometrically un-corrected image. The data product name indicates some information about the data set. For instance, the name of the image is "E01HPPRRRRYYYYDDDXXXPL.hdf". First three characters "EO1" stands for satellite name and next character "H" shows Hyperion sensors. EO-1 also carries another sensor which is called ALI. Therefore, the letter H is important for description. Letters PPP and RRR illustrate the path and row of the image data, respectively. YYYY stands for an acquisition year of the image, DDD demonstrate the image acquisition date in Julian date format. Next character block is XXX which refers to if the sensor is in operation or not. First X is belonging to Hyperion, second X is ALI and the last X is Atmospheric Corrector. If one of them is on position, then related letter shows "1", if else, then later shows as "0". The last two characters demonstrate the pointing mode as "P" and scene length as "L" (Simon and Beckman, 2006).

Hyperion images have signed 16-bit radiometric resolution. Each band stored in digital number having a value of 2^{16} (-32768 to 32767). In order to obtain radiance values, according to Beck (2003) digital number of VNIR channels and SWIR channels should be divided into 40 and 80, respectively. Then, the resultant numbers provide radiance values having a unit of $W/m^2 SR\mu m$.

2. 4. Pre-processing of Hyperspectral Data

Even though hyperspectral data have the potential to distinguish surface materials, some preprocessing needed to get reliable and accurate results. In

order to get rid of this atmospheric effects there are some techniques. Before the process, the raw radiance data from imaging spectrometer needs to be re-scaled to reflectance data. Therefore, all spectra are shifted to nearly the same albedo. The resultant spectra can be compared with the reflectance spectra of the laboratory or field spectra, directly. Atmospheric correction techniques can be divided into two categories which are absolute (empirical) and relative atmospheric corrections (Van der Meer, 1999).

2. 4. 1. Absolute Atmospheric Correction Techniques

In absolute reflectance correction techniques, there is no need for a priori knowledge of the surface characteristics and atmospheric model option. By this method, scattering and absorption of water vapor, mixed gases and topographic effects can be corrected.

In order to minimize atmospheric effect, atmosphere should be modeled while simulating the conditions of acquisition time. Radiative transfer codes (i.e. LOWTRAN and MODTRAN) can model the scattering effects in the atmosphere (Van der Meer, 1999). Using scattering and transmission properties of atmosphere, the difference between the radiation leaving earth and the radiation received at sensor is modeled by radiative transfer codes. These codes have different types of atmosphere models for a large number of atmosphere types intended for calculation of atmospheric radiance spectrum on a pixel-by-pixel basis.

MODTRAN (MODerate resolution atmospheric TRANsmission) is the program designed to model the atmospheric propagation of electromagnetic radiation from visible to far infrared region with a spectral resolution of 100 μm . It is licensed to U.S. Air Force and core modules are written in FORTRAN code. Similarly, LOWTRAN (low-resolution propagation model) algorithm computes the higher spectral resolution and the greater accuracy. Therefore, both MODTRAN and LOWTRAN use scattering and transmission

properties of the atmosphere, the difference between the radiation leaving the earth and the radiation received at sensor.

In this study, four different atmospheric correction modules (Atmospheric CORrection Now (ACORN), ATmospheric CORrection (ATCOR2 and ATCOR 3), and the Fast Line-of-sight Atmospheric Analysis of Spectral Hypercubes (FLAASH)) were used to remove atmospheric effects of the Hyperion data before the processing steps. And then, these techniques are compared with the reference data to get the successful one. The next three sections give information in detail about these correction algorithms.

2. 4. 1. 1. Atmospheric CORrection Now (ACORN)

Atmospheric CORrection Now (ACORN) software has been developed for atmospheric correction of hyperspectral and multispectral image data (ACORN Tutorial, 2004). It is stand alone software, based on MODTRAN4 (Goetz, et. al., 2002), but it has no visualization component. The equation 2.1. shows the relationship between participations of the solar source, atmosphere and surface to the radiance measured by the sensor.

$$L_t(\lambda) = F_0(\lambda)\{\rho_a(\lambda) + T_d(\lambda)\rho(\lambda)T_u(\lambda)/(1 - s(\lambda)\rho(\lambda))\}/\pi \quad (2.1)$$

where, L_t is the total radiance arrived at the sensor, F_0 is the top of the atmospheric solar irradiance, ρ_a is the reflectance of the atmosphere, T_d is the downward transmittance of the atmosphere, ρ is the spectral reflectance of the surface, T_u is the downward transmittance of the atmosphere, s is the downward reflectance of the atmosphere, λ is spectral wavelength. Equation 2.2. gives apparent surface reflectance.

$$\rho(\lambda) = 1/\left[\left\{\left(F_0(\lambda)T_d(\lambda)T_u(\lambda)/\pi\right)/\left(L_t(\lambda) - F_0(\lambda)\rho_a(\lambda)/\pi\right)\right\} + s(\lambda)\right] \quad (2.2)$$

The equation 2.1 and 2.2 are used in ACORN for atmospheric correction model. Goetz et. al. (2002) stated that using ACORN corrected data provided accurate results for minimum noise fraction image.

2. 4. 1. 2. ATmospheric CORrection (ATCOR2 and 3)

ATmospheric CORrection (ATCOR) is used for computing a ground reflectance image for the reflective spectral bands, and emissivity images for the thermal bands (Richter, 1996). ATCOR algorithm has been developed by the scientists in the last decade and it has two different types. These are ATCOR 2 and ATCOR 3 which are the atmospheric correction capability created by Dr. Richter of the German Aerospace Center - DLR. For nearly horizontal surface or flat terrain, ATCOR 2 is a spatially-adaptive fast atmospheric correction algorithm, whereas, ATCOR 3 is designed for rugged topographical surface. Digital Elevation Model (DEM) is used in the ATCOR 3 algorithm for atmospheric correction (PCI Geomatica Help, 2003).

2. 4. 1. 3. Fast Line-of-sight Atmospheric Analysis of Spectral Hypercubes (FLAASH)

The Air Force Research Laboratory, Space Vehicles Directorate (AFRL/VS) develops a software package, the Fast Line-of-sight Atmospheric Analysis of Spectral Hypercubes (FLAASH) atmospheric correction code which derives its physics-based algorithm from the MODTRAN4 radiative transfer code (Felde et. al., 2003). FLAASH is designed to eliminate atmospheric effects caused by molecular and particulate scattering and absorption from the radiance at the sensor and to obtain reflectance at the surface.

FLAASH uses a standard equation of spectral radiance at a sensor pixel (L) that applies to solar wavelength range and flat Lambertian materials. The equation (2.3) is shown as follows (ENVI Manual, 2005);

$$L = \left(\frac{A\rho}{1 - \rho_e S} \right) + \left(\frac{B\rho_e}{1 - \rho_e S} \right) + L_a \quad (2.3)$$

where, ρ is the pixel surface reflectance, ρ_e is an average surface reflectance for the pixel and a surrounding region, S is the spherical albedo of the atmosphere, L_a is the reflectance back scattered by the atmosphere, A and B are coefficients that depend on atmospheric and geometric conditions but not on the surface.

In brief, the algorithm computes the physics based calculations from the MODTRAN4 radiative transfer code. In order to obtain reflectance at surface values from the radiance-at-sensor measurements and to eliminate atmospheric effects based on molecular and particulate scattering, is the main purpose of the FLAASH module (Felde et. al., 2003).

2. 4. 2. Relative Atmospheric Correction Techniques

Relative atmospheric correction method uses directly image brightness values which means that all the reflectance value of pixels are computed relatively to each other. There is no need to a priori knowledge of the surface characteristics and atmospheric model in this method. In relative reflectance correction techniques, there are mainly four different methods which are logarithmic residuals, flat field correction, internal average relative reflectance correction, and empirical line correction. Theoretically, differences between laboratory spectra and observed spectra from sensor are due to topographic effects and difference in solar illumination. The radiance is equal to multiplication of topographic factor, reflectance and illumination factor. The topographic factor is the surface variability that is constant for all wavelengths. Illumination factor which is a function of wavelength changes for different wavelength. In order to remove these effects, original radiance value of individual wavelength is divided by geometric mean of all channels and then, the logarithm of the resultant data computed. This is called as

logarithmic residuals, or shortly *log residuals* (Green and Craig, 1985). The log residual transformation is presented as following formula (2.4) (Hutsinpillar, 1988);

$$\text{Log}(\text{Res}_{i,j}) = \log(\text{DN}_{i,j}) - \log(\text{aveDN}_i) - \log(\text{aveDN}_j) + \log(\text{aveDN}_g) \quad (2.4)$$

where,

$\text{Res}_{i,j}$ = residuals value for pixel i and channel j,

$\text{DN}_{i,j}$ = value of input pixel for pixel i and channel j,

aveDN_i = average value of all channels for pixel i,

aveDN_g = global average of all pixels for all channels

After application of log residual, original spectra loose some information. For instance, if most of the image coverage area contains absorption features for certain bands, then average values are changed and the log residual spectra is not strong enough to differentiate the strong absorption features. Although some limitations of log residuals exist, log residual transformation of radiance spectra is useful to interpretation of minerals. According to the equation 2.4. (Hutsinpillar, 1988), log residual spectra are affected by mean values of the scene. If strong absorption minerals exist in the scene, then average value reflects these features and less intense absorption features can be seen on log residual spectra. In order to eliminate this effect, average values calculated from the flat portion of the scene. This is called as *flat field correction* (Hutsinpillar, 1988). Flat field correction is almost the same as log residual technique, but only average flat surface of the scene is used instead of average values in this case (2.5). Hence, the average values do not affected to existing strong absorption features on the image.

$$\text{Log}(\text{FFRes}_{i,j}) = \log(\text{DN}_{i,j}) - \log(\text{aveDN}_i) - \log(\text{aveDN}_{\text{FF}}) + \log(\text{aveDN}_{\text{FF}g}) \quad (2.5)$$

where,

$\text{FFRes}_{i,j}$ = flat field residual value for pixel i and channel j,

$DN_{i,j}$ = value of input pixel for pixel i and channel j,

$aveDN_{FF}$ = average value of all channels in spectrally flat area for all channels,

$aveDN_{FFg}$ = global average of all pixels in spectrally flat area for all channels.

The other technique is to remove or reduce atmospheric effect is internal average relative reflectance (IARR) correction which allows the calibration of raw imaging spectrometer data to reflectance data when no calibration information is available (Kruse, 1988). In this technique, calculated average reference spectrum is used as the average pixels spectrum of the whole scene. The division of the radiance spectrum of each pixel by this average spectrum gives the relative reflectance spectrum. This method sometimes produces wrong interpretation as spectral features (Van der Meer, 1999).

The latest technique is empirical line method which requires the selection and special characterization of two calibrated targets (Roberts et. al, 1985). In the empirical correction, a constant gain and offset for each band is used for a best fit between sets of field spectra and image spectra characterizing the same area. According to Kruse et. al. (1990), this correction requires four basic steps;

- 1- wide albedo range must be chosen such as a dark and a bright target and field spectra characterizing these targets are obtained,
- 2- more than one pixels should be chosen for both targets,
- 3- linear equations of each bands having gain and offset values is constructed and then we can obtain error of gain and offset values using least square fitting,
- 4- in order to calibrate data, data is multiplied by proper gain factor and is added the corresponding offset value.

2. 5. Techniques for Mineral Mapping

Even though, hyperspectral images have more discrimination capability for minerals or rocks, there are some problems appear during the analyses. For instance, atmosphere affects the images and sometimes too much data is present for mineral mapping which are largely redundant. Mustard and Sunshine (1999) state that there is no unique accepted methodology for spectral analysis of remote sensing data. Any techniques applied in a study are optimized for the local purpose. Those purposes can be classified as follows;

- definition and mapping of broad-scale units,
- identification of presence of specific mineralogical assemblages or lithological units,
- quantification of amount of material present.

Definition and mapping of broad-scale units:

In multispectral data, the basis of shared textural and spectral properties defines the units. Even though, some physical basis can be recognized, the specific compositional features of the units cannot be determined for the most part. Field investigations and ground truth are required for verification. For definition and mapping of broad-scale units, sensors having broad band width are used with simple spectral analyses such as color composites, band ratios and principle component analysis (PCA) (Mustard and Sunshine, 1999).

Identification of presence of specific mineralogical assemblages or lithological units:

This technique is based on the logic of reflectance spectroscopy. Mustard and Sunshine (1999) elucidated that spectral reflectance curves of earth materials are different from each other. In this technique, spectral characteristics such as absorption band shape, depth or strength and

position are used to identify the mineral type and composition, mineral assemblage, and lithology. In order to get accurate identification, ground truth information from in situ or laboratory spectrometry measurements are required.

Quantification of amount of material present:

Pixels in remotely sensed data cover mixtures of materials due to field of view. Surface materials such as rocks contain not only altered minerals but non-altered minerals also. It is difficult to detect and characterize any specific mineral or rock type using classification algorithm, however, it is possible to apply a suitable abundance algorithm (Mustard and Sunshine, 1999).

2. 5. 1. Conventional Methods for Spectral Analysis

The target material can be discriminated using some simple image processing techniques. Simple methods are not perfect identifier, however, they are effective tools and mainly used in analysis of broadband sensors such as Landsat Thematic Mapper (TM). Color composites, band ratios, and statistical transforms are the main conventional methods for spectral analysis.

2. 5. 1. 1. Color Composites

Color composite images are simple and efficient for visual interpretations. For instance, in Landsat TM image, vegetation has high DN value in band 4 and low value in band 3, clay minerals relatively have high DN values in band 5 and 7.

2. 5. 1. 2. Band Ratios

Band rationing is one of the most used and simple technique in remote sensing analysis. It is used to minimize topographical effects such as

shadows due to illumination angle, and to discriminate some surface materials. (Jensen, 1996). Main use of this method is to emphasize the anomaly of the target mineral (Abrams, 1983). For example, some alteration mineral has absorption features in certain wavelength. Alunite, for instance, has absorption around 1.6 to 1.7 and 2.145 to 2.185 μm and kaolinite has absorption around 2.185 to 2.225 and 2.235 to 2.285 μm wavelength regions. Therefore, these regions are important for discrimination of these minerals (San et. al., 2004). In ASTER images, the suitable band ratios for alunite and kaolinite are band 4 over band 5, and band 7 over band 6, respectively (Rowan, and Mars, 2002).

2. 5. 1. 3. Statistical Transforms

Band rationing methods are not effective for discriminating among materials that exhibit more slight spectral differences (Mustard and Sunshine, 1999). In order to discriminate the surface materials, developed some statistical transformation techniques are;

- principle component analysis,
- minimum noise fraction,
- selective principle component analysis,
- spectral indices method,
- de-correlation stretch.

These techniques are explained in detail as follows.

2. 5. 1. 3. 1. Principle Component Analysis

One of the techniques which is most widely used and well developed is principle component analysis (PCA) designed to reduce such redundancy in multispectral data (Lillesand and Kiefer, 2000). Resultant imagery is transformed a new principal components and it can be more interpretable

than the original image (Jensen, 1996). Unlike, band ratioing or color composites, there is no need for priori information or knowledge in PCA (Mustard and Sunshine, 1999).

PCA is generally derived from the correlation matrix between spectral bands. The correlation matrix is divided into its characteristic eigenvalues and eigenvectors using standard matrix decomposition routines (Mustard and Sunshine, 1999). Finally, the first axis or principle component has the most variance and the last component has the least. The first component generally illustrates the albedo image of the scene. Vegetation is commonly located in the second component and the next components typically highlight spectral variability of the rocks and soils.

In hyperspectral and imaging spectrometer data, the second and higher components might contain crucial information.

2. 5. 1. 3. 2. Minimum Noise Fraction

Minimum noise fraction (MNF) transform is a technique modified type of PCA. First, noise covariance matrix is derived, and then the reflectance data are Converted and rescaled to make the noise isotropic with unit variance in all bands. Next, these transferred data are examined using principal components. Due to the fact that the noise of the data set is prewhitened and distributed equally among the bands, this approach gives better results for separation of noise from real information.

2. 5. 1. 3. 3. Selective Principle Component Analysis

This technique is based on PCA was developed by Crosta and Moore (1986) for mapping iron oxide/hydroxides related to sulphide ore bodies in granite-greenstone belt terrains using Landsat TM. It was named “feature-oriented

principal component selection” (FPCS). Nowadays, it is called as *Selective Principle Component Analysis* or *Crosta Technique*.

2. 5. 2. Feature Mapping and the Identification of Minerals

In literature mainly there are three different approaches to identify minerals using hyperspectral imaging. One of them is to deal with the characteristic feature of the reflectance spectrum. In this approach, some characteristics of spectrum such as wavelength of the absorption, depth of absorption, asymmetry of the absorption and full width at half maximum (FWHM) of the absorption are used to differentiate the minerals (Green and Craig, 1985). Another approach is to use complete band shape with corresponding library spectra for feature mapping (Clark and Swayze, 1995). In this approach, the degree of similarity between the data and the spectral library data is computed by the algorithm (Mustard and Sunshine, 1999). The last approach is the absorption band modeling almost same as the other approaches which are methods for applications for which spectral libraries representative of the materials in the scene exist. However, mixture of mineral compositions is difficult to find in spectral library (Mustard and Sunshine, 1999).

In order to take out the absorption features, the overall convex background must be removed first. To perform this, the spectrum is divided to its upper convex hull (envelope) (Figure 2. 3). The resultant curve is called the hull-quotient of input curve (Green and Craig, 1985). Removing background signal reveals or emphasizes the absorption features on the spectra. Therefore, it is easy to differentiate mineral groups using these absorption features.

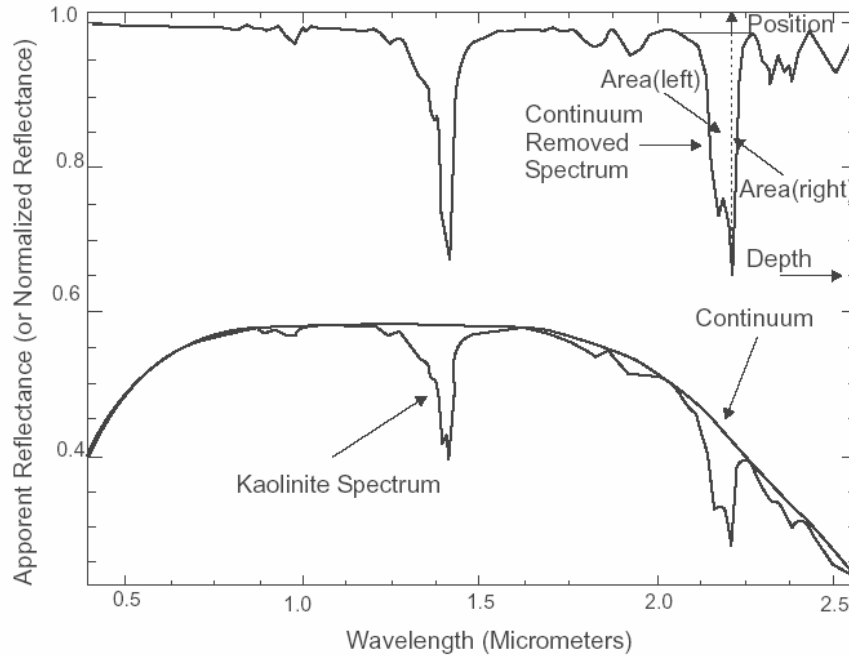


Figure 2.3. Continuum and continuum removal spectra of the kaolinite (Van der Meer, 2004).

Green and Craig, (1985) stated that laboratory spectra and radiance spectra in images are similar to each other. However, a radiance spectrum is affected by topography and solar illumination. In order to eliminate these effects, logarithmic residual or least upper bound spectrum techniques are applied (Green and Craig, 1985). These techniques are based on theoretical relationship between irradiance, topography, reflectance, and radiance. The Irradiance value is the highest and average digital numbers for each bands of the entire image in the least upper bound residual method and log residual methods, respectively (Roberts et. al., 1985).

After Atmospheric correction and obtained reflectance-like spectra, the next level is to produce absorption feature map for discrimination of surface reflectance targets. There are numerous techniques to obtain the absorption map;

- binary encoding,

- waveform characterization,
- spectral feature fitting,
- spectral angle mapping,
- spectral un-mixing,
- constrained energy minimization,
- classification,
- cross correlogram spectral matching.

2. 5. 2. 1. Binary Encoding

Binary encoding is the algorithm based on binary coding for matched or non-matched pixels as one or zero, respectively. A threshold is also applied for matching algorithm during this operation. There are three different methods of binary encoding: 1) obtained image spectra can be used as sample spectra to search whole image for similar spectra, 2) laboratory reflectance spectra used as sample spectra for searching the similar one on the entire image, 3) using a extracted spectra from the scene for searching candidate materials for matching the library spectra.

2. 5. 2. 2. Waveform Characterization

Okada and Iwashita (1992) were aimed to automatically map surface materials using hyperspectral image (GER AIS) data in Cuprite Mining district, Nevada. In preprocessing step of their study, raw digital numbers (DN) converted to reflectance-like spectra. Then resultant spectra compared with laboratory spectra for mineral and rock definition. Solar incidence, atmospheric attenuation and scatter, topographic illumination differences affect the raw data. In order to remove or minimize these effects, reflectance-like spectra can be obtained by rationing raw spectra for each pixel to average spectrum for the entire scene. This operation removes main illumination and atmospheric effects for each raw spectrum. Nevertheless, if the image contains more homogeneous part, then reflectance features of

homogeneous material can disappear in resultant spectrum. In the next step, the characteristic spectral features are extracted and parameterized. Especially, absorption features are extracted and categorized by absorption wavelength and relative depth (Okada and Iwashita, 1992). However, definition of absorption such as starting and end position of the absorption is not easy. By using the “hull-quotient” concept, absorption wavelength can be detected clearly. In this concept, reflectance spectra are called as “upper convex hull”, an envelope curve of no absorption is derived. Then, an absorption spectrum (hull-quotient) is computed by ratio between reflectance spectra and the envelope curve; therefore, isolated individual absorption features can be obtained on the hull quotient. After the correction or continuum removal, spectral curve of the material is shown in Figure 2. 3.

The most important parameters for characterization of absorption features are wavelength and depth of the absorption. However, sometimes these features are not sufficient to define materials, hence, the width of absorption, symmetry of the absorption and slope of upper hull are used to characterize absorption. Figure 2. 4 shows the absorption features of the spectrum.

Consequently, there are five different features which are position, depth, width, symmetry and slope obtained for both laboratory spectrum and image spectrum. The similarity between them illustrates the presence of characteristic absorption features.

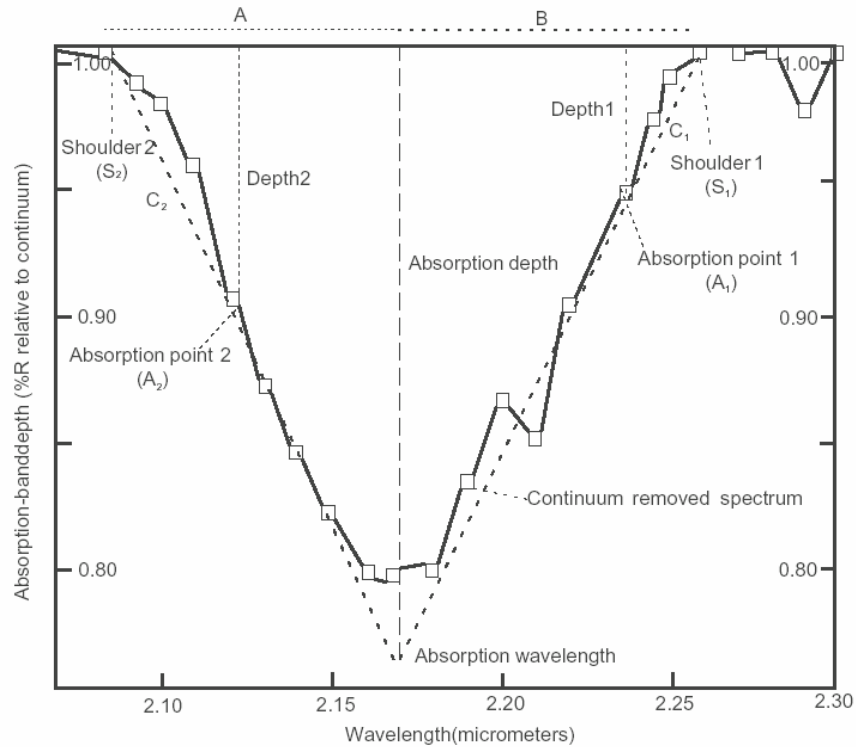


Figure 2. 4. Absorption parameters; wavelength, absorption depth, absorption width, absorption symmetry. (Van der Meer, 2004).

2. 5. 2. 3. Spectral Feature Fitting

Spectral feature fitting (SFF) is based on waveform characterization for matching image spectra to laboratory spectra. In this method, firstly, continuum removed spectra is obtained then, to define the mineral or material unknown using least-square calculation for each bands for the end member spectra of reference data. The new resultant image derived from root mean square (RMS) error of the match is created. This RMS image shows similarity of the pixels to selected reference end member (Van der Meer, 1999). In another words, SFF is a kind of detection algorithm for checking the match of the image spectra and reference end members (Borengasser et. al., 2008)

2. 5. 2. 4. Spectral Angle Mapping

Spectral Angle Mapper (SAM) is a method for mapping of spectral similarity of image to reference spectra. The laboratory, field spectra or spectra extracted from the image can be used as reference spectra. This method can be applied to apparent reflectance with all dark current and path radiance biases removed (Kruse et. al., 1993.b.). The spectral similarity between two spectra by calculating the angle between the two spectra is determined by the algorithm with the vectorial representation. These vectors are generated by connection of reflectance spectrum point with the origin. The number of vectors is equal to number of bands. Figure 2. 5. illustrates a simplified theoretical illustration of a two band image with reference and image spectrum. If illumination of the pixels is low, then it is closer to the origin (dark point). The angle between the vectors is the same regardless of their length. The computation contains taking the arccosine of the dot product of the spectra (Kruse et. al., 1993.a.). The spectral angle θ is the angle between the two vectors v_1 and v_2 ; i.e.,

$$\theta_{v_1, v_2} = \cos^{-1} \frac{v_1^T v_2}{\|v_1\| \|v_2\|} \quad (2.6)$$

Where; v_1 and v_2 represent two different surface objects with different spectral signatures (Sohn and Rebello, 2002). This formula can be written as following for more than two bands (Kruse et. al., 1993.b.);

$$\theta = \cos^{-1} \left(\frac{\sum_{i=1}^{nb} t_i r_i}{\left(\sum_{i=1}^{nb} t_i^2 \right)^{1/2} \left(\sum_{i=1}^{nb} r_i^2 \right)^{1/2}} \right) \quad (2.7)$$

Where; n_b is the number of bands, t and r is the test and reference spectrum.

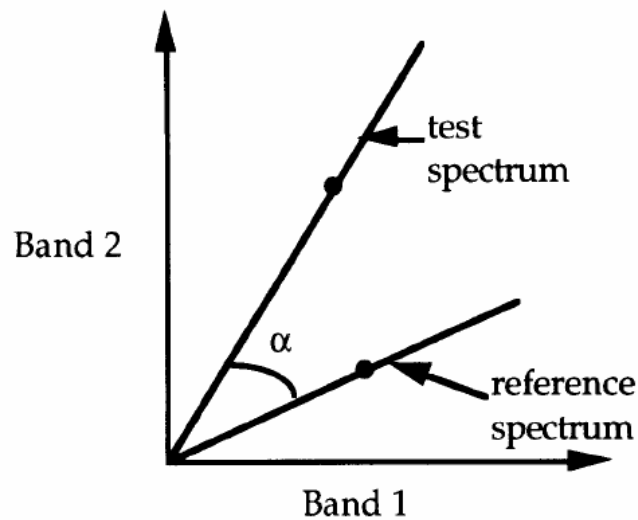


Figure 2.5. Reference and test spectrum of a two band image. The same material is represented by vectors connecting the origin (Kruse, et. al., 1993.b.).

A major difference between the spectral angle mapper and conventional classifiers is that SAM is based on the spectral shape pattern, whereas conventional classifiers are based on the statistical distribution of the pattern (Sohn and Rebello, 2002).

2. 5. 2. 5. Spectral Un-mixing

Most of the materials in the earth are not pure. They are mixture of pure materials. In order to determine the ratios of mixed material, un-mixing procedure is required. There are four different type of spectral mixtures which are linear, intimate, coatings and molecular mixtures (Clark, 1999).

In linear or aerial mixtures, the main assumption on the spectral un-mixing method is that a pixel contains the spatial mixing of the materials within the area bounded by a pixel. Each material has its own characteristic spectral signature (Van der Meer and De Jong (2001)). The mixture of these materials give the reflection of the image pixels. In other words, it is a linear

relationship between an observed spectrum (mixture) and a library spectrum (pure end members). The following expressions (2.8.a and b) can be clearly displays the relationship;

$$[A]_{M \times N} \times [X]_{N \times 1} = [B]_{M \times 1}, \quad (2.8.a)$$

$$[X]_{N \times 1} = [A]_{M \times N}^{-1} \times [B]_{M \times 1} \quad (2.8.b)$$

Where; A is an end-member library matrix having M by N dimension, X is an N by 1 abundance vector, and B is an M by 1 observed data vector with M as the total number of bands and N is the total number of mixing end members. The end-member library matrix and observed pixel spectrum are known and the abundance values are unknown. Therefore, if the number of end members and the number of spectral bands are equal to each other, by means of a least squares approximation the equation can be solved. At the end of this process, total abundance of each known end member is computed for each pixel with the RMS error of match between the observed mixed spectra and the reference spectra.

Boardman et. al. (1995) asked the following question: “are my target signatures present in the scene, and if so, how much of each target material is present in each pixel?“. Pixel purity index (PPI) is a method to find out spectrally pure pixels in a data set. In this application, the data are repeatedly projected onto random unit vectors. The extreme pixels in each projection are recorded and a cumulative account of the pixels having extreme scores for each time is identified as pure pixels.

Intimate mixture is a mixture that materials having intimate contact in a scattering surface such as mineral grains in a rock or soil (Clark, 1999). Intimate contact is known as non-linear mixture.

If one material coats another, this results in change in the reflection properties (Clark, 1999).

The last mixture is molecular mixture which occurs on a molecular level (Clark, 1999).

Figure 2. 6. illustrates the spectra of different types of mixtures of alunite and jarosite minerals. In linear mixture, bright and dark minerals mixed as 50 %, then spectra of aerial mixture is exactly the linear combination of them. On the contrary, intimate mixture is observed as darker than aerial mixture in the wavelength of 400 to 1300 nm due to photons are absorbed by the dark grains (Clark, 1999).

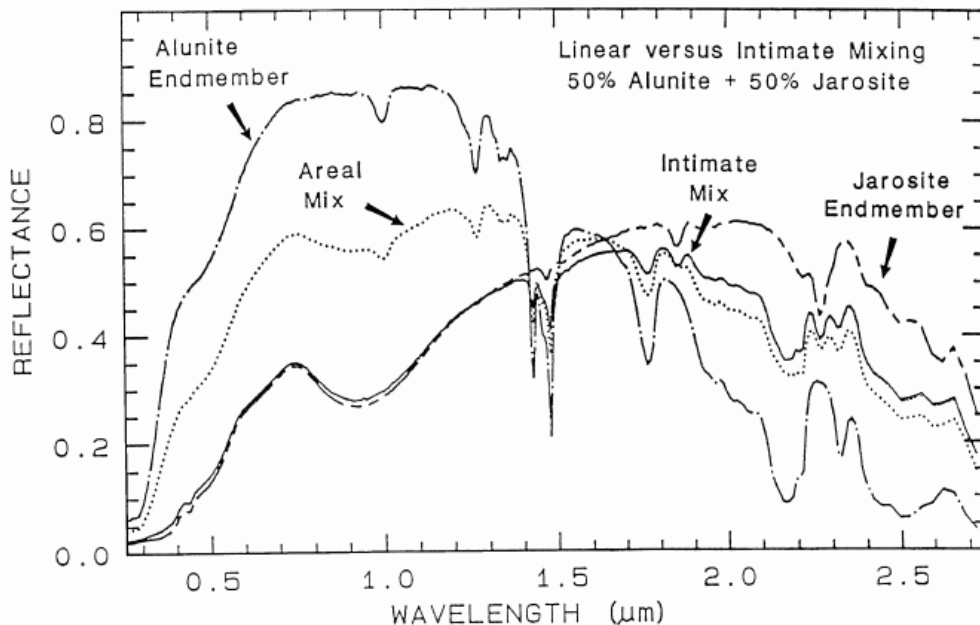


Figure 2.6. Reflectance spectra of alunite, jarosite and mixtures of them. Two different mixture which are aerial and intimate are shown (Clark, 1999).

2. 5. 2. 6. Constrained Energy Minimization

Constrained energy minimization (CEM) developed by Farrand and Harsanyi (1997), is an extension to spectral un-mixing. The main idea of this technique is to maximize the response of the target and suppress the response of undesired background signatures. Foreground and background signatures

are assumed as linearly mixed to each other (Van der Meer, 1999). In order to suppress unknown background and enhance the target signature, the total output energy of all pixels is minimized and total energy of an individual pixel is assumed to equal to one. The resultant image of CEM is the vector component having information of abundance.

2. 5. 2. 7. Classification

Classification of remotely sensed imagery is based on spectral similarity of pixels in the data. The classification can be divided into two groups which are supervised and unsupervised classifications. If the surface material is known, then training pixels are collected to construct a signature of the target to classify. This is known as supervised classification. On the other hand, if there is no any priori information about the site, it is called as unsupervised classification. The main objective of the classification is to replace visual analysis of the image with quantitative techniques for automating the identification of features in the scene (Lillesand and Kiefer, 2000).

Cetin et. al. (1993), and Cetin and Levandowski (1991) produced n-dimensional probability density functions (nPDF) which is based on the principle of the maximum likelihood classifier for analyzing AVIRIS, TIMS and Landsat TM data. The nPDF plots supply a apparent perspective of distribution of the data. After application of this method, data in nPDF space can be divided according to the distribution of training data. This technique is applicable for both supervised and unsupervised classification scheme.

Lee and Landgrebe (1993) illustrated the inaccurate estimation of first and second order statistics and they stated that algorithms for the minimum distance classifier in high-spectral resolution data.

Benediktsson et. al., (1995) used neural network classification for alternatives of conventional classification techniques. Neural network is a process which

connects the neurons. Each neuron receives input signals delivered by another neuron with different output value. In order to activate neurons, each neuron has their own threshold values. Benediktsson et. al., (1995) applied this technique for AVIRIS image data in Koldukvislarbotnar which is located on the Neovolcanic Zone in South-Central Iceland.

2. 5. 2. 8. Cross Correlogram Spectral Matching

Calculation of cross correlation coefficient between a test and reflectance spectrum creates a basic cross correlogram. Cross correlogram is derived by computing the cross correlation at different match positions between reflectance spectrum and a test spectrum by shifting the reference spectrum over subsequently channel positions (Van der Meer, 2001).

$$r_M = \frac{N \sum \lambda_r \lambda_t - \sum \lambda_r \sum \lambda_t}{\sqrt{[N \sum \lambda_r^2 - (\sum \lambda_r)^2][N \sum \lambda_t^2 - (\sum \lambda_t)^2]}} \quad (2.9)$$

Where, r_M = cross correlation at match position M,

λ_t = test spectrum,

λ_r = reference spectrum,

N= number of overlapping positions (spectral bands),

M= the match position.

If there exists a perfect matching between reference and test data, then peak correlation is obtained as 1. A deviation from this shape illustrates different surface mineralogy. Correlation coefficient, the moment of skewness and the significance are the parameters that are crucial for mineral mapping (Van der Meer, 1999).

Briefly, a simple and straightforward technique, Cross correlogram spectral matching (CCSM), allows quantification of the spectral similarity between remotely sensed data and field spectra (Van Der Meer and Bakker (1997) and Van der Meer, (2004)).

CHAPTER 3

DATA PREPARATION

The study is composed of four groups of image processing tasks which are data preparation, atmospheric correction, cross track illumination (smile) correction, and classification/thematic mapping. The necessary processing steps of the proposed approach are summarized in the flow chart given in Figure 3. 1. This chapter contains detailed information about data preparation with geometric correction and masking operations for EO-1 Hyperion hyperspectral images of Ekecek and Biga test sites.

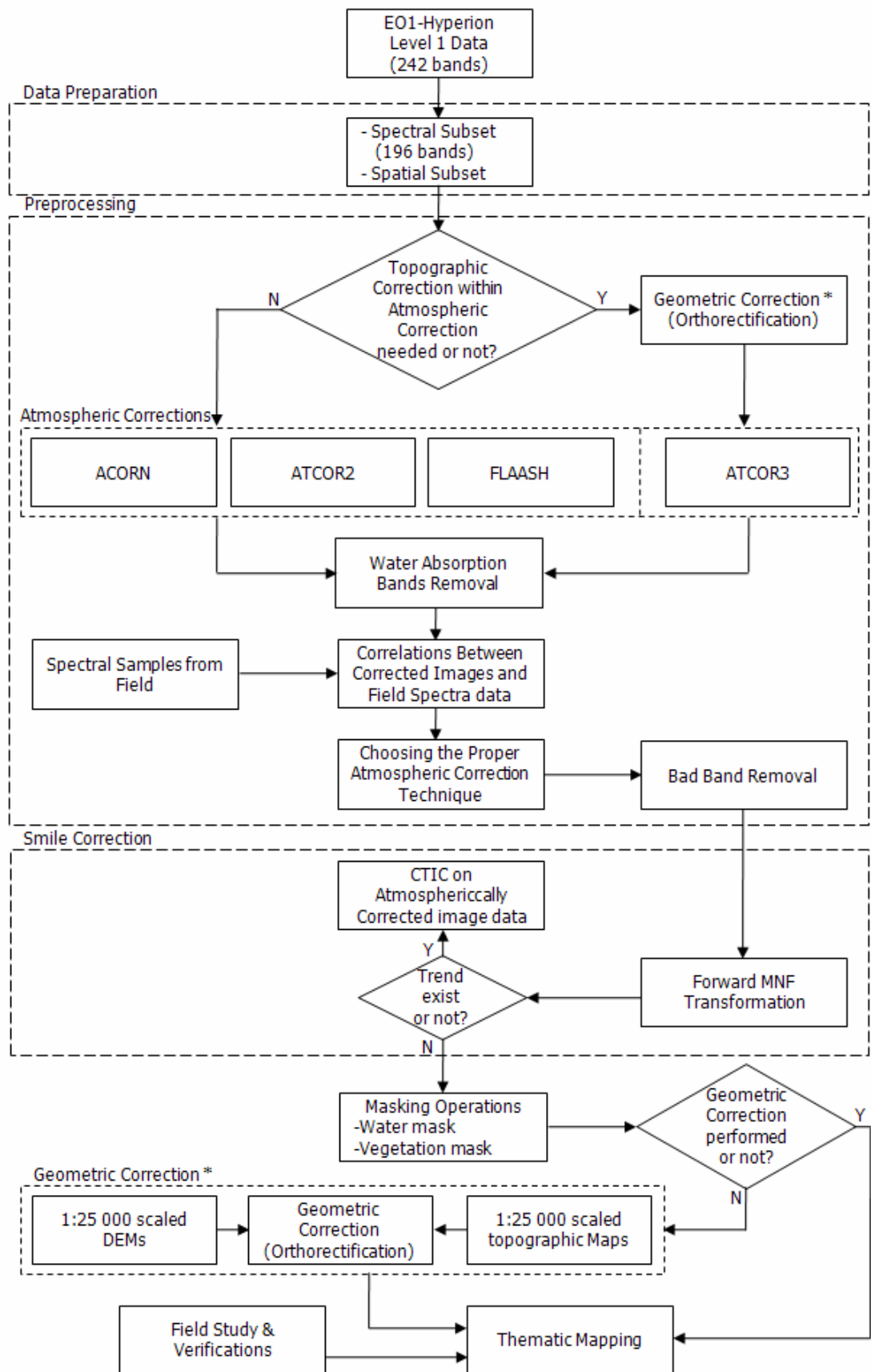


Figure 3. 1. The flow chart of proposed approach for Hyperion image data processing.

3. 1. Elimination of Un-calibrated Bands and Spatial Subset

When Hyperion level 1 data acquired, it has originally 242 spectral bands. Among them only 198 bands are radiometrically calibrated (Beck, 2003). There is an overlap between visible-near infrared (VNIR) and short wave infrared (SWIR) in 2 bands which should be eliminated before starting the process. Therefore, radiometrically calibrated valid 196 Hyperion bands from band 8 to 56 for VNIR and 78 to 224 for SWIR were used for analyses in this study (Figure 3. 2.).

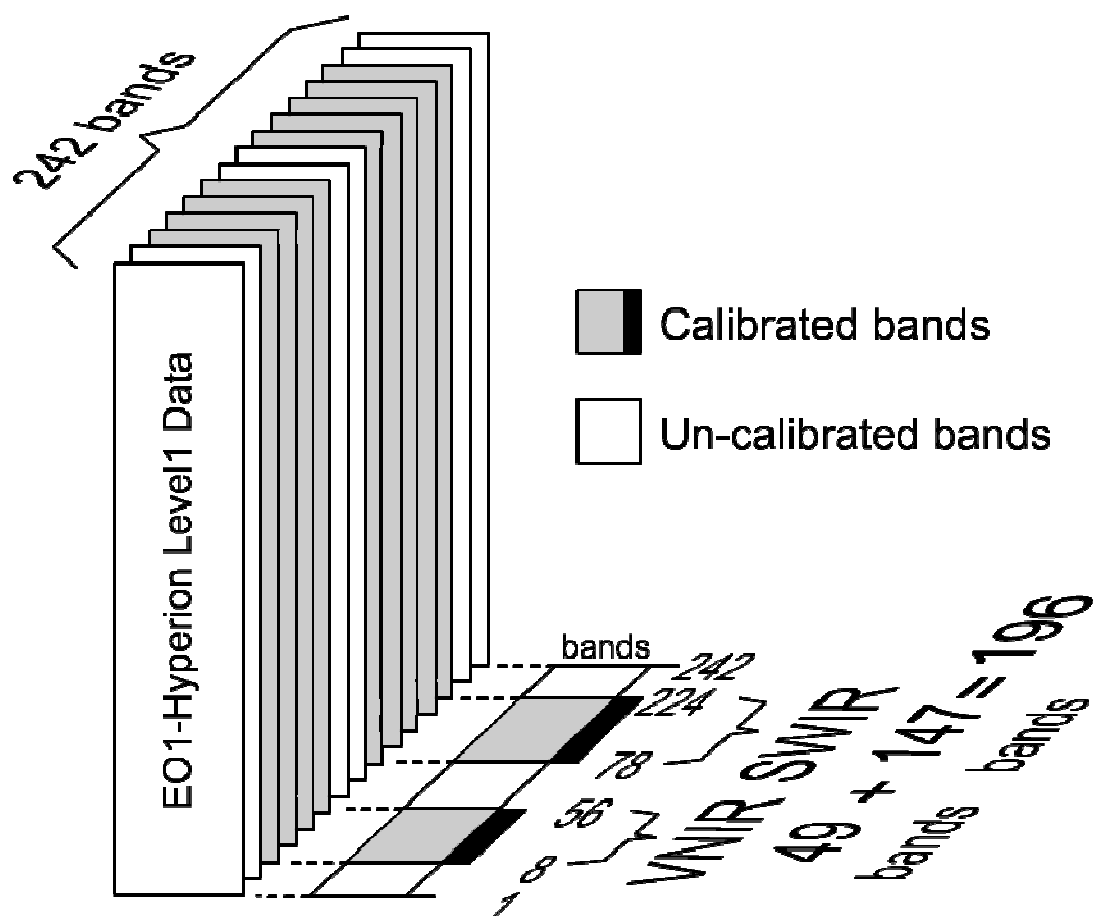


Figure 3. 2. EO1-Hyperion Level 1 image data and its calibrated channels.

As a result of the band elimination operation, there are 49 bands for VNIR and 147 bands for SWIR. The raw 242 bands are spectrally subsetted into radiometrically calibrated 196 individual bands that range in between 426.82 nm to 2395.50 nm while each individual band covers a 10 nm wavelength width.

In order to deal with the interested area, a spatial subset is also taken in this stage of the study. For instance, target area in Biga test site is mono mineralic outcrops hence the image is subsetted considering the aerial distribution of these units. Reducing the aerial extent would yield in spectrally more uniform rock units than mixed land cover types which would definitely yield in better discrimination and classification accuracies. The second advantage of spatial subsetting is that unused or un-necessary classes are eliminated before the classification stage. Furthermore another advantage could be listed as speeding up the operations performed in the study due to smaller image extents.

3. 2. Geometric Correction

Geometric correction is the process of transforming image plane onto real earth coordinates while adjusting the remotely sensed imagery to a specified map projection and selected datum. Most digital image analysis systems provide fundamental tools to perform geometric correction procedures. In some cases, geometric correction is better to be applied after the whole image processing steps to keep the original digital numbers (DNs). However, ATCOR3 (ATmospheric CORrection 3) atmospheric correction procedure requires a Digital Elevation Model (DEM) during the atmospheric correction. Therefore, geometric correction should be done prior to atmospheric correction steps.

The header file of EO1-Hyperion image data contains information about image raw coordinates. Unfortunately, these coordinate points are taken from satellite's Global Positioning System (GPS), hence, they only show some

approximate coordinates as the terrain shape and the velocity of the platform is not accurately encountered. Based on this fact a geometric correction must be applied using the true coordinate points collected from reference maps or field data. In this study, the reference maps used are 1:25,000 scaled topographical maps of the General Command of Mapping, Turkey.

The extent of the Hyperion imagery is a long rectangle having 100 km length and 12.7 degrees of azimuthal deviation in long axis. This long skinny extent yielded in uneven distribution of Ground Control Points (GCPs) where the polynomial models in ordinary rectification are not found to be suitable for geometric correction. In order to obtain a better fitted model, the image is orthorectified. Orthorectification uses map or image as the planimetric reference and DEM for correction in z-direction. Whole Hyperion image was orthorectified to Universal Transverse Mercator (UTM) projection using 12 GCPs with Erdas Imagine software for Ekecek image. The residual errors were obtained as ± 0.419 and ± 0.868 pixels for easting and northing respectively. The total root mean square error (RMSE) was ± 0.964 pixels. Figure 3. 3 (a) shows the locations of the collected GCPs on the Hyperion image of Ekecek.

Similarly, same orthorectification routine is performed for Hyperion data of Biga site. In this case, 29 GCPs were collected on the site and the residual errors were obtained as ± 0.648 and ± 0.809 pixels for easting and northing respectively. The total root mean square error (RMSE) was ± 1.037 pixels.

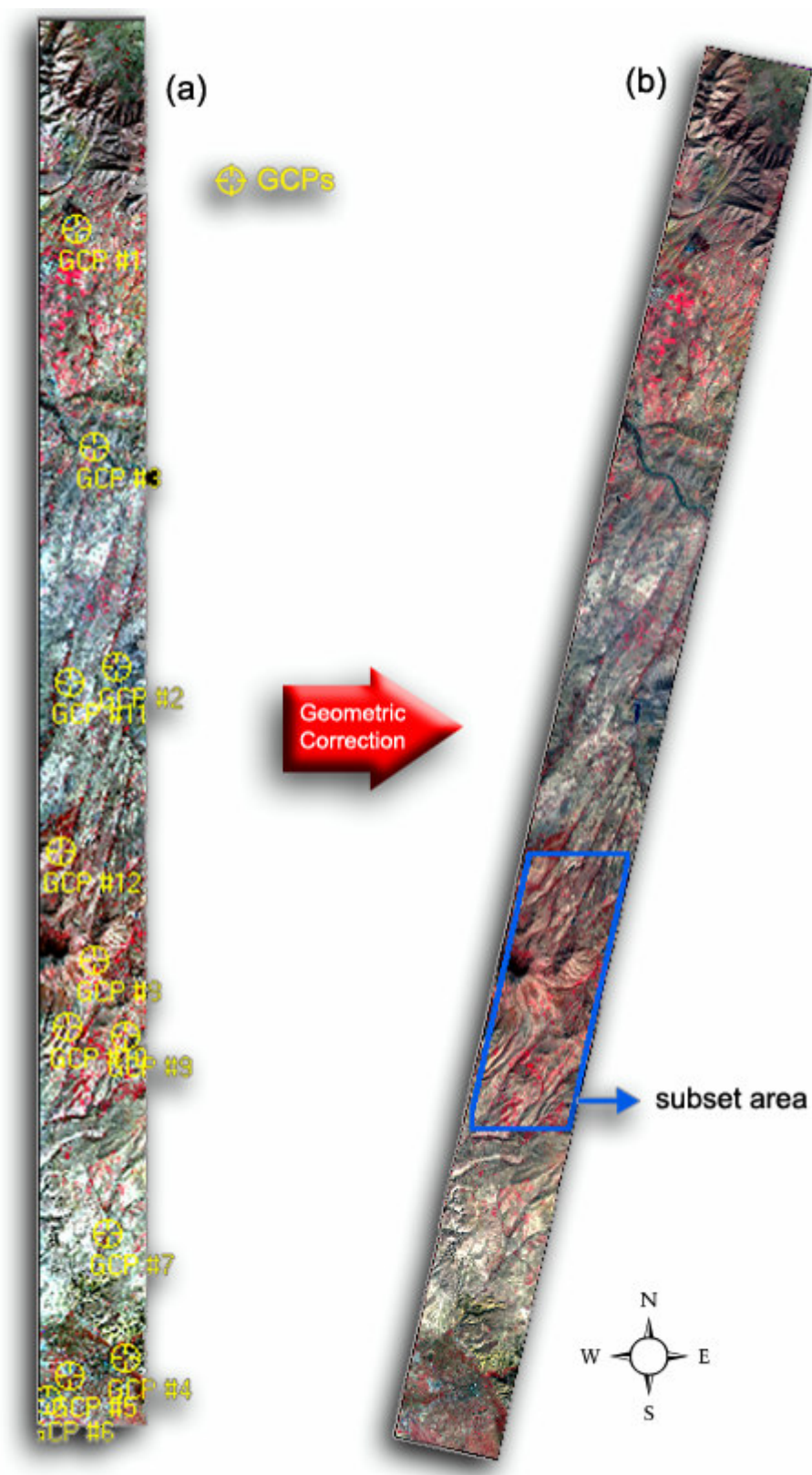


Figure 3. 3. The locations of collected ground control points on the raw Hyperion image for Ekecek test site.

3. 3. Masking Operations

Although the study area 1 (Ekecek test site) was deliberately chosen because of its sparse natural vegetation, presence of agricultural fields and pasture on river banks hamper the accuracy of the classification. Furthermore water bodies (dam reservoir area, lakes and rivers) are intentionally left out of any analysis. Therefore, vegetated areas, water bodies and no image data part for geometrically corrected image were masked out during the study.

In order to generate the mask for vegetation, the vegetated areas should be extracted by one of the well known vegetation indices, as there are more than 20 vegetation indices in literature (Jensen, 2000; Yesilnacar and Suzen, 2006). In this study, Normalized Difference Vegetation Index (NDVI) (Deering et. al. 1975) was used for vegetation mask computation. NDVI is a simple arithmetic operation for emphasizing the vegetation cover on the image. The following formula (3.1) shows the NDVI calculation;

$$NDVI = \frac{NIR - R}{NIR + R} \quad (3.1)$$

where, NIR is the near-infrared band and R is the red band. After this operation, obtained image has a range between -1 and +1. Values of highly vegetated areas are approaching to +1 and non-vegetated areas have values of -1. However Hyperion has numerous near-infrared and red channels and during the study, wavelength of 721.90 nm (band 30 in Hyperion data) and 874.53 nm (band 45) were used as red and near-infrared regions, respectively. When NDVI is applied, all vegetated area would appear as brighter pixels (Figure 3. 4 (a)). The resultant image is continuous data, which needs to be segmented in order to yield in a definite boundary mask, hence threshold is applied to the data. After inspecting image and combining field information, value of 0.16 was accepted as a threshold to detect vegetation boundary of Ekecek image. Smaller values of this threshold are

defined as non-vegetated area and the rest of the data was take into account as vegetated area.

Similarly, another masking operation was carried out for water bodies. In this case, near-infrared wavelength was used to detect water bodies. The wavelength of 874.53 nm which is the band 45 was used as a key to water and land separation.

At the end of these processes, there are two main masks of which their union extent is defining the area of interest hence the data to be used in this study (Figure 3. 4 (b)).

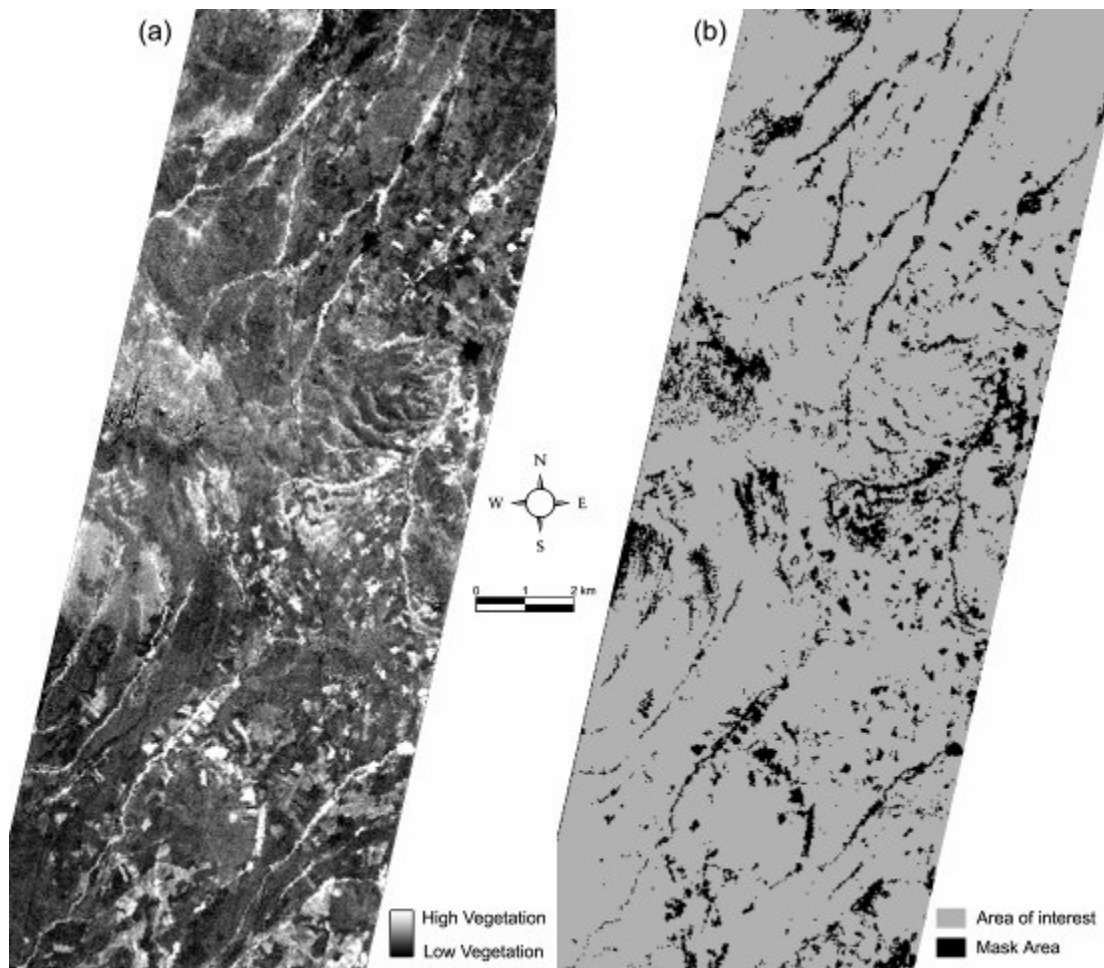


Figure 3. 4. NDVI image (a) and Area of interest (b) is used for analysis in the study area of Ekecek.

CHAPTER 4

ATMOSPHERIC CORRECTION

This chapter contains application of four atmospheric correction techniques (ACORN, ATCOR2-3, and FLAASH) and their comparisons according to the reference spectra. Then, proper atmospheric correction technique is determined for the further process. In order to perform these comparisons, Ekecek test site is selected. This is because, Ekecek area is located on the Central Anatolia which has dry climate and water vapor effects are less than coastal zones. Therefore, one of the environmental artifacts, atmospheric moisture content, is minimized by choosing this site.

Although EO1-Hyperion image data is a powerful tool for mineral discrimination, it is difficult to prepare for image analysis. It requires rigorous atmospheric correction before the analysis. Different wavelengths interact with atmosphere in different ways, due to the presence of different sized unidentified unpredictable particles or molecules within the atmosphere.

The absolute or empirical atmospheric correction techniques utilize reference atmospheric model and image header information which contains acquisition date and time. Atmospheric scattering, absorption of water vapor, mixed gases, and topographic effects are major input parameters for digital numbers to radiance conversion. Image pixel values of individual bands are

turned into the absolute radiance values at the end of the computations. In absolute atmospheric correction, method is directly related about the environmental conditions and location of the image scene. The generated model simulates the atmospheric conditions at image acquisition time. In the next sections, these four atmospheric corrections are explained in detail.

4. 1. Atmospheric CORrection Now (ACORN)

The simple atmospheric correction for calibrated hyperspectral data; Mode 1 in the ACORN software (ACORN v.5.1) is chosen to be implemented. At the beginning of the computation, ASCII text files included wavelength and corresponding Full Width Half Maximum (FWHM) of all channels, gain and offset values of all channels are prepared. The wavelength and FWHM information are acquired from header information of the Hyperion data. However, the information from the header file contains 242 channels. After elimination of the un-calibrated image channels, 196 channels have been left for image analysis. Then, corresponding information of the wavelength and FWHM values to subset channels are taken from the header file. Gain file contains 1/40 and 1/80 values for VNIR and SWIR, respectively. Bands 1 to 49 stand for VNIR regions and the rest of the 147 bands are in SWIR regions.

Except for the wavelength, FWHM, gain and offset information; image scene center location, image acquisition day and time, image dimension, file format (Band Interleaved by Line (BIL) or Band Interleaved by Pixel (BIP)), average surface elevation, acquisition altitude, and reference atmospheric model (mid-latitude summer, mid-latitude winter or tropical) information are entered in ACORN interface (Appendix A) and the software have been run.

4. 2. ATmospheric CORrection (ATCOR2 and 3)

During the study, ATCOR2 and ATCOR3 algorithms are used that are bundled in PCI Geomatica image processing software. Main difference of

ATCOR3 algorithm from ATCOR 2 is to need to use a Digital Elevation Model (DEM) during the atmospheric correction. In order to obtain the same pixel location of the DEM data and Hyperion data, geometric correction is required. To facilitate proper geometric correction of the data, orthorectification is applied to the image that will be enlightened in geometric correction section.

ATCOR2 and ATCOR3 use an ASCII text file which is a calibration file that contain the wavelength offsets and gain information of channels similar to the ACORN atmospheric correction software (Appendix B).

4. 3. Fast Line-of-sight Atmospheric Analysis of Spectral Hypercubes (FLAASH)

Before starting to use FLAASH module in ENVI, Hyperion data is to be converted in to BIL format. FLAASH module requires an ASCII text file having scale factors of VNIR and SWIR channels. This file can be obtained from USGS scale file or it can be entered by manually. The scale factor is 400 for VNIR channels and 800 for SWIR channels. The scene center, mean elevation, sensor altitude, image acquisition date and time, reference atmospheric model, and aerosol model are selected and entered in software interface (Appendix C).

4. 4. Water Absorption Bands Removal

Hyperion data ranges in between 400 nm and 2500 nm wavelengths. The water vapor is absorbed at 940 nm (Van der Meer, (1999), Sanders et. al., (2001), Liang, (2004), Marion et. al., (2006)), 1130 nm (Felde et. al., (2003), Goetz et. al., (2002)), 1380 - 1400 (Van der Meer, (1999), ACORN Tutorial, (2004)) and 1870 nm - 1900 nm (Staenz et. al., (2002), ACORN Tutorial, (2004)). Because of the water vapor absorption, most of the atmospheric correction algorithms suppresses or eliminates this wavelength portion from the whole image channels. Figure 4. 1. shows the spectral curve of one random pixel from raw image, ACORN, ATCOR2, ATCOR3, and FLAASH

corrected images, respectively. The regions A and B stand for the wavelength of 1296 nm to 1467 nm and 1740 nm to 1992 nm, respectively which illustrate the main water vapor regions (San and Suzen, 2007). If the water vapor absorption region A and especially region B are not eliminated, then the information from this region can not be evaluated and compared correctly. As can be seen on the Figure 4. 1, ACORN corrected data (Figure 4. 1 (b)) on the region A and B are suppressed by the algorithm. On the contrary, spectral signal response curves asymptotically large positive or negative values at the region B for ATCOR2-3 and FLAASH corrected data.

Therefore, after the atmospheric correction process, band removal must be carried out for water vapor wavelength regions. In this study, totally 44 bands are eliminated from each atmospherically corrected image data. After the removal of these 44 water absorption bands, 152 valid image channels were left for image processing and comparison of atmospheric correction techniques.

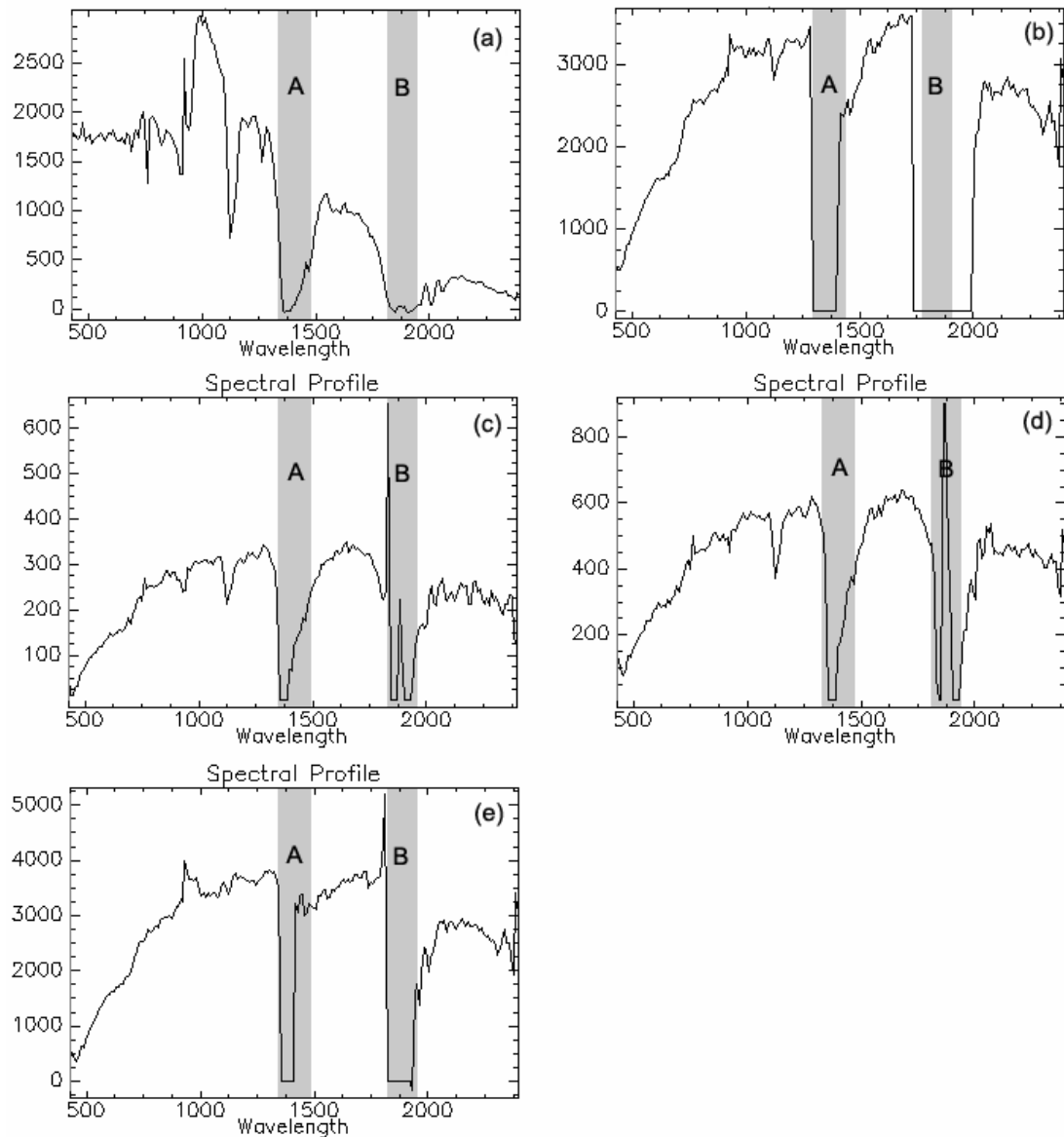


Figure 4. 1. Spectral curve of one pixel sample on raw image (a), ACORN corrected image (b), ATCOR2 corrected image (c) ATCOR3 corrected image (d), and FLAASH corrected image (e). The wavelength region A (1296 nm to 1467 nm) and B (1740 nm to 1992 nm) are eliminated during the analysis stage due to water vapor absorption.

4. 5. The Comparison of Atmospheric Correction Techniques

During the study, one of the objectives is to compare the existing atmospheric correction algorithms for Hyperion image processing. Owing to this purpose, all operations performed as parallel processes for all of the atmospherically corrected images. The proper atmospheric correction

algorithm is defined in this section and would be utilized before any further processes.

Atmospheric correction techniques are compared beyond the scope of two different aspects. One of them is the cross-correlation between atmospherically corrected image spectrum and corresponding pixel spectrum from field measurements. Another is the comparison of spectral curves with the reference spectrum in specific wavelength absorption regions. For both comparisons, 15 field sample spectra (A1, A2, A3, A4, A6, A7, A8, A9, B2, B5, B10, B12, B13, B17, and B20 in Appendix D) are used as a reference data source for the Ekecek test site.

4. 5. 1. The Cross Correlations between Image Data and Field Spectra Data for Each Atmospheric Correction Algorithm

In order to perform appropriate comparison of the atmospherically corrected images, 15 samples were collected from Ekecek test site. Figure 4. 2 shows the location of collected samples and their photos from the study area. A detailed sampling strategy is applied considering that all of the samples should be taken from uniform and largely outcropping rock units as much as it could be possible. After that, all of the collected hand specimens are measured multiple times using ASD field spectrometer within the range between 350 nm and 2500 nm (Figure 4. 3).

The spectral curves of the samples were taken as reference data sets, where cross correlations were calculated between these and the corresponding pixels of the atmospherically corrected image data. Unfortunately, the number of image bands and the number of spectrometer wavelengths are not equal to each other. In order to compare them, one of them should be converted to the other. Therefore, at the beginning of the process, wavelength of reference spectra was reduced to wavelength of image channels. The idea of this process is also similar to the spectral subsetting of image data. Figure 4. 3, 4. 4, and 4. 5 illustrate 6 spectral curves which are

reference, raw image spectra, ACORN corrected image spectra, ATCOR2, ATCOR3, and FLAASH corrected image spectra (as red color) for each collected 15 samples (A1, A2, A3, A4, A6, A7, A8, A9, B2, B5, B10, B12, B13, B17, and B20 (Appendix D).

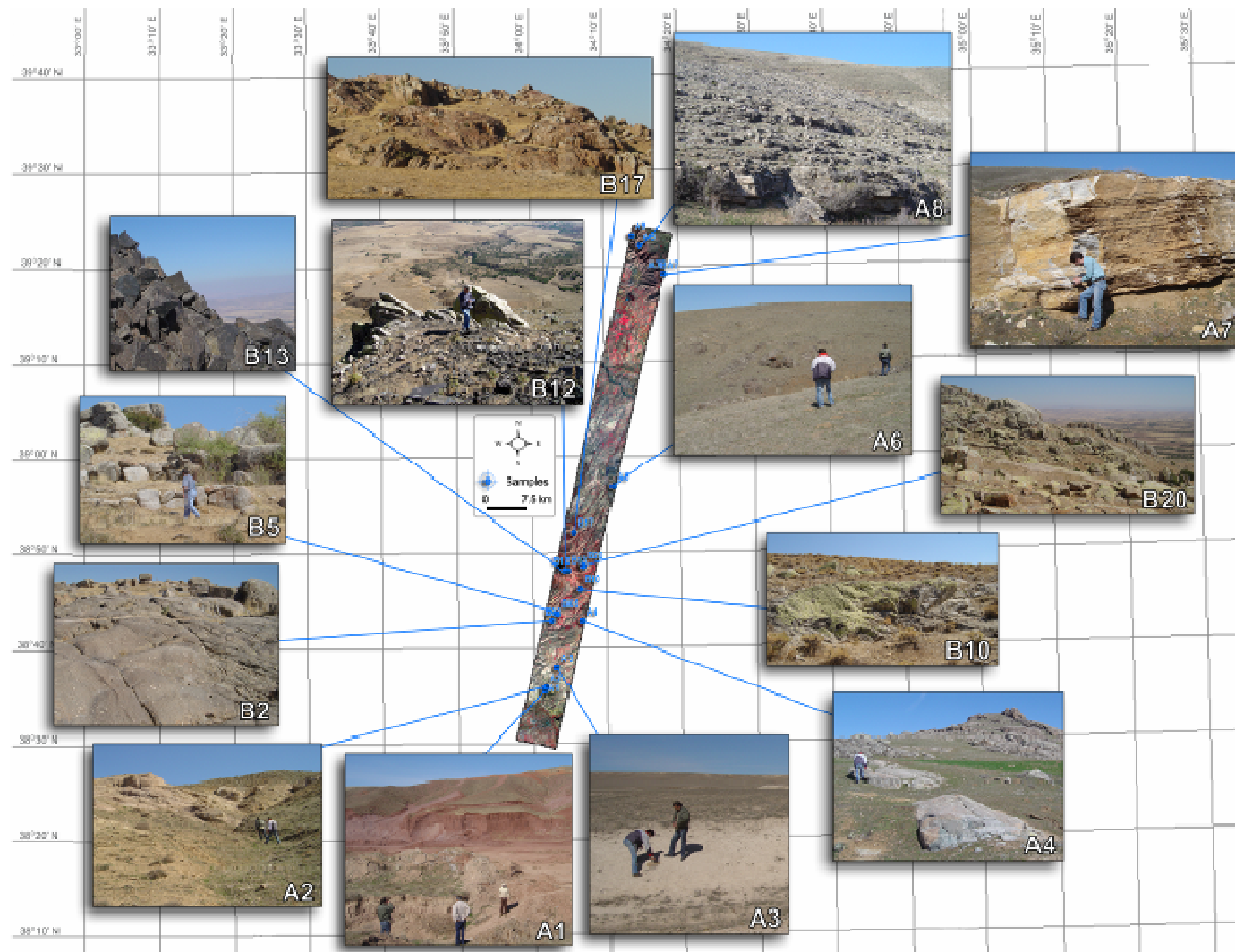


Figure 4. 2. Spectral samples collected from the field and Hyperion Image data for Ekecek test site.

As can be seen in Figure 4. 3, 4. 4., and 4. 5, the trend of the raw image spectrum and the other spectra are different from each other. The raw image spectrum is similar to radiant flux of the earth called "hull quotient" (Figure 2. 2). After the atmospheric correction process, hull-quotient effect is removed and then, absorption features can be clearly seen on the spectra. All atmospherically corrected and reference spectral curves of corresponding samples were normalized to range between 0 and 1 for appropriate comparison. Following this, all spectra were plotted on a plate with vertical shift for clear display (Figure 4. 3, 4. 4, and 4. 5).

According to Figure 4. 3, 4. 4. and 4. 5, all of the atmospheric correction modules successfully detect the absorption at 2200 nm as seen in reference spectra in sample A2. For sample A1 and A2; ATCOR2 and ATCOR3 are capable of discrimination for wavelength of 970 nm as seen in reference spectra (San and Suzen, 2007). Although digital elevation model (DEM) and geometric correction of data are required for the application of ATCOR3, the results of ATCOR2 and ATCOR3 are very similar to each other. Even though, FLAASH and ACORN also give similar results, only the suppression of water absorption bands in ACORN is wider than that of FLAASH.

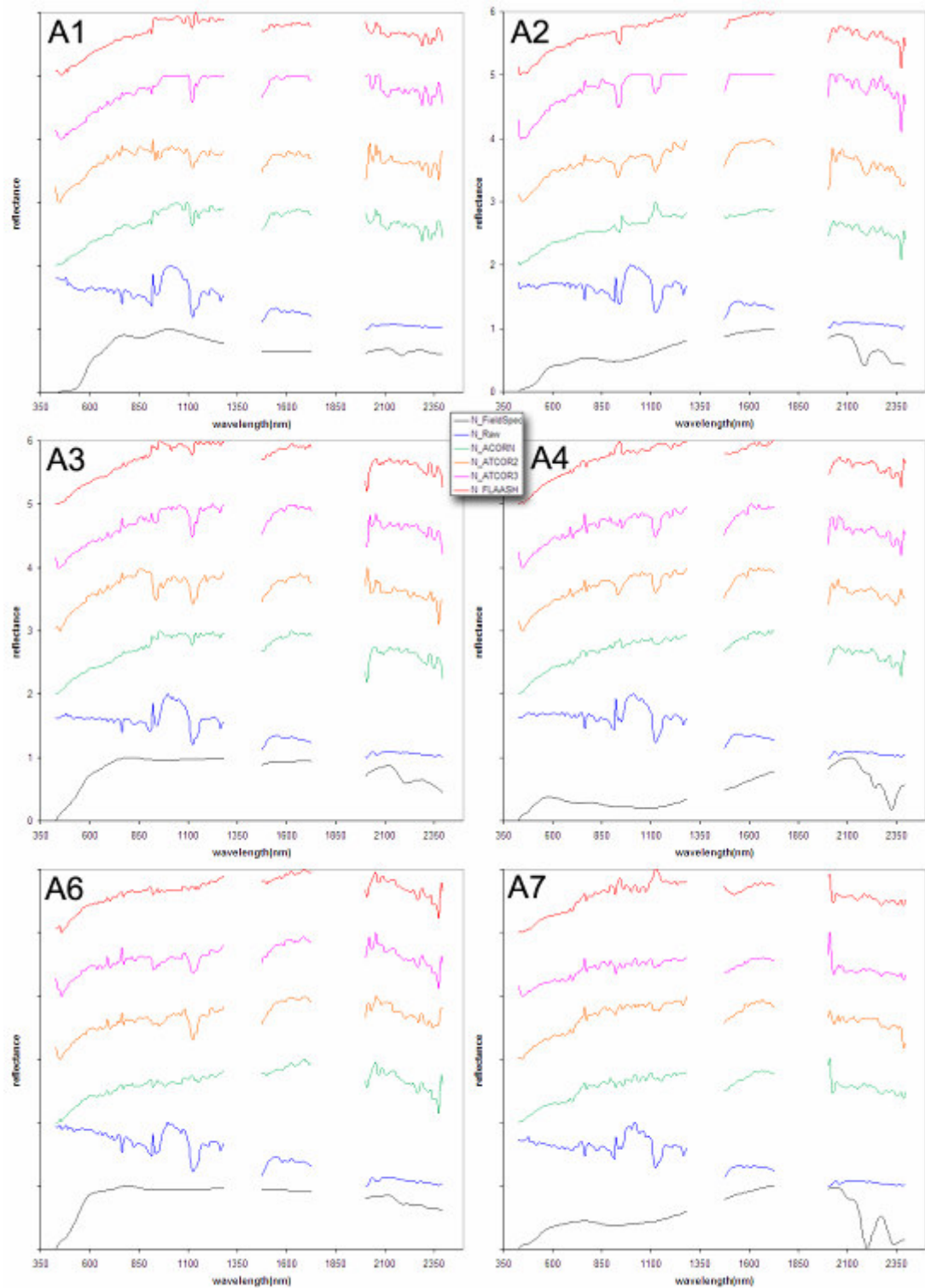


Figure 4. 3. Spectral curve of the samples A1, A2, A3, A4, A6 and A7 (Black: reference spectra, blue: raw image spectra, green: ACORN corrected image spectra, orange: ATCOR2 corrected image spectra, violet: ATCOR3 corrected image spectra, red: FLAAASH corrected image spectra)

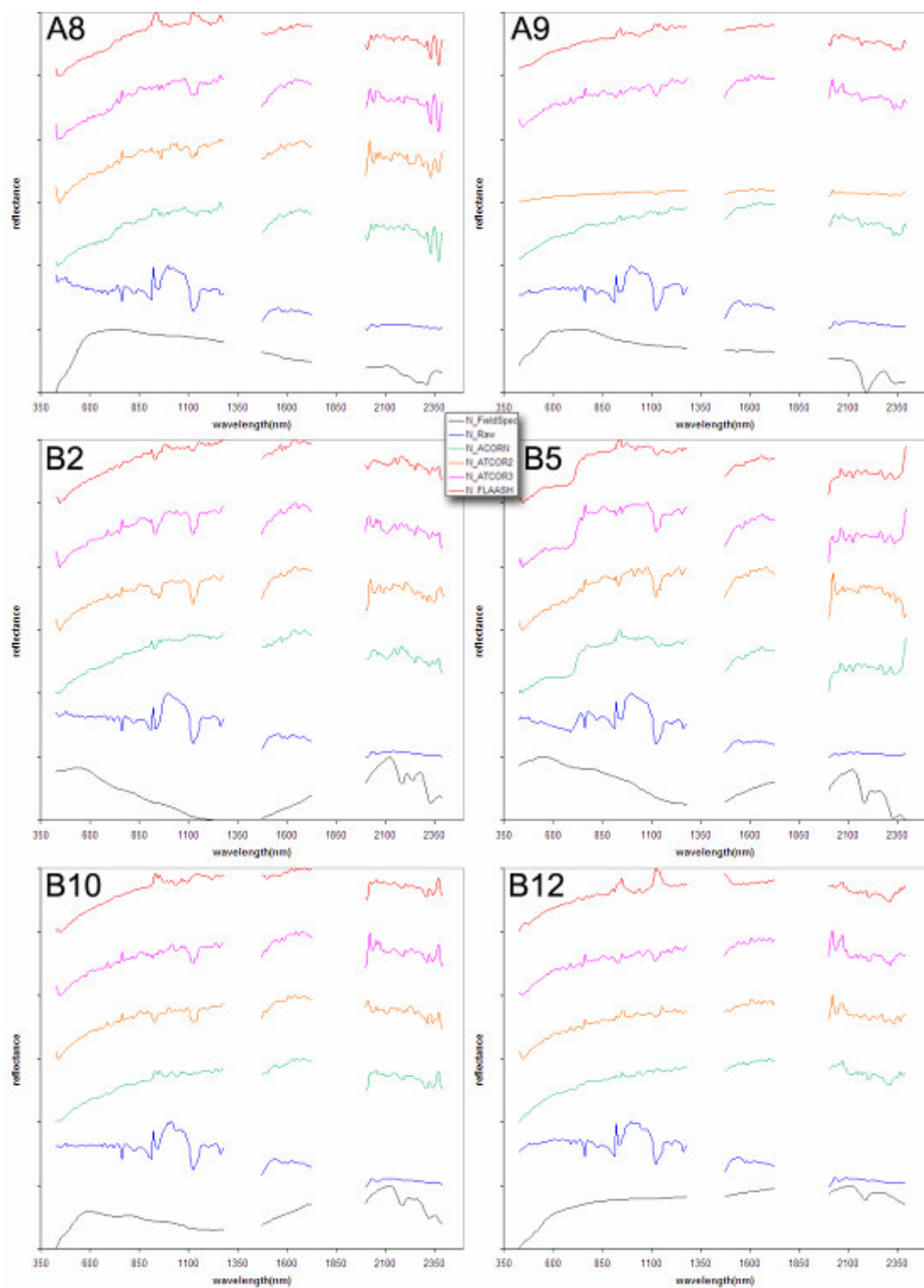


Figure 4. 4. Spectral curve of the samples A8, A9, B2, B5, B10 and B12 (Black: reference spectra, blue: raw image spectra, green: ACORN corrected image spectra, orange: ATCOR2 corrected image spectra, violet: ATCOR3 corrected image spectra, red: FLAAASH corrected image spectra)

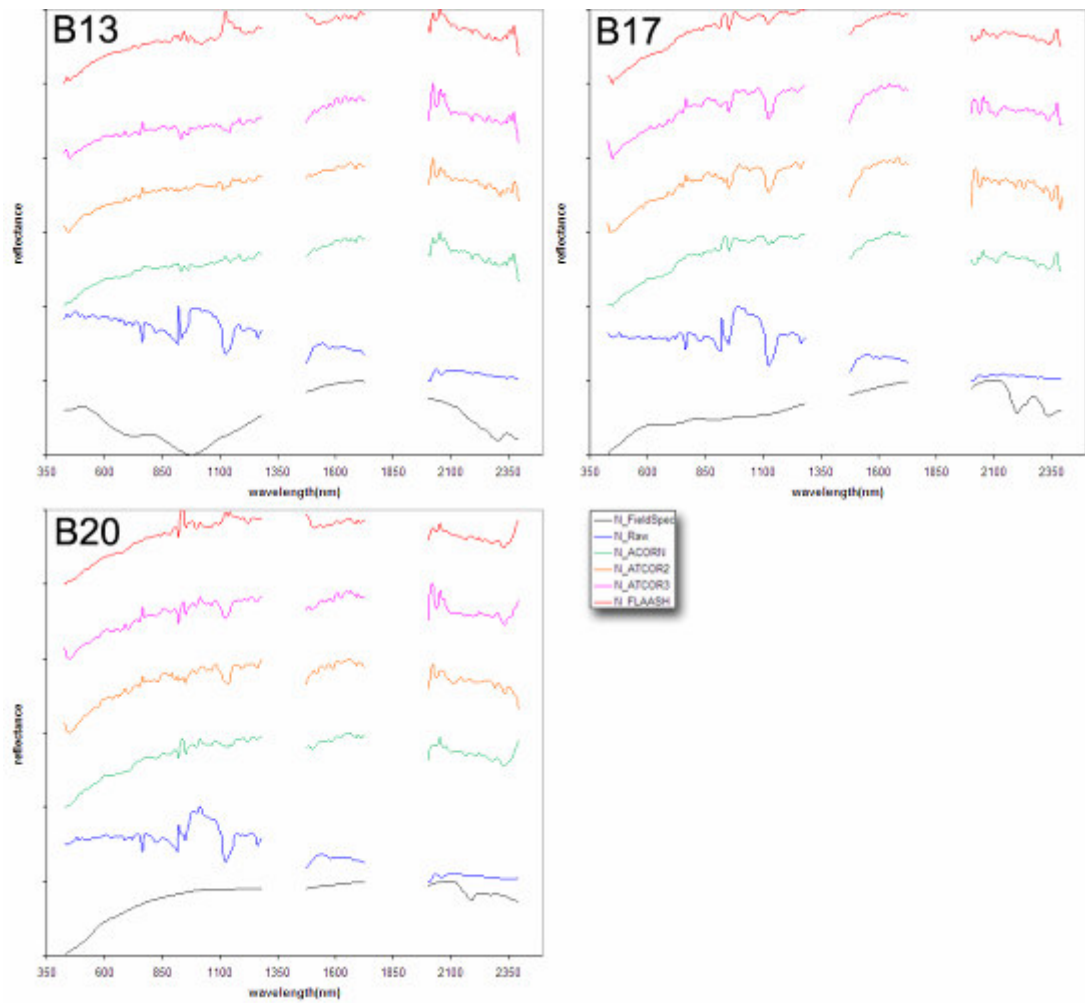


Figure 4. 5. Spectral curve of the samples B13, B17, and B20 (Black: reference spectra, blue: raw image spectra, green: ACORN corrected image spectra, orange: ATCOR2 corrected image spectra, violet: ATCOR3 corrected image spectra, red: FLAASH corrected image spectra)

When examining the spectral curves of the atmospherically corrected images and reference data, there exist different trends in the different wavelength regions. In order to achieve precise cross-correlations, different wavelength regions are evaluated separately for all wavelength region spectra and for divided portions of spectrum. The whole wavelength range between 426 nm and 2396 nm is divided into 3 sub-regions. The wavelength range between 426.82 nm and 1285.76 nm is defined as region 1, the wavelength range between 1477.43 nm and 1729.7 nm is described as region 2, and the

wavelength region 2002.06 nm and 2395.50 nm is identified as region 3. The correlation coefficients were computed for the specified wavelength regions and for whole spectrum which covers all the three specified regions. The computed correlation coefficients (r) of the field samples are given in Table 4. 1. The correlation coefficient approaching the value of 1, indicates that the correlation is perfect and the two data sets exactly fit to each other. Conversely, if the correlation coefficient is nearly equal to zero, the two data sets are not correlated to each other. The minimum and the maximum correlation coefficients are obtained as 0.00 and 0.97.

Table 4. 1. The correlation coefficient of samples for full wavelength spectrum and regions of spectrum. The maximum values are underlined.

Sample #	Full Region Correlation				Region 1 Correlation				Region 2 Correlation				Region 3 Correlation			
	AC	AT2	AT3	FL	AC	AT2	AT3	FL	AC	AT2	AT3	FL	AC	AT2	AT3	FL
A01	0.65	<u>0.75</u>	0.60	0.68	0.82	<u>0.91</u>	0.84	0.83	<u>0.64</u>	0.52	0.59	0.61	0.00	<u>0.05</u>	0.00	0.00
A02	0.74	0.73	0.67	<u>0.76</u>	0.87	0.90	0.83	<u>0.92</u>	<u>0.80</u>	0.66	0.29	<u>0.80</u>	<u>0.49</u>	0.42	0.48	0.47
A03	0.70	<u>0.75</u>	0.67	0.70	0.75	<u>0.83</u>	0.75	0.75	0.87	<u>0.93</u>	<u>0.93</u>	0.83	0.24	<u>0.34</u>	0.29	0.21
A04	<u>0.07</u>	0.04	0.06	0.03	0.01	<u>0.03</u>	<u>0.03</u>	0.01	0.82	0.66	0.67	<u>0.84</u>	<u>0.42</u>	0.41	0.37	0.39
A06	0.51	0.40	0.44	<u>0.55</u>	0.78	0.74	0.72	<u>0.80</u>	<u>0.69</u>	0.35	0.45	0.68	0.64	0.66	<u>0.70</u>	0.61
A07	<u>0.35</u>	0.29	0.33	0.26	<u>0.72</u>	0.70	0.69	0.66	<u>0.87</u>	0.77	0.83	0.65	0.19	<u>0.22</u>	0.19	0.15
A08	<u>0.16</u>	0.08	0.11	0.15	0.38	<u>0.45</u>	0.37	0.36	0.85	0.80	0.82	<u>0.87</u>	<u>0.06</u>	<u>0.06</u>	0.05	<u>0.06</u>
A09	0.00	0.00	<u>0.01</u>	<u>0.01</u>	0.00	0.01	<u>0.02</u>	0.00	0.34	0.19	0.18	<u>0.45</u>	0.49	0.17	<u>0.57</u>	0.47
B02	0.54	0.33	0.43	<u>0.55</u>	<u>0.91</u>	0.73	0.79	0.90	<u>0.76</u>	0.68	0.64	0.74	<u>0.39</u>	0.21	0.29	0.38
B05	0.13	0.16	0.12	<u>0.17</u>	0.54	<u>0.57</u>	0.47	0.55	<u>0.86</u>	0.78	0.81	<u>0.86</u>	0.04	<u>0.23</u>	0.03	0.05
B10	0.08	<u>0.14</u>	0.11	0.05	0.00	<u>0.01</u>	0.00	0.00	<u>0.81</u>	0.66	0.69	0.78	0.39	<u>0.52</u>	0.29	0.29
B12	<u>0.87</u>	0.85	0.81	0.75	<u>0.93</u>	0.92	<u>0.93</u>	0.86	<u>0.84</u>	0.72	0.73	0.05	0.19	<u>0.20</u>	0.13	0.05
B13	0.20	0.14	<u>0.28</u>	0.14	0.34	<u>0.38</u>	0.26	0.33	<u>0.91</u>	0.88	0.90	0.19	<u>0.68</u>	0.66	0.54	0.66
B17	0.37	<u>0.45</u>	0.40	0.34	<u>0.86</u>	<u>0.86</u>	0.82	<u>0.86</u>	<u>0.84</u>	0.70	0.72	0.82	0.20	<u>0.29</u>	0.25	0.15
B20	<u>0.89</u>	0.85	0.85	0.83	<u>0.97</u>	0.95	0.93	0.95	<u>0.80</u>	0.65	0.75	0.08	0.21	<u>0.44</u>	0.20	0.11

AC: ACORN corrected image, AT2: ATCOR2 corrected image, AT3: ATCOR3 corrected image, FL: FLAASH corrected image.

Figure 4. 6 shows the correlation values of each sample for whole spectrum. Each samples and correlation coefficients are located on the x-axis and y-axis, respectively on the graphic. As can be seen on this figure, sample A1, A2, A3, A6, B02, B12, and B20 have moderate to high correlations. On the

contrary, sample A4, A7, A8, A9, B5, B10, B13, and B17 have low to moderate correlations with the reference. Although some samples have low correlations, ACORN corrected samples have relatively high correlation comparing the corresponding competitor correction techniques on the same sample. Consequently, ACORN is quite successful for atmospheric correction of the Hyperion imagery according to the cross correlation results (San and Suzen, 2007).

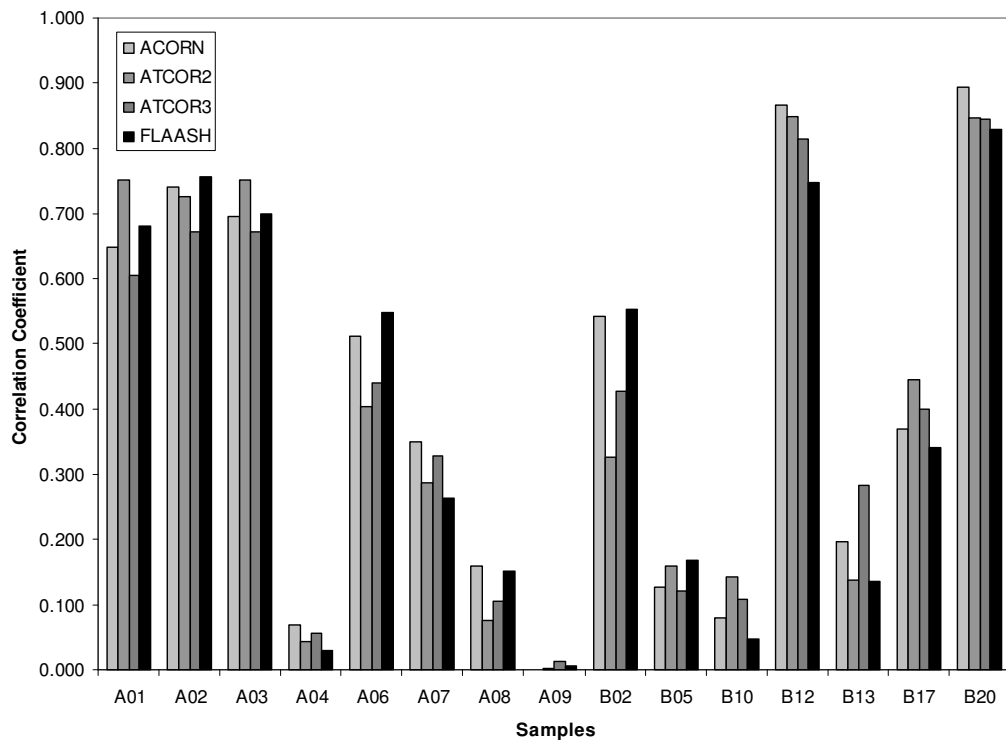


Figure 4. 6. Correlations of each sample between reference spectra and atmospherically corrected images for full wavelength range.

4. 5. 2. The Comparison between Image Data and Field Spectra Data for Each Atmospheric Correction Algorithms Using Absorption Wavelength

The comparisons of spectral curves of atmospherically corrected images and reference spectra in specific predefined regions are examined in previous section. In this section, only absorption wavelengths of the reference spectra are checked. If the absorption features of the corrected and reference spectra on the same wavelength positions are exactly the same, then the corrected spectra is considered to be used for further hyperspectral analyses.

Although the atmospherically corrected image spectra of collected samples seem to be quite similar, there are some differences between reference spectra and the atmospherically corrected image spectra. For sample A1 and A2 (Figure 4. 3), all atmospherically corrected data have absorption at the wavelength of 2150.7 nm as seen on reference spectra. At the wavelength of 2158.5 nm, the absorption feature is also clearly observed for all corrected data. Furthermore, all atmospheric correction algorithms minimize the effect of atmosphere and they show same features as the reference spectra features at wavelength of 1700 nm, 1652.35 nm and 2221.5 nm for sample B13, wavelength of 2152.5 nm, 2186.1 nm and 2230.8 nm for sample B10, wavelength of 1652.5 nm for sample B20 (Figure 4. 4 and 4. 5). On the contrary, all atmospheric correction algorithms failed at the wavelength of 2152.5 nm for sample B12, the wavelength of the sample A9, the wavelength of 2235.4 for sample A7. None of them shows the absorption feature like in the reference spectra for those wavelength regions.

When a major absorption wavelength feature of reference spectra is observed, related atmospheric correction technique is considered as successful. In other words, if the wavelength position of the absorption features coincides to reference spectra, then the used correction technique matches properly for that sample. Table 4. 2 shows the absorption wavelengths of the reference spectral samples and corresponding

wavelength locations of four atmospheric correction techniques. If the absorption wavelength position is in the correct location for the atmospheric correction, then it is marked as “1” on Table 4. 2. Similarly, if there is no any consistency, then “0” is written on the table.

Table 4. 2. The main absorption wavelength of the reference spectra and the comparison of the corresponding region of atmospherically corrected image spectra. Blue shows all the correction techniques are correctly detected and the red shows none of the atmospheric correction techniques detected the absorption wavelength.

Sample	wavelength (nm)	ACORN	ATCOR2	ATCOR3	FLAASH
A1	2150.70	1	1	1	1
A2	2150.70	1	1	1	1
A3	2158.50	1	1	1	1
A4	2187.75	0	0	0	0
	1482.30	1	0	0	0
	2232.30	0	0	1	1
A6	1482.30	1	0	0	1
	1600.00	1	0	0	1
	2150.70	1	0	1	1
A7	2155.35	1	0	1	0
	2235.45	0	0	0	0
A8	2224.65	1	0	1	1
A9	2155.35	0	0	0	0
	2235.45	1	0	1	1
B2	2150.70	0	1	0	0
	2187.75	1	0	1	1
	2235.45	1	0	0	0
B5	2147.70	1	0	1	1
B10	1482.30	1	0	0	1
	2152.50	1	1	1	1
	2186.10	1	1	1	1
	2230.80	1	1	1	1
B12	1482.30	1	0	0	0
	2152.50	0	0	0	0
B13	1700.00	1	1	1	1
	2221.50	1	1	1	1
	2239.99	1	0	0	0
	1439.70	1	0	0	0
	1652.35	1	1	1	1
B17	2160.00	1	1	0	0
	2240.00	1	0	1	1
B20	1482.30	1	0	0	0
	1652.50	1	1	1	1
	2152.50	0	0	1	0
	2201.65	1	0	1	1
Total		28	12	20	21
(%)		75.68	32.43	54.05	56.76

According to the absorption feature of the reference spectra, all the atmospheric correction algorithms are clearly distinguish absorptions of the sample A1, A2, A3, and some absorption wavelengths of sample B10, B13, B20. On the contrary, some of the absorption wavelengths of sample A4, A7, A9, and B12 can not be identified correctly as an absorption by the atmospheric correction algorithms. Table 4. 2 summarizes the comparison of the absorption wavelengths between the reference and atmospherically corrected image spectra. As a result of the comparison, ACORN can detect the 28 absorption features correctly out of total 35 absorption features on 15 different samples. FLAASH, ATCOR3, and ATCOR2 can detect only 21, 20, and 12 absorption features, respectively. Based on these results ACORN is the most successful atmospheric correction method among the four on the study area of Ekecek.

4. 6. Choosing the Optimum Atmospheric Correction Technique

When comparing the atmospheric correction techniques on the Ekecek study area, only ATCOR3 uses digital elevation model (DEM) for atmospheric correction. Although theoretically including DEM in atmospheric correction seems to be a powerful technique, not always a detailed DEM would be available (San and Suzen, 2007), hence the usage of other techniques is indispensable. Another conceptual problem is that there are no any perfect atmospheric correction technique present. This is because, the atmosphere can not be modeled as much detailed as the acquired image data at the same time. According to this statement, the appropriate atmospheric correction technique should be selected using the techniques of absorption wavelength feature comparisons and cross correlations with the field sample spectra. The result of these comparisons would let the user to decide best atmospheric correction technique for the case area. However, sometimes it is difficult to get different atmospheric correction modules due to greater costs.

The results of the cross correlations between the atmospherically corrected data and reference spectra show that ACORN is quite successful over the other atmospheric corrections. Similarly, in the comparison of the absorption wavelengths, almost 76 % accuracy which is the highest amount is obtained for detecting the absorption wavelengths using ACORN. Therefore, ACORN will be used as an atmospheric correction for the further image processing stages.

4. 7. Bad Band Removal

The bad band removal operation is almost the same operation of removal of water absorption bands. However, bands which have noise or no data (null value) due to suppression by the atmospheric correction algorithm are eliminated in this time. All atmospheric correction modules suppress the water and aerosol absorption wavelength regions. Unfortunately, they use different algorithms inside and the width of the suppressed wavelength regions are not the same for all. Therefore, suppressed bands which have null or zero value should be eliminated before minimum noise fraction (MNF) transformation. Otherwise, all the transformed channel results would be equal to null value.

After the comparison of atmospheric correction techniques, ACORN is selected as more successful correction technique for the test site of Ekecek. Then, bands 1 to 2, 50 to 52, 87 to 105, 131 to 158, and 194 to 196 are eliminated due to containing of noise and null values. Therefore, total 141 image bands are left valid for MNF transformation and the rest of the image processing operations.

CHAPTER 5

CROSS TRACK ILLUMINATION CORRECTION

This chapter contains application of minimum noise fraction transformation (MNF) and cross track illumination correction (CTIC). Furthermore, the effects of cross track illumination on image processing results are explained in detail.

5. 1. Minimum Noise Fraction (MNF) Transformation

Minimum Noise Fraction (MNF) transformation is one of the most used and powerful processing steps for hyperspectral image classification. It is similar to Principle Component Analysis (PCA) which performs a transformation that recognizes maximum variance in multi dimensional space (Sabins 1997). It is mainly used for data dimension reduction and it does not deal with noise or target signal of interest in case of detection applications (Farrell, 2005). The first component of PCA has the highest variance of the data. Green et. al., (1988) found that PCA does not always produce images that illustrate gradually decreasing image quality with increasing component number.

Green et. al., (1988) developed the maximum noise fraction (MNF) transform as a method for ordering components in terms of image quality. Some of the researchers used the term “noise-adjusted principle component (NAPC)”

instead of MNF (Chang, 2003). Minimum/Maximum Noise Fraction (MNF) or noise-adjusted principle component analysis is a modification of PCA approach based on to the maximization of the S/N ratio (Chang, 1999). Owing to the unequal noise variances gained in different bands, the real S/N ratio in the image bands do not reflect the variance of the data components. It is not a rule that band with small variance has poor image quality and it is possible to have a high S/N ratio compared to other bands with large variances but low S/N ratio's (Chang, 1999).

MNF denoted as minimum noise fraction which follows a series of processing steps. The first step, an estimated noise covariance matrix is produced using image channels separately and the noise in the data is de-correlated and rescaled. The next step, an ordinary PCA transformation is applied to noise-whitened data (noise-free data) (ENVI User's Guide, 2001). At the end of the MNF transformation, new transformed channels arranged as series of bands from the least amount of noise to high amount of noise.

After the MNF transformation, transformed data is divided into two parts: one of them contains large eigen values with coherent eigen images, and the other part has a complementary part with near-unity eigen values and noise-dominant images. The noise is separated from the data using coherent part which contains large eigen values (ENVI User's Guide, 2001).

Figure 5. 1 shows the MNF eigen value bands after transformation of Ekecek image. The noise can not be observed as a salt and pepper effect in the first ten MNF bands. As can be seen in the Figure 5. 2, eigen values approaches to value of 2 beyond the first 20 MNF bands. The break point of the graphic defines threshold value for the noisy part of data (B), which indicates that the first 20 MNF bands have less amount of noise. Beyond MNF band 20, the eigen value distribution is nearly becoming constant as being parallel to the horizontal axis. Therefore, the first 20 MNF bands, as input data, are

considered suitable and noise free for classification. The computed statistics of MNF transformation is given on Table 5. 1.

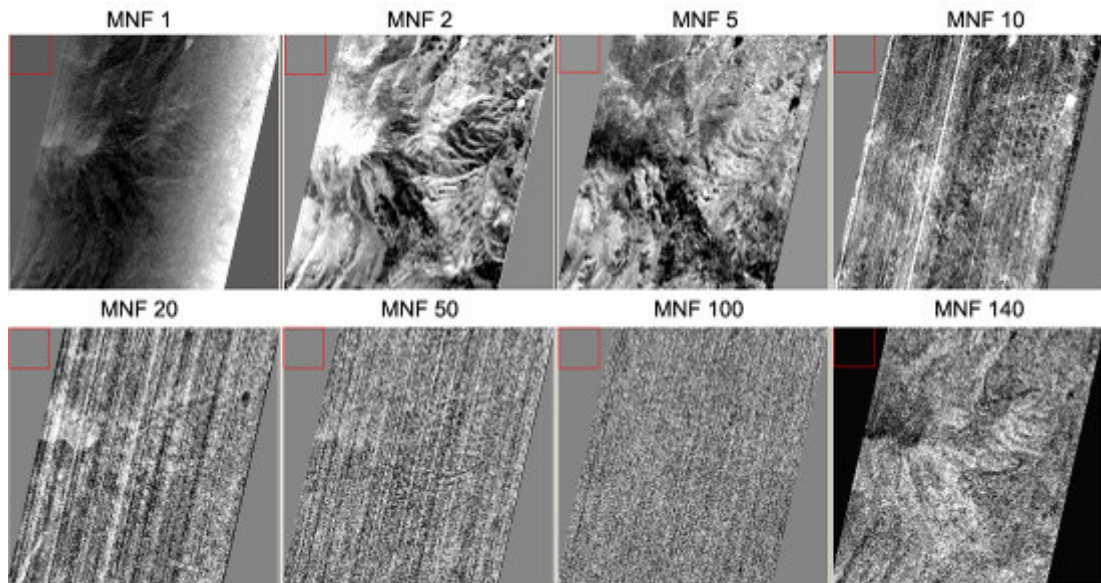


Figure 5. 1. MNF eigen value bands of The ACORN corrected Ekecek image

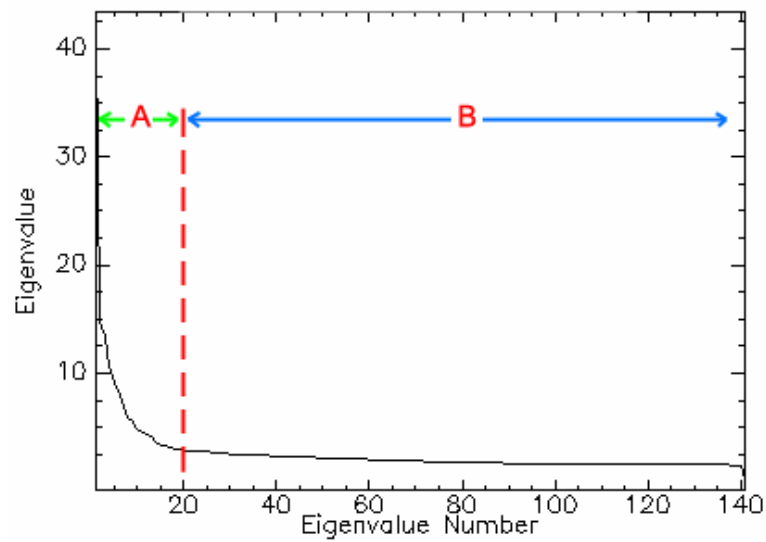


Figure 5. 2. Graphical representation of the eigen values versus eigen numbers for the ACORN corrected image for Ekecek test site. A region shows high eigen indicating mainly image data and B region shows low eigen values indicating possible noise.

Table 5. 1. Eigen values of MNF transformation (no CTIC applied)

No	Eigenvalue	No	Eigenvalue	No	Eigenvalue	No	Eigenvalue
1	42.454584	36	2.399456	71	1.852248	106	1.576100
2	14.767761	37	2.384760	72	1.831689	107	1.572864
3	13.427542	38	2.360224	73	1.811661	108	1.571906
4	10.657036	39	2.338440	74	1.805978	109	1.566645
5	9.090603	40	2.332887	75	1.791668	110	1.561022
6	8.371349	41	2.309600	76	1.776429	111	1.557769
7	6.975503	42	2.286822	77	1.771951	112	1.555761
8	5.879650	43	2.270958	78	1.761444	113	1.552808
9	5.597399	44	2.253672	79	1.754987	114	1.550976
10	4.867516	45	2.236247	80	1.737415	115	1.550192
11	4.435145	46	2.225476	81	1.728770	116	1.546545
12	4.362691	47	2.215878	82	1.719600	117	1.545659
13	4.197066	48	2.197600	83	1.713590	118	1.542405
14	3.712991	49	2.166757	84	1.702534	119	1.536793
15	3.348054	50	2.164137	85	1.698314	120	1.535969
16	3.244018	51	2.147453	86	1.695052	121	1.534915
17	3.113247	52	2.126082	87	1.688099	122	1.533272
18	3.014141	53	2.109334	88	1.676918	123	1.531200
19	2.964550	54	2.093247	89	1.666450	124	1.530523
20	2.856371	55	2.085932	90	1.663288	125	1.526201
21	2.842194	56	2.076856	91	1.661312	126	1.522390
22	2.803528	57	2.059321	92	1.655125	127	1.521976
23	2.772486	58	2.047924	93	1.643923	128	1.519205
24	2.738918	59	2.016475	94	1.632022	129	1.517074
25	2.705350	60	2.008278	95	1.621527	130	1.514453
26	2.634287	61	2.004324	96	1.620412	131	1.513051
27	2.604884	62	1.987406	97	1.614231	132	1.510203
28	2.591672	63	1.978267	98	1.609054	133	1.508042
29	2.535194	64	1.962801	99	1.605716	134	1.506210
30	2.515598	65	1.945260	100	1.598121	135	1.504487
31	2.507558	66	1.929121	101	1.593479	136	1.501667
32	2.455544	67	1.906430	102	1.589527	137	1.500101
33	2.447089	68	1.893460	103	1.586755	138	1.493943
34	2.426180	69	1.878601	104	1.585174	139	1.491411
35	2.414439	70	1.866279	105	1.581695	140	1.488245
						141	0.202592

In Table 5. 1, first eigen value is seen as 42.45 and the eigen values decrease to 0.20 for the last MNF component. As the MNF component number increases, the eigen value decreases.

It is clearly observed that, after MNF transformation of ACORN corrected image, there exist an almost E-W trend which is perpendicular to the flight direction in the first MNF component in the Figure 5. 1.

5. 2. The Cross Track Illumination Correction (CTIC) / Spectral Smile Correction

All Hyperion image data has smile effect with varying degree which is caused by the change of dispersion angle with target position and it is associated with an across-track wavelength shift from center wavelength (Goodenough et. al., 2003). Datt et. al. (2003) stated that smile effect is occurring due to low-frequency array outcomes which are likely to be expected to happen in Hyperion data that was already observed before the launch of Hyperion.

Although smile effect can not be observed visually in the individual image bands, after application of Minimum Noise Fraction (MNF) transformation smile effect can be seen visually in the eigen value images (Goodenough et. al., 2003 and Datt et. al. 2003). While smile effect is detected on EO-1 Hyperion data; on the contrary, there is no any smile effect in AVIRIS data (Goodenough et. al., 2003). In order to remove this effect, Goodenough et. al., (2003) applied moving linear fitting and interpolation using AVIRIS data with the simulated smile effect. As a result of their studies the spectral smile of Hyperion data is reduced; however, it is not removed completely.

In our study, after MNF transformation of ACORN corrected image for Ekecek test site, smile effect is observed as a definite trend in the first eigen value component (Figure 5. 3). This observed trend is similar to the trend present in cross track radar images. Signal power is reduced away from the radar antenna resulting in a trend observable on the image scene. Before starting to any image processing step this error should be corrected, as it would definitely add uncontrolled bias to the results. Therefore, smile or cross-track illumination effect should be reduced; hence in this study cross-track illumination correction (CTIC) module of ENVI image processing software was used. In the most important MNF components which are component 1 and 2, cross-track illumination is clearly detected as the first and second order polynomial functions, respectively (Figure 5. 4).

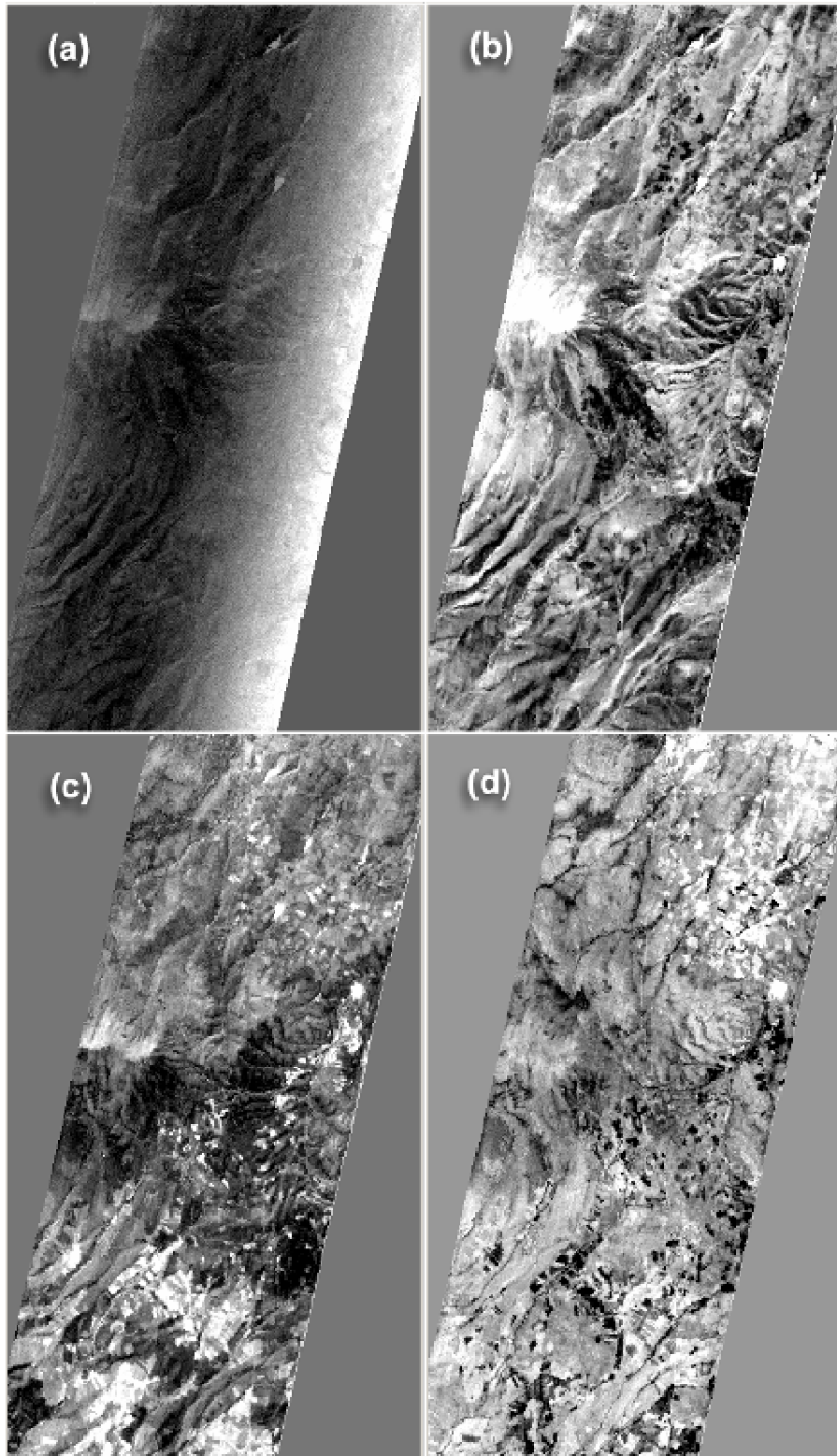


Figure 5. 3. ACORN corrected image for Ekecek test site; the first MNF component (a), the second MNF component (b), the third MNF component (c), and the forth MNF component (d).

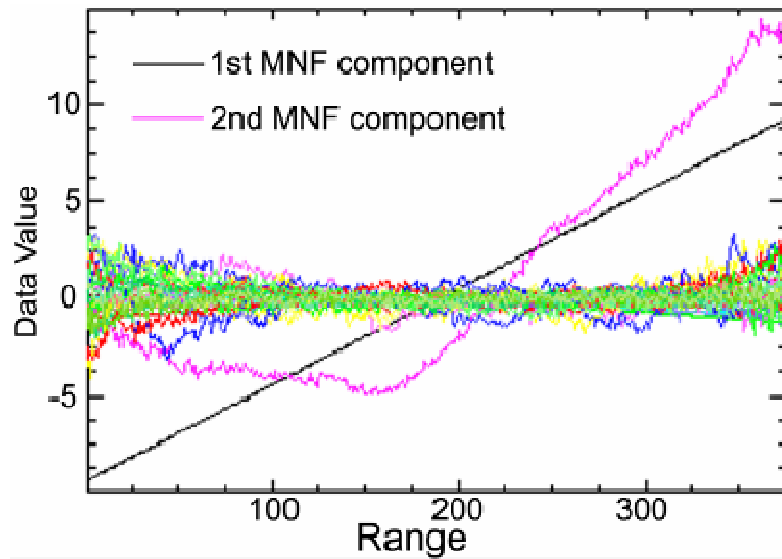


Figure 5. 4. Cross-Track Illumination of MNF which transformed from whole image channels.

During smile effect removal, at first, the average value for each column of individual bands was calculated. Then, the best fit line or the best fit non-linear polynomial functions for each band were generated by the CTIC algorithm. After that obtained polynomial functions are applied to pixels for each individual band. Finally, original DN values are converted to new DN values. In this step, new values are calculated by adding the difference between computed values and original DNs or by multiplying the ratio of computed values to original DNs.

As mentioned before, the best tool for observation of smile effect is MNF transformation. Therefore, MNF is used to test if the smile effect is removed or not. Figure 5. 5 shows the removal process of smile effect on the first component of MNF data. Each time, CTIC is applied to original data with the different degree of polynomial correction.

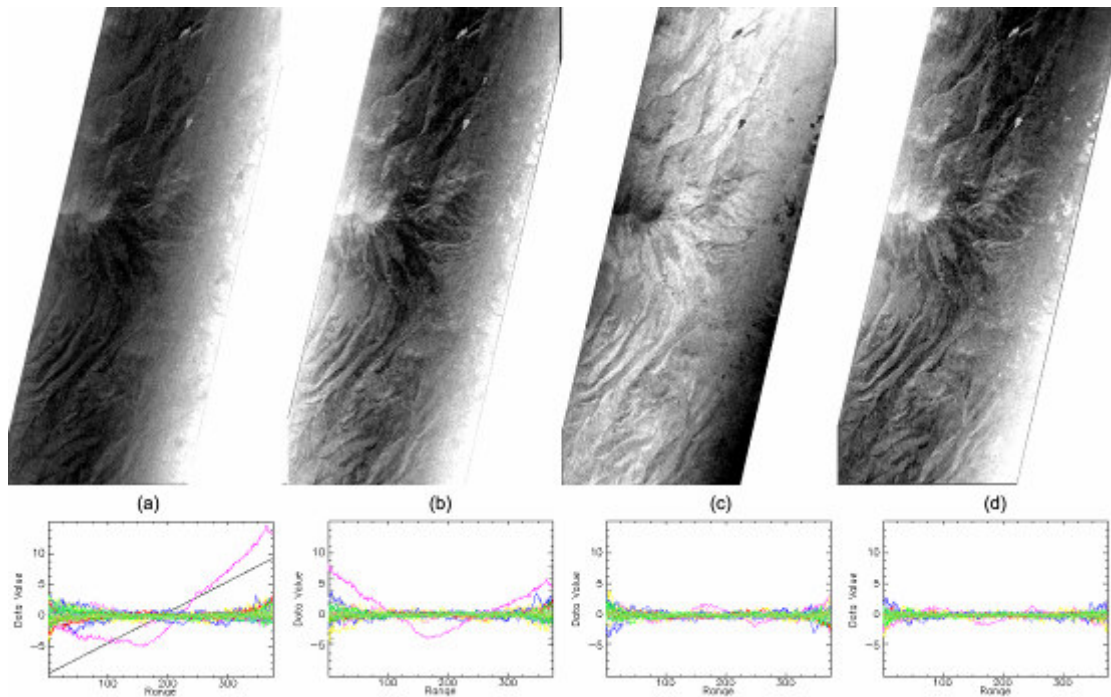


Figure 5. 5. The first MNF component with varying degrees of CTIC correction. (a) MNF with no CTIC applied data, (b) MNF of the first order CTIC, (c) MNF of the second order CTIC, and (d) MNF of the third order CTIC.

In order to keep the data as close as to the original form, data is tested using MNF transformation to find any existing smile effect. If the smile effect exists, then the polynomial order of CTIC is increased as one order and the data is tested again by both displaying the first MNF channel and graphical representation. This process continues up to no or little smile effect is observed.

In order to assess the magnitude, smile effect was also investigated separately in Visible-Near Infrared (VNIR) and Short Wave Infrared (SWIR) spectral band groups. In this case, MNF transformation was applied to VNIR bands and SWIR bands separately and then, smile effects were checked. Figure 5. 6 shows the raw MNF bands, the first, the second, and the third order CTIC applied MNF bands. It is seen that smile effect is clearly observed on VNIR image bands. Even though smile effect is not obviously

seen in raw MNF of SWIR channels, it is minimized after the third order correction (Figure 5. 6 (h)).

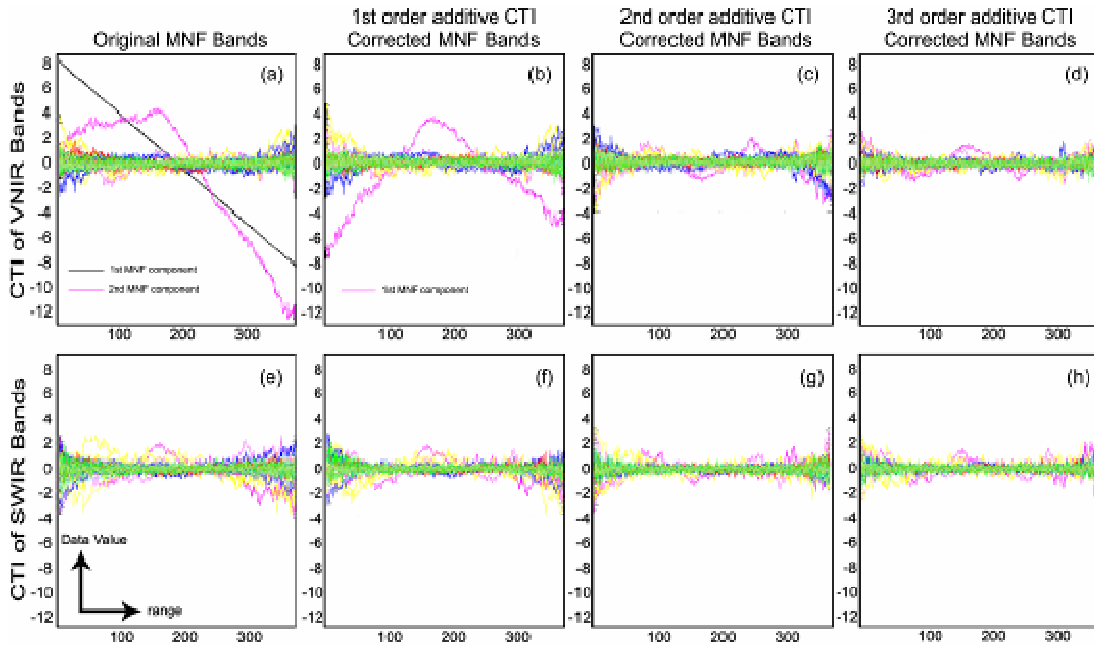


Figure 5. 6. Cross-Track Illumination (CTI) of MNF images. (a), (b), (c) and (d) are MNF of VNIR bands for no CTI Correction, first order additive CTIC, second order additive CTIC, and third order additive CTIC, respectively. (e), (f), (g) and (h) are MNF of SWIR bands for no CTI Correction, first order additive CTIC, second order additive CTIC, and third order additive CTIC, respectively.

Table 5. 2 shows eigen values of the MNF transformation after third order polynomial CTIC applied data. The eigen values are changed comparing before and after CTIC application. For example, the first MNF eigen value is changed from 42.45 to 19.77 and the last eigen value is changed from 0.20 to 0.19. Before CTIC, there is a huge difference between the first eigen value and the other eigen values. However, after the third order CTIC, the eigen value differences getting smaller.

Table 5. 2. Eigen values of MNF transformation (third order CTIC) for Ekecek Image data.

No	Eigenvalue	No	Eigenvalue	No	Eigenvalue	No	Eigenvalue
1	19.771871	36	2.398746	71	1.849824	106	1.576136
2	14.437028	37	2.384321	72	1.829713	107	1.572431
3	13.317330	38	2.339402	73	1.810804	108	1.571968
4	10.140044	39	2.332073	74	1.805026	109	1.564133
5	8.660659	40	2.326088	75	1.791257	110	1.560845
6	8.049659	41	2.301283	76	1.774055	111	1.557391
7	6.186183	42	2.265460	77	1.770136	112	1.554806
8	5.771650	43	2.262617	78	1.756806	113	1.552244
9	5.294467	44	2.239455	79	1.755424	114	1.550612
10	4.727502	45	2.225886	80	1.733717	115	1.549402
11	4.364748	46	2.221804	81	1.728085	116	1.546979
12	4.202271	47	2.207926	82	1.717954	117	1.545481
13	4.073969	48	2.182796	83	1.711953	118	1.541151
14	3.320345	49	2.164842	84	1.701561	119	1.537139
15	3.211950	50	2.160860	85	1.695673	120	1.536095
16	3.148029	51	2.146997	86	1.689915	121	1.535006
17	3.103194	52	2.107318	87	1.683937	122	1.533486
18	2.978616	53	2.098768	88	1.676449	123	1.530524
19	2.914712	54	2.093369	89	1.665409	124	1.530251
20	2.855672	55	2.078234	90	1.663076	125	1.526244
21	2.815893	56	2.075949	91	1.658970	126	1.522550
22	2.774721	57	2.057196	92	1.654542	127	1.521655
23	2.741204	58	2.035589	93	1.644157	128	1.519161
24	2.710380	59	2.011698	94	1.629498	129	1.515571
25	2.664607	60	2.001509	95	1.621284	130	1.514424
26	2.631750	61	1.987947	96	1.619239	131	1.513029
27	2.599829	62	1.985882	97	1.614104	132	1.510771
28	2.587305	63	1.971692	98	1.607937	133	1.506989
29	2.518988	64	1.956344	99	1.602151	134	1.506143
30	2.511767	65	1.943742	100	1.596860	135	1.504570
31	2.474101	66	1.927464	101	1.593412	136	1.501800
32	2.446675	67	1.904394	102	1.588695	137	1.500501
33	2.433784	68	1.889317	103	1.586057	138	1.494005
34	2.421060	69	1.877648	104	1.583536	139	1.491284
35	2.405803	70	1.859134	105	1.581027	140	1.488593
						141	0.199364

5. 3. The Cross Track Illumination Effect on SAM Rule Images

Previous sections, existence of cross track illuminations and its degree on Hyperion data sets are investigated. In this section, the effect of cross track illumination is given on the SAM rule images. In order to check this effect, Biga image is selected. This is because, Biga test site contains mainly mono mineralic outcrops and it is easy to compare endmembers from spectral library.

Similarly, cross-track illumination effect is detected on the Biga image data using MNF transformations. In order to remove smile effect on Spectral Angle Mapper (SAM) rule images, second order CTIC is applied on Biga image (Figure 5. 7).

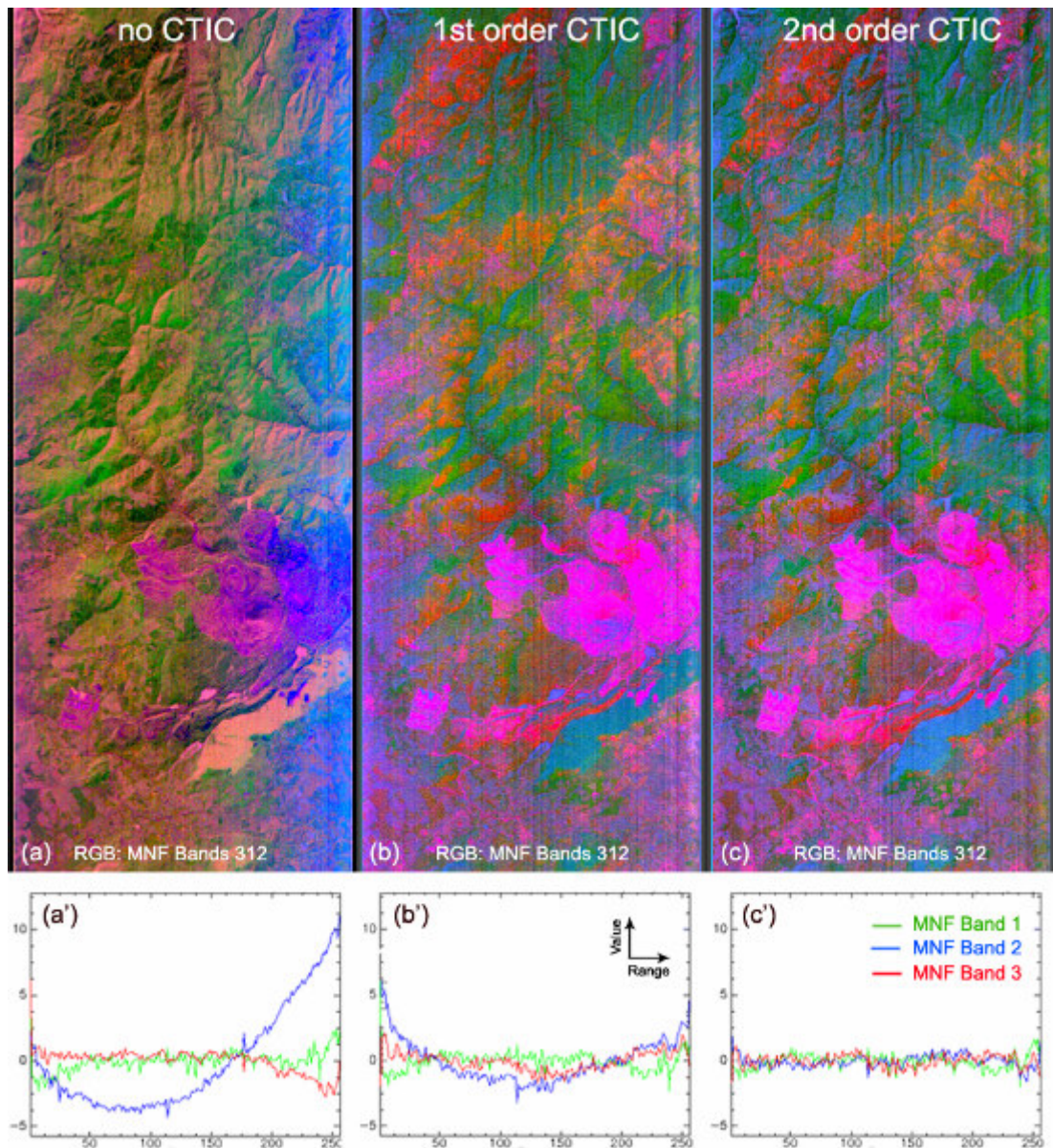


Figure 5. 7. RGB color composite representation of MNF bands of no CTIC applied (a), first order CTIC applied (b), second order CTIC applied (c) for Biga image.

The SAM rule images give the radians values of related samples. Negative rule images are computed with the multiplication of the original rule image by -1, and then the rule image can be seen more meaningful due to brightest pixels shows the highest possibilities of relevant sample. Figure 5. 8 and Figure 5. 9 shows the negative rule images of no CTIC, second order CTIC applied data and difference of them for all collected samples from field of Biga test site.

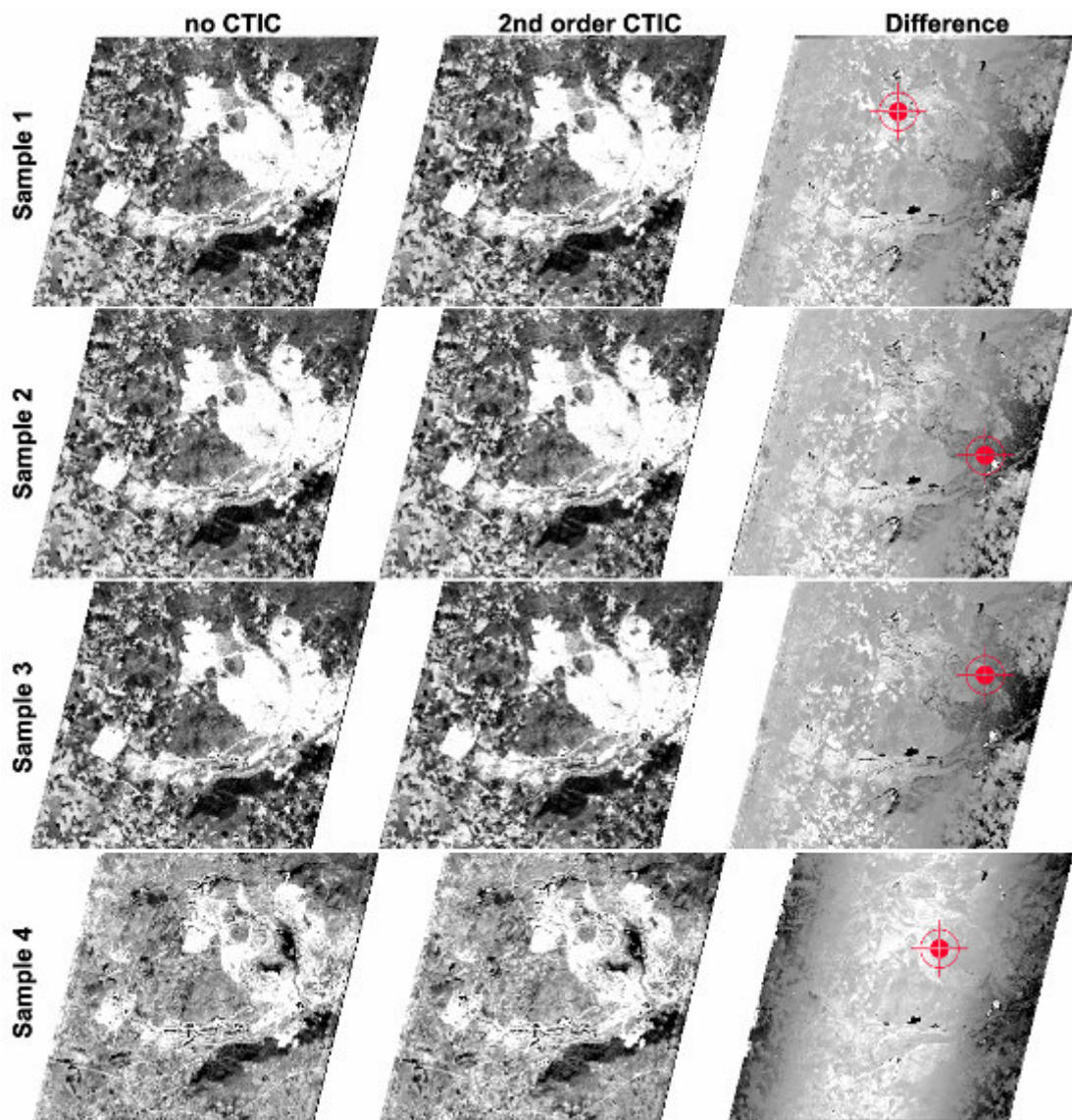


Figure 5. 8. Negative rule images of field samples (1 - 4) are generated from no CTIC applied and second order CTIC applied images, and the differences of them with the location of samples.

After CTIC application, computed rule images are changed. It is difficult to recognize by visually for the difference of rule images. However, in order to emphasize the difference between before and after CTIC application on the rule images, the subtraction of rule images which are before and after CTIC application is carried out and then smile effect is clearly observed as an existing trend on the rule image data. This trend directly affects the resultant data as it is composed of rule image data which is also affected by trend.

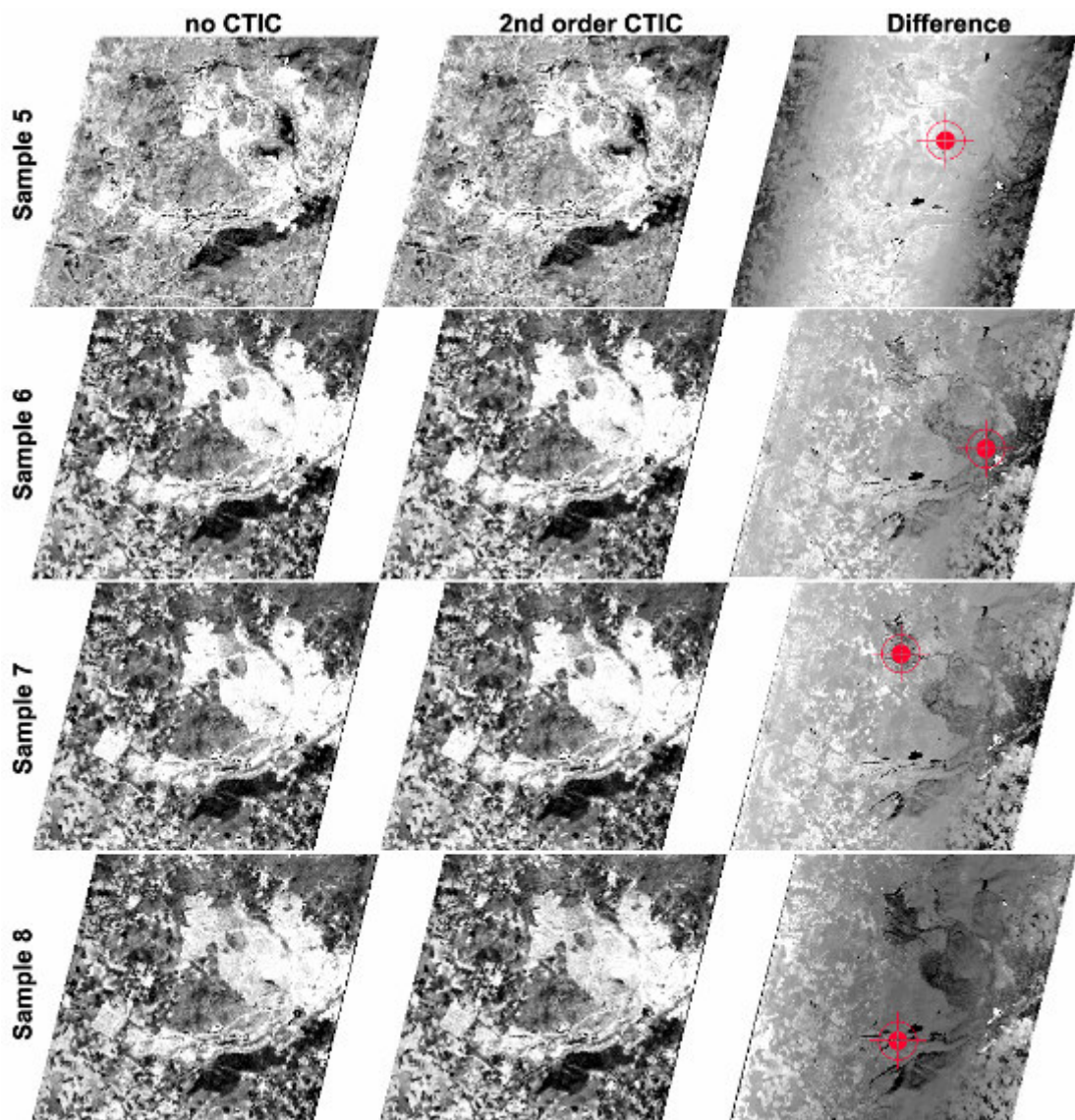


Figure 5. 9. Negative rule images of field samples (5 - 8) are generated from no CTIC applied and second order CTIC applied images, and the differences of them with the location of samples.

Therefore, as mentioned before, CTIC is the necessary process for increasing the accuracy of the classification and for minimizing the degree of misclassification in hyperspectral data classification.

CHAPTER 6

RESULTS AND DISCUSSIONS

In this chapter, the results of the hyperspectral image processing and analysis are presented and discussed. First, the atmospheric correction techniques are discussed in detail and next, the results of classification for Ekecek Image and its process steps are provided. Then, the results of Biga Image are given and processes are explained. In addition, the application of Spectral Mixture Analysis (SMA) is given for Biga test site. Finally, they are compared in terms of their applications and accuracies.

6. 1. CTIC Effect of Hyperspectral Thematic Mapping

In hyperspectral image classification, unlike multispectral case, classification deals with the numerous image bands. However, there exists high correlation among the adjacent image channels (Chen and Wang, (2007), Kumar et. al., (2001)). Figure 6. 1 shows the correlation obtained from image channels of AVIRIS (Airborne Visible/Infrared Imaging Spectrometer) data. In the figure, the bright and dark colors indicate the highest correlation (1 or -1) and the lowest correlation (0), respectively.

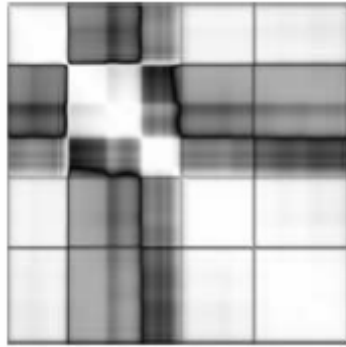


Figure 6. 1. Band correlation image generated from the experimental data of AVIRIS image, (Chen and Wang, 2007). The horizontal and the vertical axes show the bands of AVIRIS data.

Due to presence of high correlation between the adjacent image bands in hyperspectral data, large amount of redundant information in image channels are observed. Therefore, the application of MNF transformation not only reduces redundancies but also reduces the amount of noise in Hyperspectral data.

In hyperspectral imaging literature, image classification is generally performed by the following sequence of processes which are atmospheric correction, MNF transformation (Echtler, et. al., (2003), Kruse et. al., (2003)), pixel purity index (PPI) (Boardman, et. al., (1995), Chang, (2006), Kruse et. al., (2003)), or using spectral samples, and finally classification. There are different kinds of classification techniques used in hyperspectral imaging which are Mixture-Tuned Matched Filtering (Hubbard et. al., (2003), Yu et. al., (1993), Glenn et. al. (2005)), Neural Network Classification (Benediktsson et. al., (1995)), probability density function (Cetin et. al. (1993), and Cetin and Levandowski (1991)), Spectral Angle Mapper (Keshava, (2003), Echtler, et. al. (2003), Kruse, et. al. (1993.a.), Robila, (2005), Kruse et. al., (2003)).

In order to apply the classification sequence, proper end-members should be selected. The proper end-member is mainly uniform rock unit and it should

not contain mixtures of different classes. Field samples can be used as powerful end-members but, it is difficult to correlate field samples with the 30 by 30 m pixel of Hyperion image. Because of the mentioned obstacles above, data driven methods were used for image classification in the study.

In this study, the proposed approach contains CTIC application as a standard procedure for Hyperion image classification. In order to confirm the requirement of CTI correction as a processing step for the classification improvement, the classification is performed using the ordinary MNF transformed data and using the CTI corrected MNF data and the results are evaluated for comparison. Although n-dimensional visualization is a versatile and powerful tool for end-member selection, it is impossible to use n-dimensional visualization tool as a standard operation for both MNF data. This is because, data clouds of both MNFs in n-dimensional data space are different than each other. Shape, size and distribution of the observed clusters in data clouds may not be indicate the same classes for both MNFs. Although defining the cluster boundaries depend on the operator's experience and knowledge, there are so many possibilities to describe same clusters for both MNF data sets. Therefore, it is impractical to use n-dimensional visualization tool for defining the same classes in both data sets.

This part of the study was carried out for Ekecek image data. In order to obtain comparison between the CTI corrections of MNF image and raw (ordinary) MNF image, out of unsupervised classification techniques k-means algorithm with 10 classes was used during the study. Figure 6. 2 shows the unsupervised classification using original MNF bands and CTIC applied MNF bands. As can be seen on the classification results, third order CTIC applied MNF images (Figure 6. 2 (b), (c), and (d)) have no any trend feature discretized as a class, while the result for no CTIC applied data (Figure 6. 2 (a)) has a definite trend features mapped as separate classes. After the first additive CTIC application, the observed strip like classes was narrowed. Furthermore, when the second additive CTIC was applied, the observed

strips located on the East side of the image were narrower than the previous CTIC result. Finally, as the third order additive CTIC was applied to MNF image, the classification result was more satisfactory than the previous classification results (Figure 6. 2) due to absence of trend on the classified data.

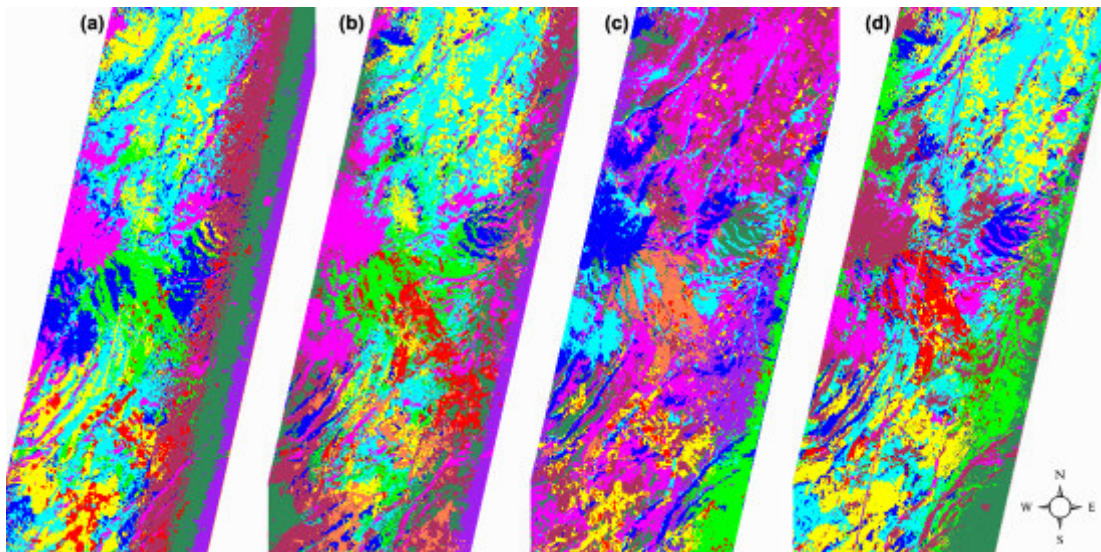


Figure 6. 2. Unsupervised classification results with 10 classes; using first 20 MNF bands (a), using first 20 MNF bands applied first additive CTIC (b), using first 20 MNF bands applied second additive CTIC (c), and using first 20 MNF bands applied third order CTIC.

6. 2. Hyperspectral Classification of Ekecek Image

Ekecek study area covers different outcrops of granites, granodiorities and gabbros. In this case site, lithological discrimination of the major rock units is planned to be performed. Therefore, it is important to find out some key minerals to distinguish lithological units.

6. 3. Spectral Angle Mapper (SAM) Classification of Ekecek Image

In order to classify the Hyperion image of Ekecek area, Spectral Angle Mapper (SAM) classification method is used. Three different sources of spectra are used for SAM classifications. One of them is spectral field measurement of samples; the other one is the United States Geological Survey (USGS) spectral library for minerals; the last one is John Hopkins University (JHU) spectral library for rocks.

Rule images of SAM shows the magnitude of SAM angle of related endmember in radiance and lower pixel values is indicating the likelihood of the endmember in ENVI image processing software (personnel communication of Stefano Gagliano, ITT Visual Information Solutions Italy). The target area of Ekecek test site has mainly covered by gabbro and Ortaköy Granitoid which has granite, granodiorite, granite porphyry etc. (Atabey, (1989) and Kara, (1991) in Figure 6. 3).

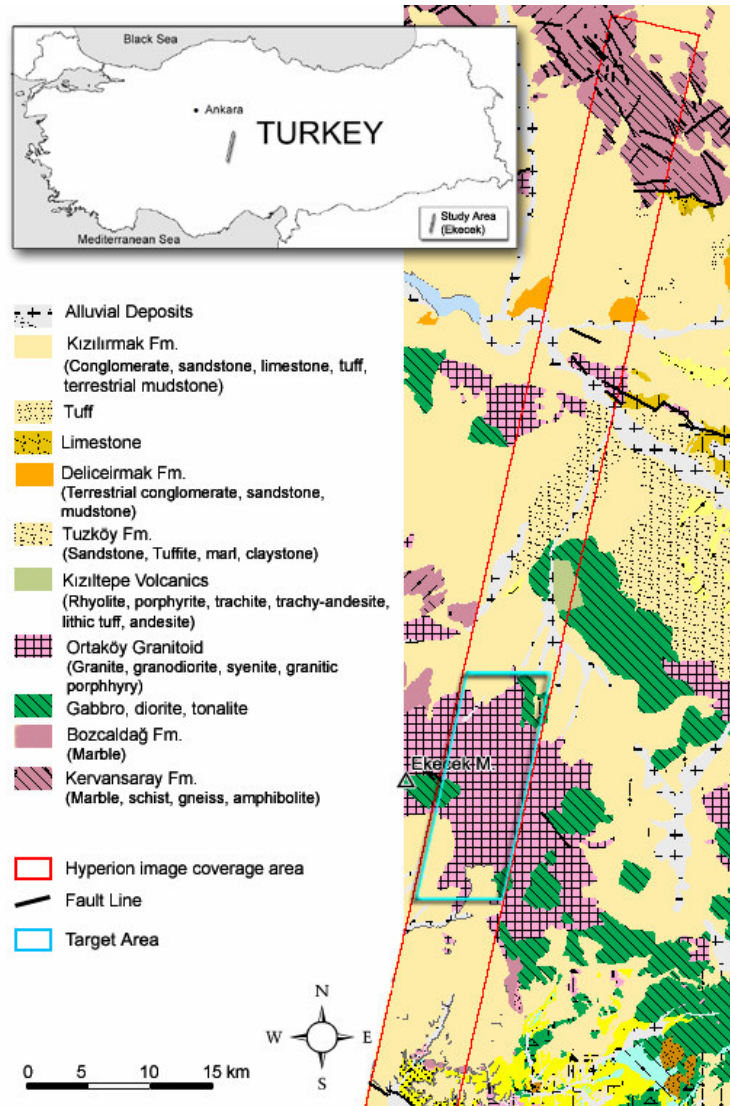


Figure 6. 3. 1: 100 000 scaled simplified Geological map (Atabey, (1989) and Kara, (1991)) and image boundary of Hyperion data.

It is difficult to distinguish different type of granites on the field without any chemical analysis or measurements. The usage of hyperspectral data is helpful for spatial distribution of the different type of granites on the target area. In order to separate these units from each other, JHU spectral library for gabbro, granite, and granitoid is used. Figure 6. 4 shows the RGB color composite representation of the SAM rule images for Gabbro, Granite, and Granodiorite from JHU spectral library endmembers. Reddish color shows

the highest possibility of gabbro which is marked as C on the figure. This location is checked with the field observations and the area marked as C is mainly covered by gabbro units. Granite and granodiorite are assigned to the green and blue channels, respectively. However, location of A and B are not separated clearly using JHU spectral library samples because, chemical composition of the JHU endmembers do not match to field samples.

The second generation of SAM rule images is attempted to separate main mineral groups which form the granites and gabbros are used as endmembers in USGS spectral library. The main distinction between granites and the gabbro is presence of olivine and quartz. Gabbro does not have quartz minerals and granite does not have olivine minerals. (Bell, 1993) Therefore, spectral responses of these two minerals are the key for separation of gabbro and granite. Figure 6. 5 shows the RGB color composite of olivine - kaolinite - orthoclase endmembers from negative rule images. All reddish color illustrates the high possibility of olivine that means gabbro covered area shows as reddish color with the letter of C on the Figure 6. 5. Gabbro which is mainly located on Ekecek Mountain (C) and the distribution of olivine rule image are coincided to each other.

Another important key mineral is kaolinite which is used for discrimination of altered granites and granites. In Figure 6. 5, granite and altered granite separation are noticed as bluish and greenish colors, respectively. The separation of them is clearly observed as a result of the SAM rule image analysis.

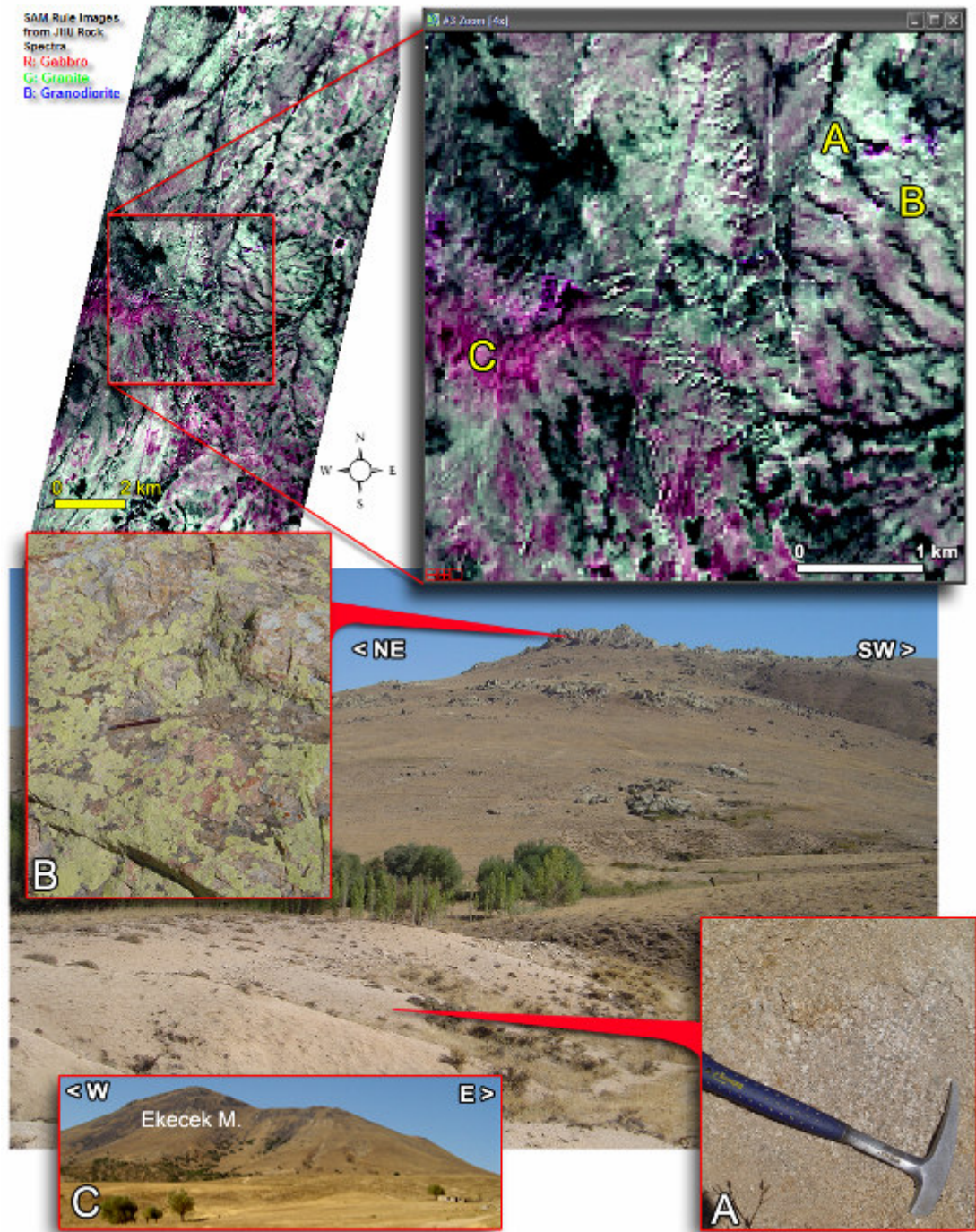


Figure 6. 4. RGB color composite representation of negative SAM rule images for Gabbro, Granite, and Granodiorite from John Hopkins University (JHU) spectral library and photo on the same location from the field study. A and B shows the location and appearance of altered granite and granite, respectively. C is taken from Ekecek Mountain.

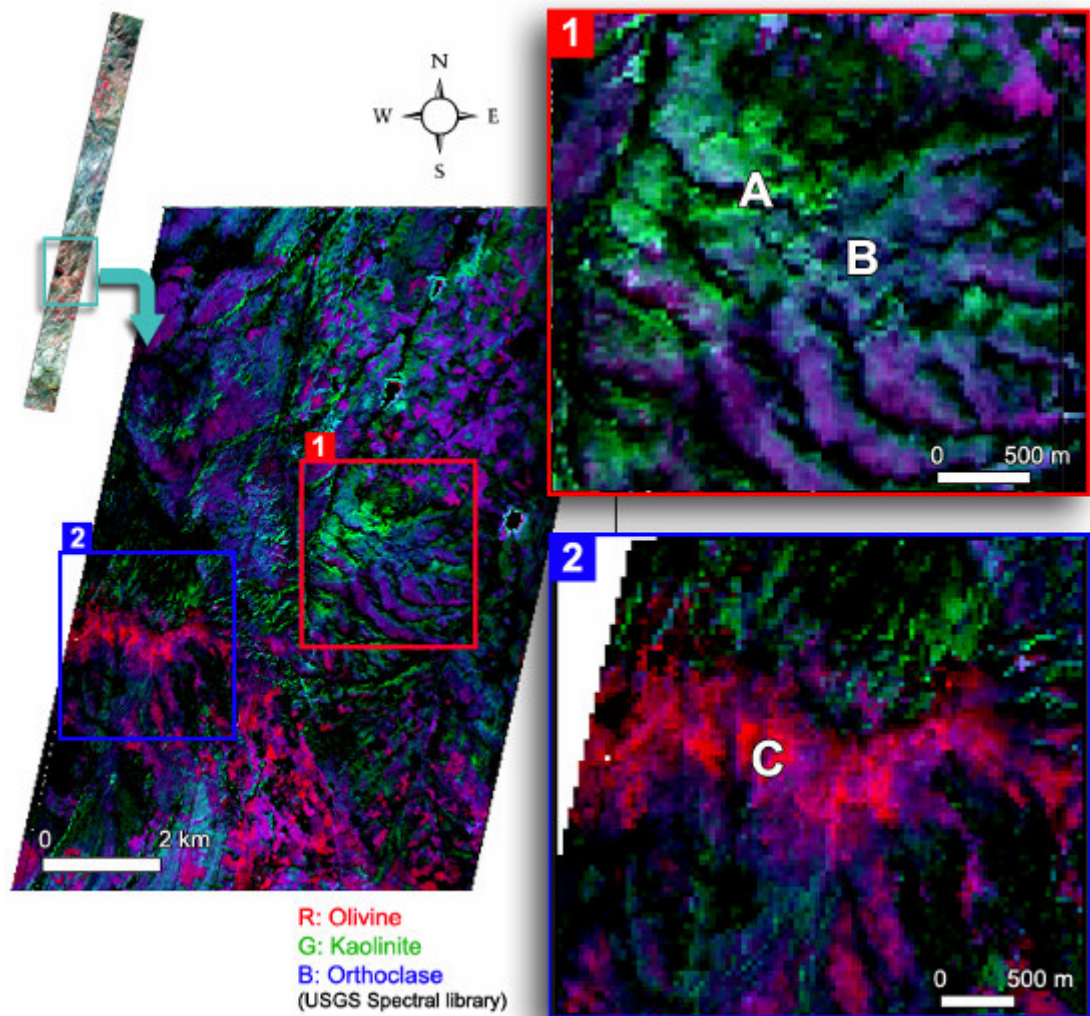


Figure 6. 5. RGB color composite representation of negative SAM rule images for olivine, kaolinite, and orthoclase from USGS spectral library. The rule image of the olivine endmember is assigned to red channel. Kaolinite endmember is directly related with the altered granite (A) and rule images of the sample is assigned to green channel. Orthoclase endmember is also related with the granite body and it is assigned to blue channel.

The previously mentioned two spectral libraries are the part of knowledge driven mineral mapping methods of which, the user should have information about the key minerals and rock units formed by mineral groups. It should

also be noted that these mineral and rock spectral libraries are composed of the measurements of perfect representative samples.

In Ekecek area, the last attempt to find the lithological differences is to use the spectra from collected field samples (Figure 4. 3, 4. 4, and 4. 5). The sampling strategy is based on collection of distinct lithological units. Sample B13 is taken from the gabbro units on Ekecek Mountain to represent the gabbro. Sample A03 and B20 stand for altered granite and granite units, respectively. In Figure 6. 6, RGB color composite of the samples are shown and reddish color shows gabbro units. In addition to that greenish and bluish colors illustrate the distribution of altered granite and granite units. The letter of A, B, and C are the ground control points of altered granite, granite and gabbro units.

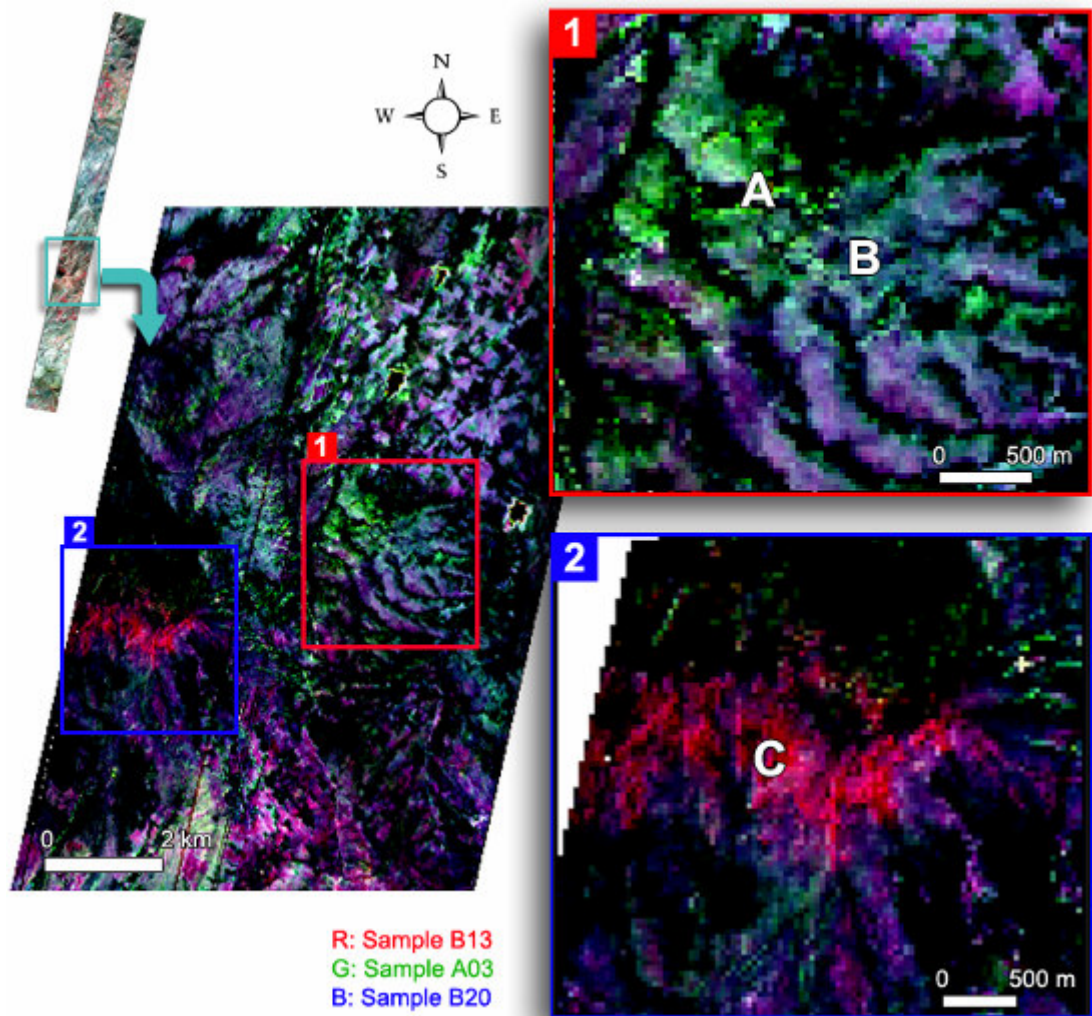


Figure 6. 6. RGB color composite representation of SAM rule images for sample B13, sample A03, and sample B20 from Field Samples Spectra. The rule image of the sample B13 endmember is assigned to red channel. The sample A03 endmember is taken from the altered granite (A) and rule images of the sample is assigned to green channel. sample B20 endmember is also related with the granite body and it is assigned to blue channel.

6. 4. Hyperspectral Classification of Biga Image

Previously, the lithological classification using Hyperion data is carried out on the Central Anatolia (Ekecek). In this section, the mineral mapping and mixture analysis are presented. The target on study area of Biga which is 1.5 km North-West of Çan mainly covers different type of clay minerals especially

kaolinite (Figure 6. 7). Furthermore one large open pit mine operated for coal extraction that neighbors to the largest Kaolinite open pit mine of Turkey is in the spatial subset of the Biga image.

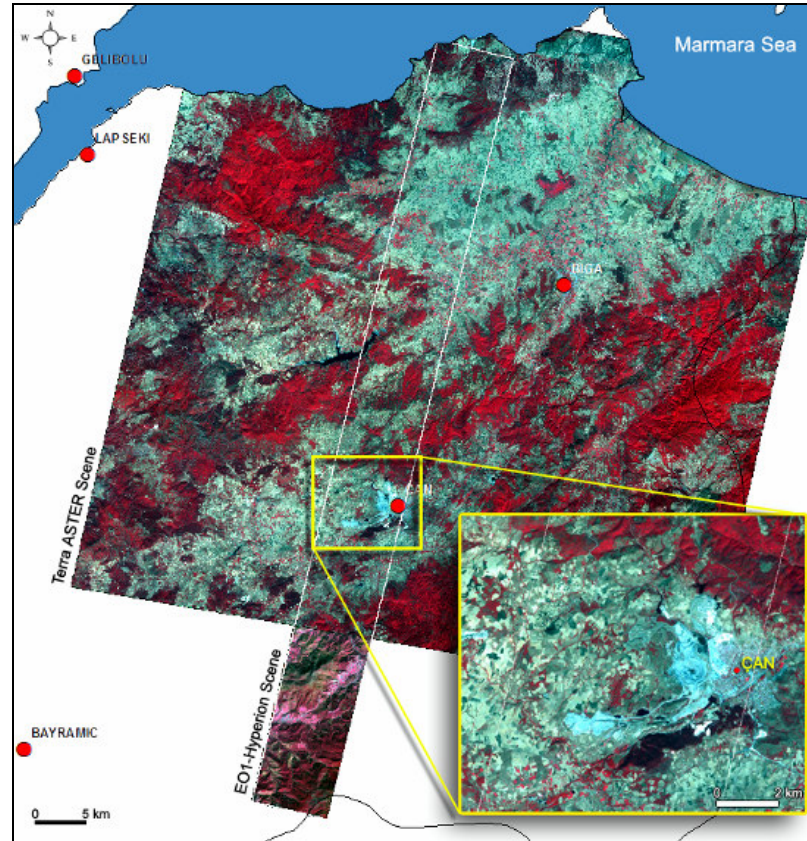


Figure 6. 7. False color representation of ASTER and Hyperion images of Çan area.

Similar preprocessing steps are applied on the Biga image. In this case, ATCOR2 atmospheric correction technique is used as an atmospheric correction. Then, CTIC is applied for removal of smile effect. Finally, SAM classification method is used for mineral mapping on the target area.

6. 5. Spectral Angle Mapper (SAM) Classification of Biga Image

In order to classify the Hyperion data of Biga area, SAM rule images are computed using two different sources which are USGS spectral library for

minerals and spectral measurements from the field samples. The major difference between the previous application and this application is that mixture analysis is performed at the end of the process in this case.

At first, USGS mineral spectral library is used for calculation of SAM rule images. During the SAM analysis, kaolinite, montmorillonite, and hematite minerals are used as endmembers. Then, obtained results are compared with the SAM rule images of field samples which are shown in Figure 6. 8.

Figure 6. 9 illustrates the RGB color composite of rule images derived from USGS spectral library minerals (Hematite, illite, kaolinite, halloysite, and quartz). Hematite rule image is assigned to red channel for all combinations, then hematite rich composition on the images are seen as reddish color in Figure 6. 9 (a), (b), and (c). In Figure 6. 9 (a), Halloysite and Kaolinite rule images are assigned to blue and green channels, respectively. Similarly, kaolinite rule image is assigned to green channel for Figure 6. 9. (b) and (c). In addition, Halloysite and Quartz rule images is allocated to the blue channels for displaying.

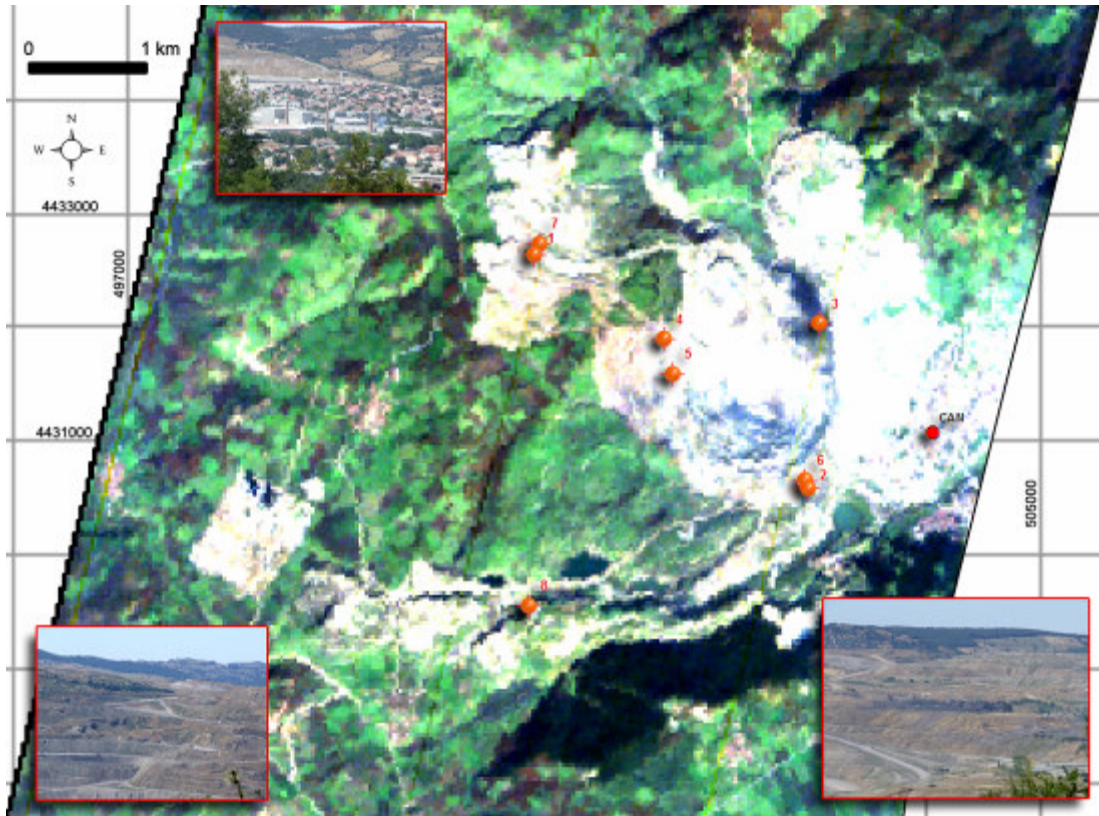


Figure 6. 8. Collected samples on true color representation of Hyperion image.

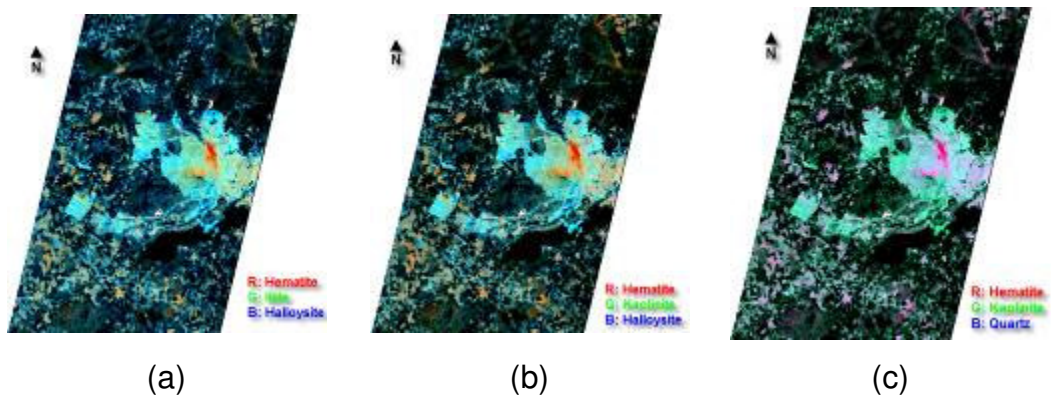


Figure 6. 9. RGB color composite of rule images derived from the USGS spectral library. Three different color composite images are (a) RGB: Hematite-Illite-Halloysite, (b) RGB: Hematite-Kaolinite-Halloysite, and (c) RGB: Hematite-Kaolinite-Quartz.

6. 6. Cross Correlations and Performance Evaluation

Except for the previous tests for accuracy assessment of CTIC application, rule images of each endmembers are inspected separately for checking the effects of CTIC on each endmembers of USGS. In this part of the study, endmembers are chosen from USGS spectral library according to field samples which are analyzed at MTA (Mineral Research and Exploration General Directorate) Mineralogical Analyses Laboratories. According to the analysis results, collected samples have mainly composed of halloysite, illite, smectite, kaolinite, opal, quartz, and hematite with varying amounts. In order to carry out this evaluation, cross correlations are performed between before and after the CTIC for each endmember rule images. The main logic of the correlation is whether the CTIC affects the rule images of corresponding endmembers or not. If the correlation of the rule images is high, then it would be concluded as the CTIC does not affect the corresponding endmember (Appendix E).

When the correlation coefficient (r) approaches to 1, and the slope of the correlation is equal to 1, then it means that two variables are highly correlated to each other. According to the correlation coefficients of endmembers' rule image, the highest correlation coefficient ($r= 0.9964$) and the slope value ($a= 0.98$) are observed on quartz endmember. On the contrary, the lowest correlation coefficient is obtained as 0.9883 for opal endmember and the lowest slope values is calculated as 0.6 for halloysite endmember. The correlation coefficients from the lowest to highest value are ordered as the endmembers of opal, halloysite, kaolinite, illite, hematite, halloysite+Smectite and quartz (Figure 6. 10). According to the slope values from the lowest to the highest, endmembers are ordered as follows: halloysite, kaolinite, illite, hematite, kaolinite+smectite, opal and quartz (Figure 6. 11).

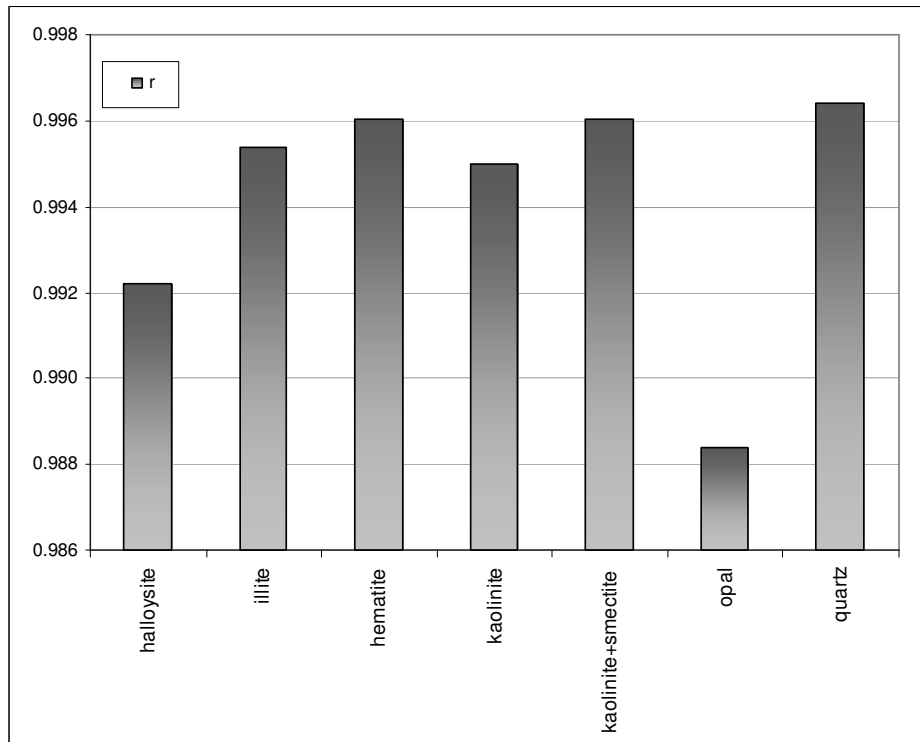


Figure 4. 10. Cross correlation coefficients (r) between before CTIC and after CTIC for different rule images of endmembers.

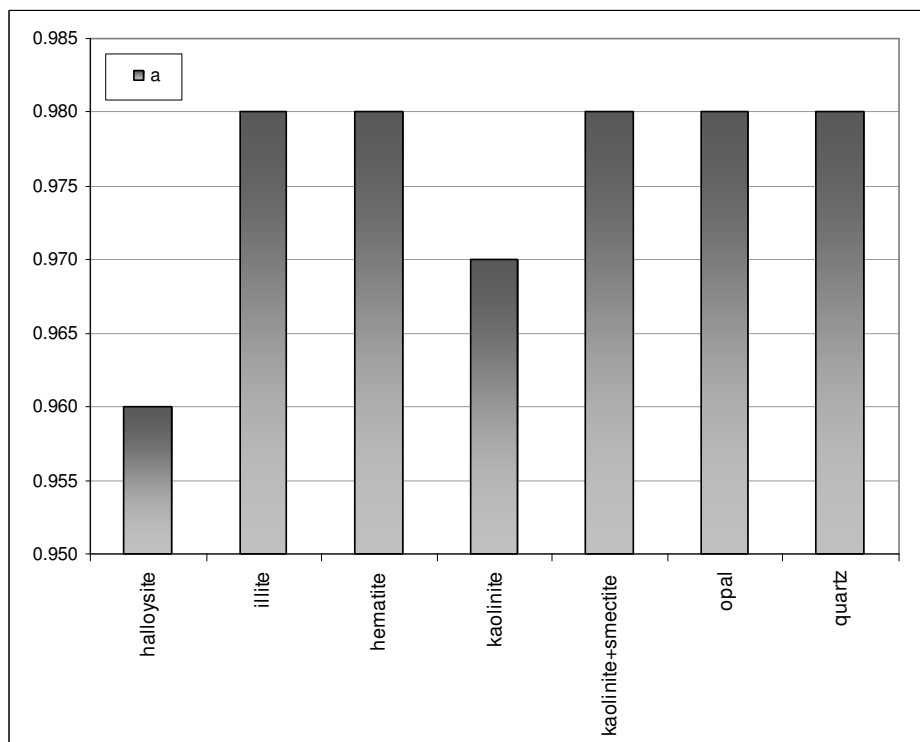


Figure 4. 11. Slope values (a) between before CTIC and after CTIC for different rule images of endmembers.

The other performance evaluation technique is Variance Account For (VAF) which is given as below (Grima, (2000) and Tutmez et. al., (2006));

$$VAF = \left(1 - \frac{\text{var}(y - y')}{\text{var}(y)} \right) * 100 \quad (6.1)$$

where, var stands for variance. y and y' are the no CTIC corrected and second order CTIC corrected rule images, respectively. At the end of this computation, performances of each endmembers are obtained in percentages. Figure 6. 12 shows the VAF values of the endmembers.

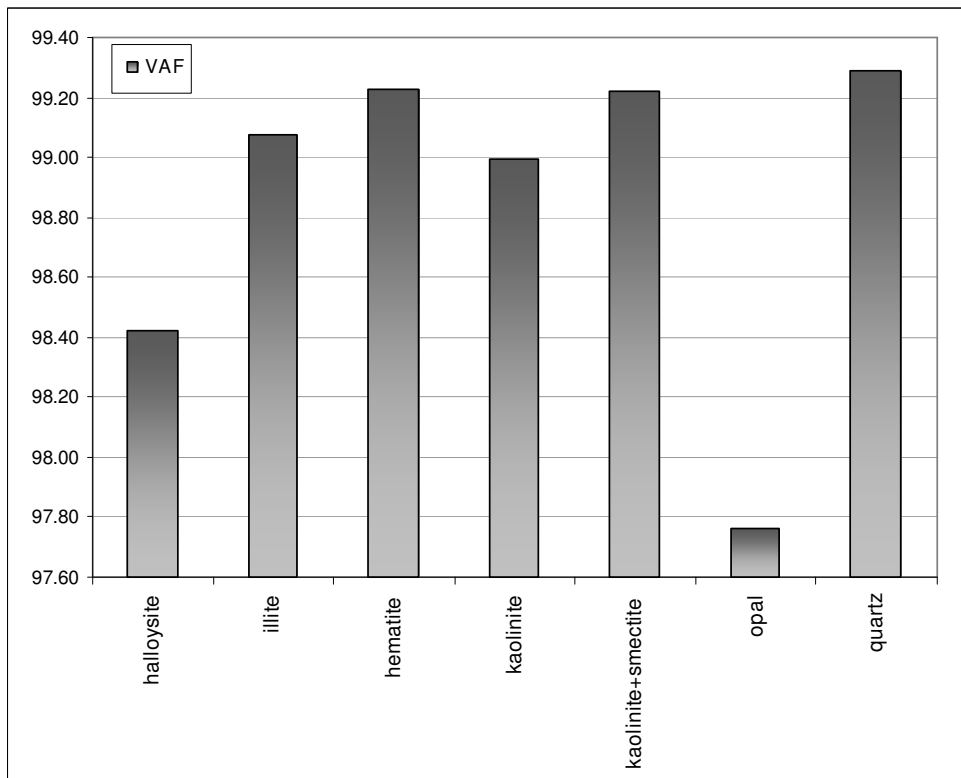


Figure 6. 12. VAF values of endmembers between before CTIC and after CTIC for different rule images of endmembers

According to the cross correlation analysis on the Biga image, CTIC mainly affects the opal, halloysite, kaolinite, and illite endmembers. Quartz is the

lowest effected endmember on this area. As a result of the cross correlation analysis, the application of CTIC must be performed as a standard procedure for hyperspectral image classification scheme.

6. 7. Spectral Mixture Analysis (SMA)

The minerals in natural environment are formed as mixture. On the contrary, the minerals in spectral library are composed of the pure minerals. Even one of the largest kaolinite open pit mine of Turkey exists in the study area of Biga, presence of mixtures are still expected. Likewise the measured spectrum within the instantaneous field of view of the sensors of Hyperion (900 m²) happens to be the combination of the spectra of various minerals (Dennison and Roberts, 2003). Therefore, it is necessary to create spectral mixture analysis (SMA).

SMA is the technique based on linear combination of endmembers with the fractional involvement (Dennison and Roberts, (2003), Kameyama et. al., (2001), Haboudane et. al., (2002)). SMA can be denoted as the following formula (6.2) by De Jong, and Van Der Meer, (2004);

$$A_i = \sum_{j=1}^N F_j B_{ij} + \epsilon_i \quad (6.2).$$

where, A_i is a mixture spectrum for a pixel in band i , F_j is j^{th} endmembers in the pixel, B_{ij} is the fraction of j^{th} endmember in the i^{th} band, N is the number of endmembers in the scene, and ϵ represent the residual errors.

In linear mixtures, sum of all the endmember fractions are commonly constrained to 1;

$$\sum_{j=1}^N F_j = 1 \quad (6.3)$$

Spectral mixture analysis (SMA) is performed on Biga test site. In this part of the study, spectral measurements from the field constitute the reference spectra. There are 8 samples collected from the field and measured with the ASD field spectrometer within the wavelength range of 400 nm to 2500 nm. Then, all spectra are analyzed using SpecMin Pro software. Figure 6. 13 shows the spectra of field sample 1 and corresponding USGS spectral library minerals for mixture. In this analysis, spectra of USGS spectral library minerals are checked for consistency with the sample spectra in different wavelength regions. If a match exists, then the matched spectra are attached to a matched minerals pool. After selecting minerals, un-mixing is performed.

Spectral un-mixing is carried out for all the field samples collected from the Biga test site. The un-mixing results are summarized in Table 6. 1. Even though the USGS spectral library has pure minerals, there are some different contents of them such as different types of halloysite minerals. Halloysite 5 stands for the mixture of halloysite and kaolinite minerals (Appendix F).

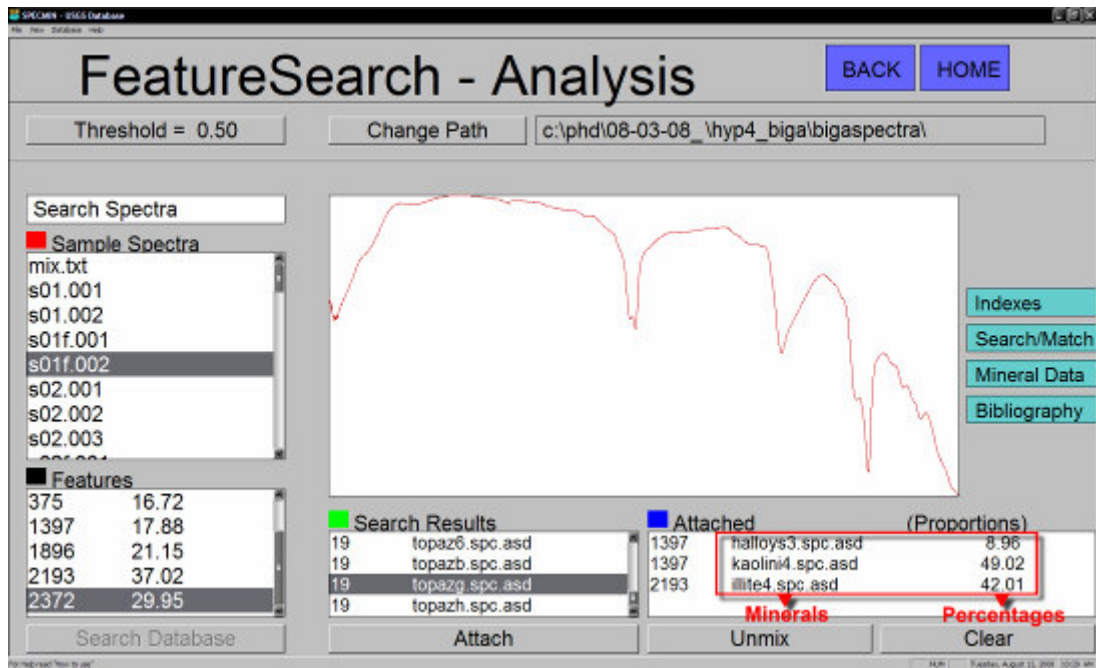


Figure 6. 13. Spectral Mixture Analysis for sample 1 from Biga test site.

Table 6. 1. Spectral un-mixing results showing the mineral ratios of the corresponding samples

Minerals from USGS Spectra	Sample 1	Sample 2	Sample 3	Sample 4	Sample 5	Sample 6	Sample 7	Sample 8
Albite 2								24.22
Halloysite 1					65.86			
Halloysite 3	8.96	32.15		52.93		14.09		
Halloysite 4					34.14			
Halloysite + Kaolinite 5			22.64	44.57				
Hematite 1								19.13
Illite 4	42.01	6.89		2.50		1.72	61.62	
Illite 5								10.05
Kaolinite 4	49.02	32.40						10.76
Kaolinite 6		20.45						
Montmorillonite 2							38.38	
Muscovite 4		8.12						
Oligoclase 2			77.36					
Kaolinite + Smect 5								34.70
Opal 2						48.71		
Quartz 2						35.47		1.14

After obtaining mixture proportions, linear mixture of each sample is generated as seen on Figure 6. 14. As can be seen on the figure, spectra of mixtures and field samples are almost similar to each other. The correlation coefficients of the samples 1 to 8 are computed as 0.92, 0.94, 0.73, 0.69, 0.93, 0.97, 0.84, and 0.97, respectively. The lowest correlation, 0.69, is

observed between the mixture 4 and sample 4. This is because, correlation analysis is applied in whole spectrum range, however, there are no any consistencies of the wavelength on visible region. The second lowest correlation, 0.73, is reported between mixture 3 and sample 3. Although the correlation of them is low, spectral response curves of them are similar to each other. Main difference appears on the absorbance strength. Field sample 3 has water absorbance on 1412 nm and 1925 nm wavelengths. On wavelength of 1413 nm, absorbance depth of sample 3 and mixture 3 are 1 and 5 percents, respectively (Figure 6. 14 (c)). Other mixtures and the samples are successfully matched to each other having correlations higher than 0.80.

Similarly, the logic of same SMA is applied with different mineral contents. In this case, SMA is performed using the minerals from XRD analysis results. Therefore, irrelevant mineral or mineral groups directly eliminated at the beginning of the mixture analysis. In this part of the study, 10 minerals which are Albite, Anorthite, Halloysite, Hematite, Illite, Kaolinite, Kaolinite + Smectite, Opal, Orthoclase, and Quartz are forced to used for spectral mixture of field samples. These mineral groups are chosen from USGS spectral library. Table 6. 2 shows the proportion of minerals for each samples. For example, sample 6 is composed of 8.15 % of albite, 47.92 % of kaolinite + smectite, and 31.08 % opal minerals.

Table 6. 2. Spectral un-mixing results show the mineral ratios of the corresponding samples using minerals from XRD results.

Minerals from XRD results using USGS Spectra	Sample 1	Sample 2	Sample 3	Sample 4	Sample 5	Sample 6	Sample 7	Sample 8
Albite						8.15	28.32	
Anorthite	17.13	34.98		68.46	55.77			
Halloysite	0.41			23.05	24.89		3.01	
Hematite			5.45					5.43
Illite	2.62		18.16		10.00			
Kaolinite	36.79	47.62					12.85	9.87
Kaolinite + Smectite	5.27	16.48		1.94	2.59	47.92	44.16	35.43
Opal	0.03		14.52	6.55	6.75	31.08	9.82	11.09
Orthoclase		0.92	61.87				14.69	25.71
Quartz	37.75							12.47

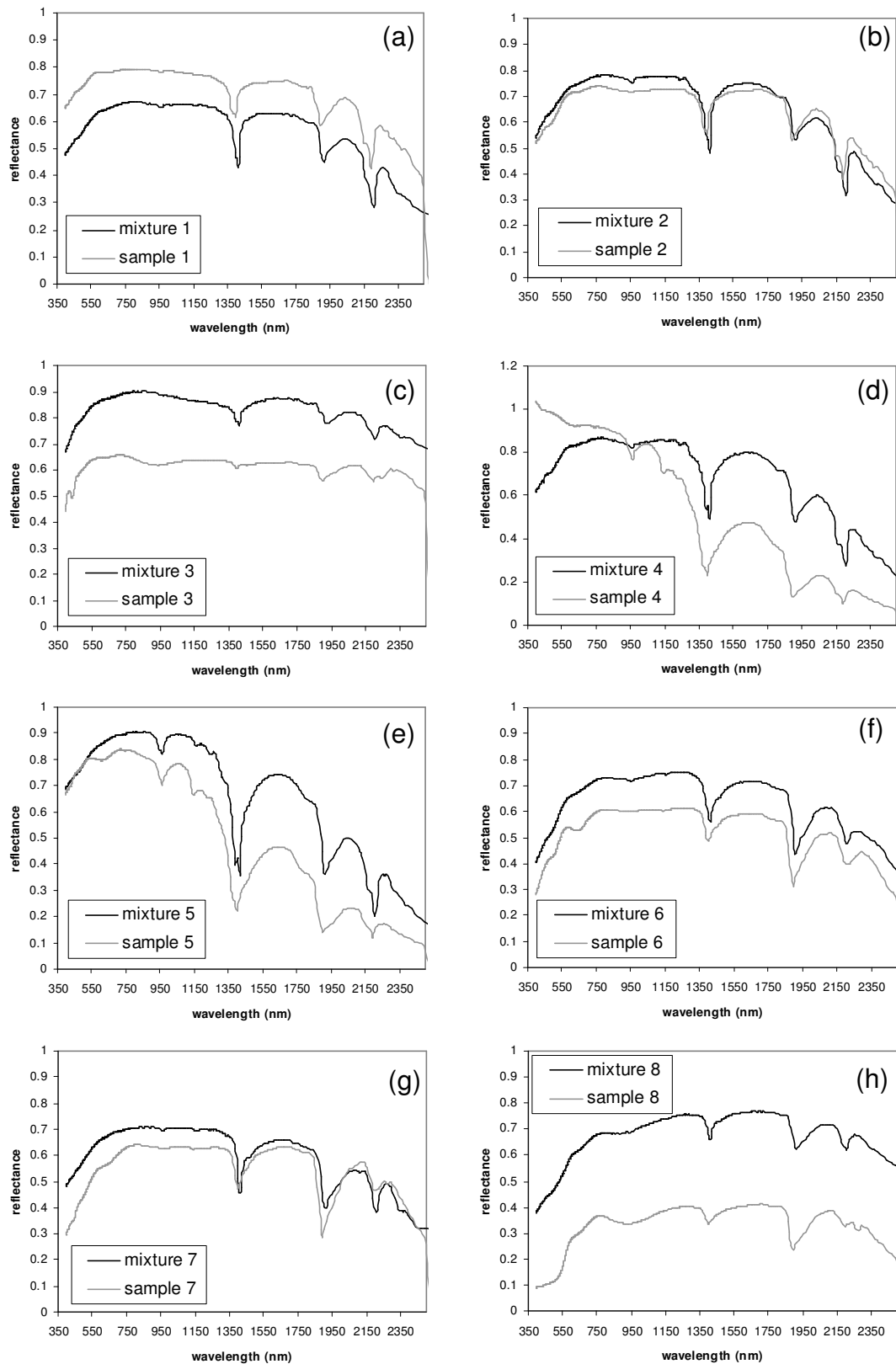


Figure 6. 14. Field sample spectra and their matched corresponding mixtures. Sample 1 and mixture 1 to sample 8 and mixture 8 are shown from (a) to (h).

Figure 6. 15 illustrates the spectra of field samples and corresponding mixtures using USGS minerals from XRD results. According to the spectral curves, mixture 4 and 5 (Figure 6. 15. (d) and (e)) are not correctly matched to their corresponding samples. As the correlations between the samples and complementary mixtures are investigated, the highest correlations are observed on sample 8 and sample 6 with the value of 0.97 and 0.96, respectively. The other correlation values are listed as follows: 0.46 for mixture 1, 0.90 for mixture 2, 0.53 for mixture 3, 0.38 for mixture 4, 0.65 for mixture 5, 0.96 for mixture 6, 0.93 for mixture 7, and 0.97 for sample 8. When comparing these correlation values with the previously obtained correlation of SMAs, mixture 2, 6 and 8 are almost the same values even though the mixture constituents are not exactly the same. Correlation value of mixture 1, 4, and 5 are changed more than half a percent.

The differences occur between the correlation values of previously applied SMA and this SMA due to the application techniques. The former technique uses whole spectral library minerals and there is no any restriction to select minerals for mixture. However, the later one is used only limited number of minerals for SMA. The match algorithms of both techniques are the same but the input mineral groups are different.

Finally, spectra of mixtures obtained from USGS spectral library and field samples spectra are compared by using them as input spectra for SAM classification. The resultant rule images for both SAM classifications are employed for cross correlations. Figure 6. 16 summarizes the correlations between field samples spectra as x-axis and mixtures spectra as y-axis. According to the correlation results given in the Figure 6. 16, mixtures 1, 2, 3, 6, 7, and 8 have high correlation coefficients having the value of 0.99. On the other hand the mixtures 4 and 5 have the correlation coefficients of 0.5928 and 0.7886, respectively.

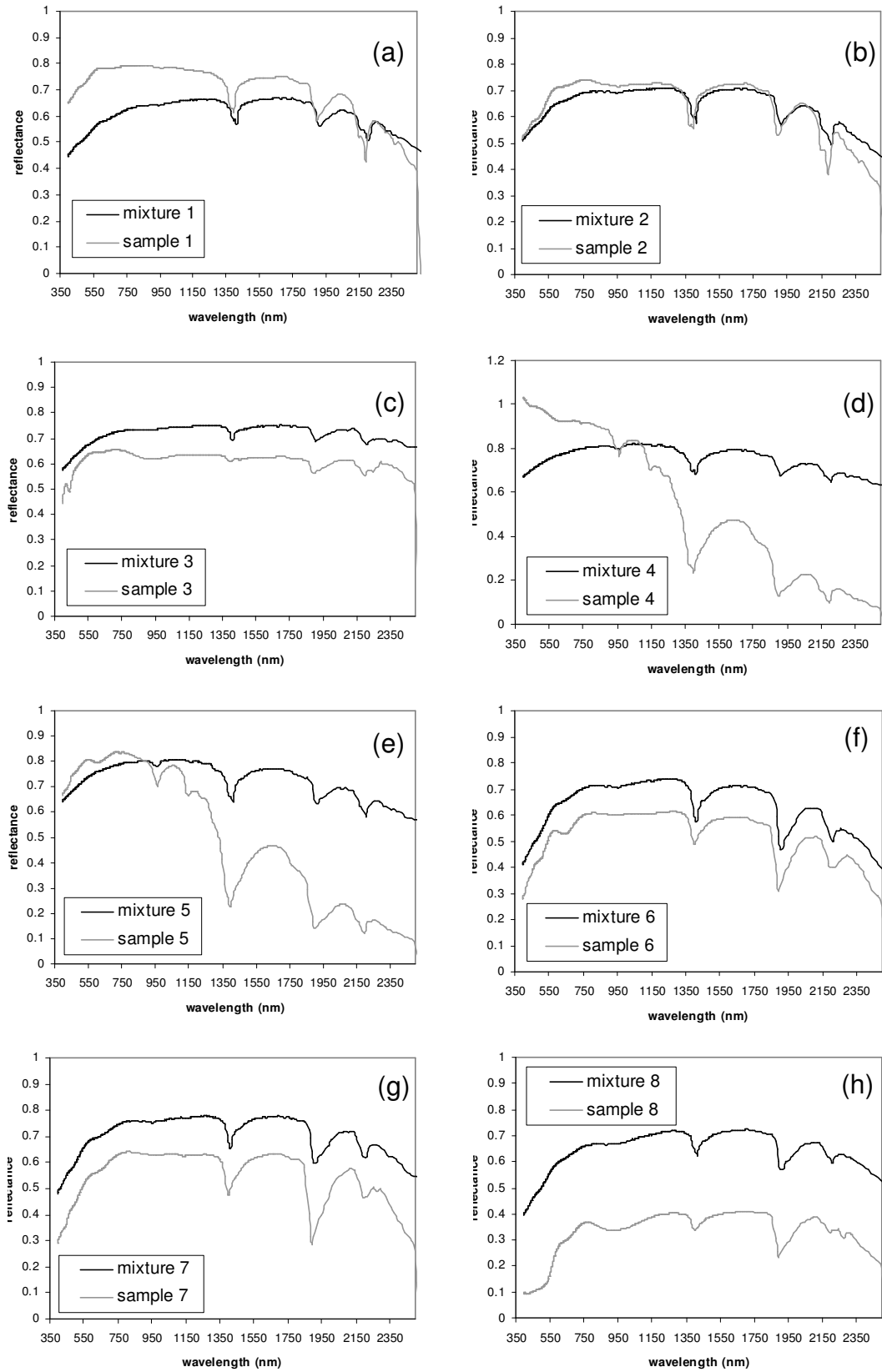


Figure 6. 15. Field sample spectra and their corresponding mixtures using minerals from XRD result. Sample 1 and mixture 1 to sample 8 and mixture 8 are shown from (a) to (h).

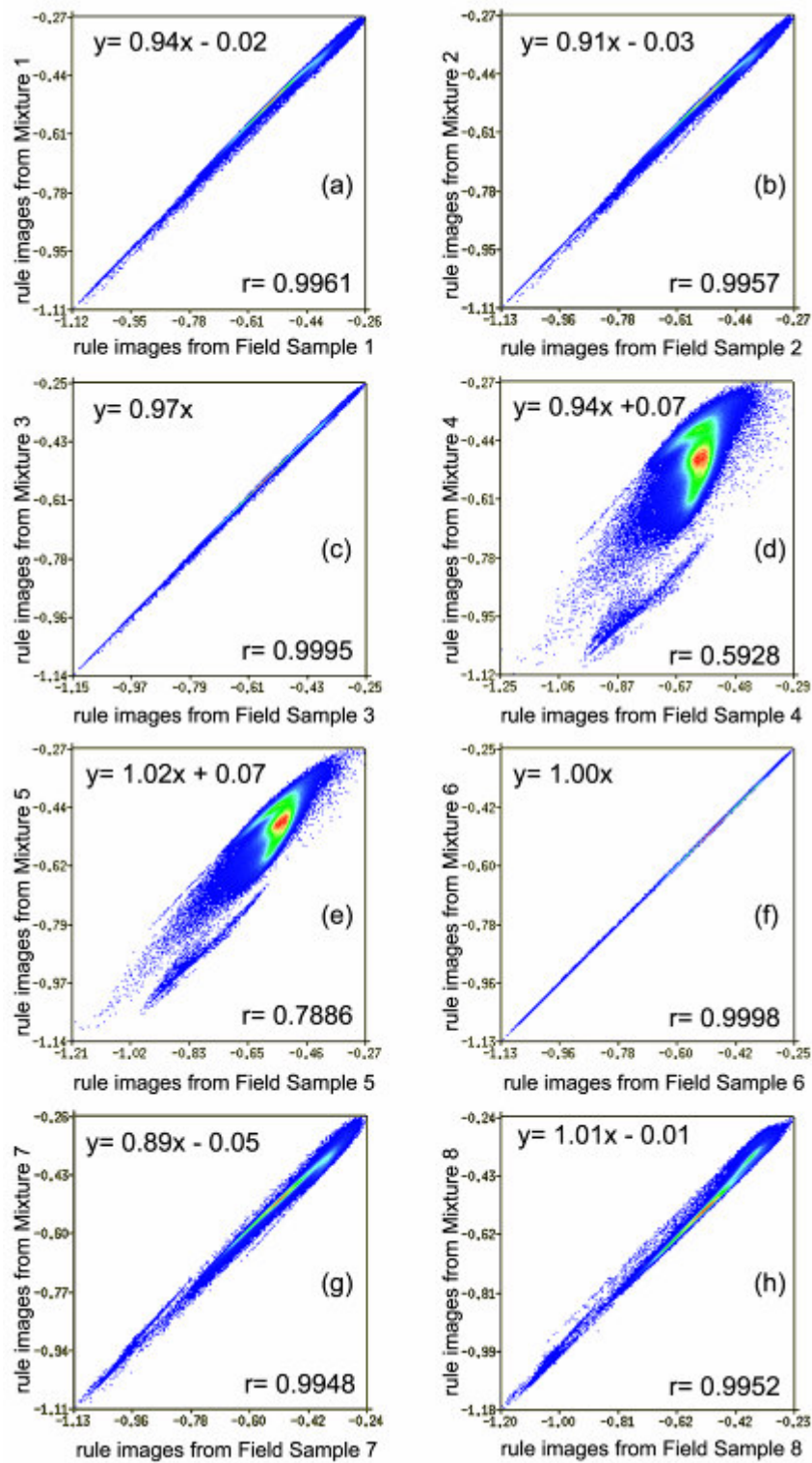


Figure 6. 16. Correlations between SAM rule images of Field Spectra (x axis) and SAM rule images of corresponding mixture spectra (y axis). Figure (a) to (h) stands for mixture 1 to 8. (r stands for the correlation coefficient).

In addition to the correlation between rule image of mixtures and that of samples, the correlation between the mixtures using minerals from XRD results and the samples is also generated. In this case, except for the mixtures 4 and 5, high correlations are obtained as 0.99 between the samples and corresponding mixtures (Figure 6. 17). The correlation coefficients of mixture 4 and 5 are 0.4122 and 0.4745, respectively.

When comparing two different mixture techniques and the rule image correlations of them, mixtures constructed using USGS spectral library are more similar to the samples collected from the field.

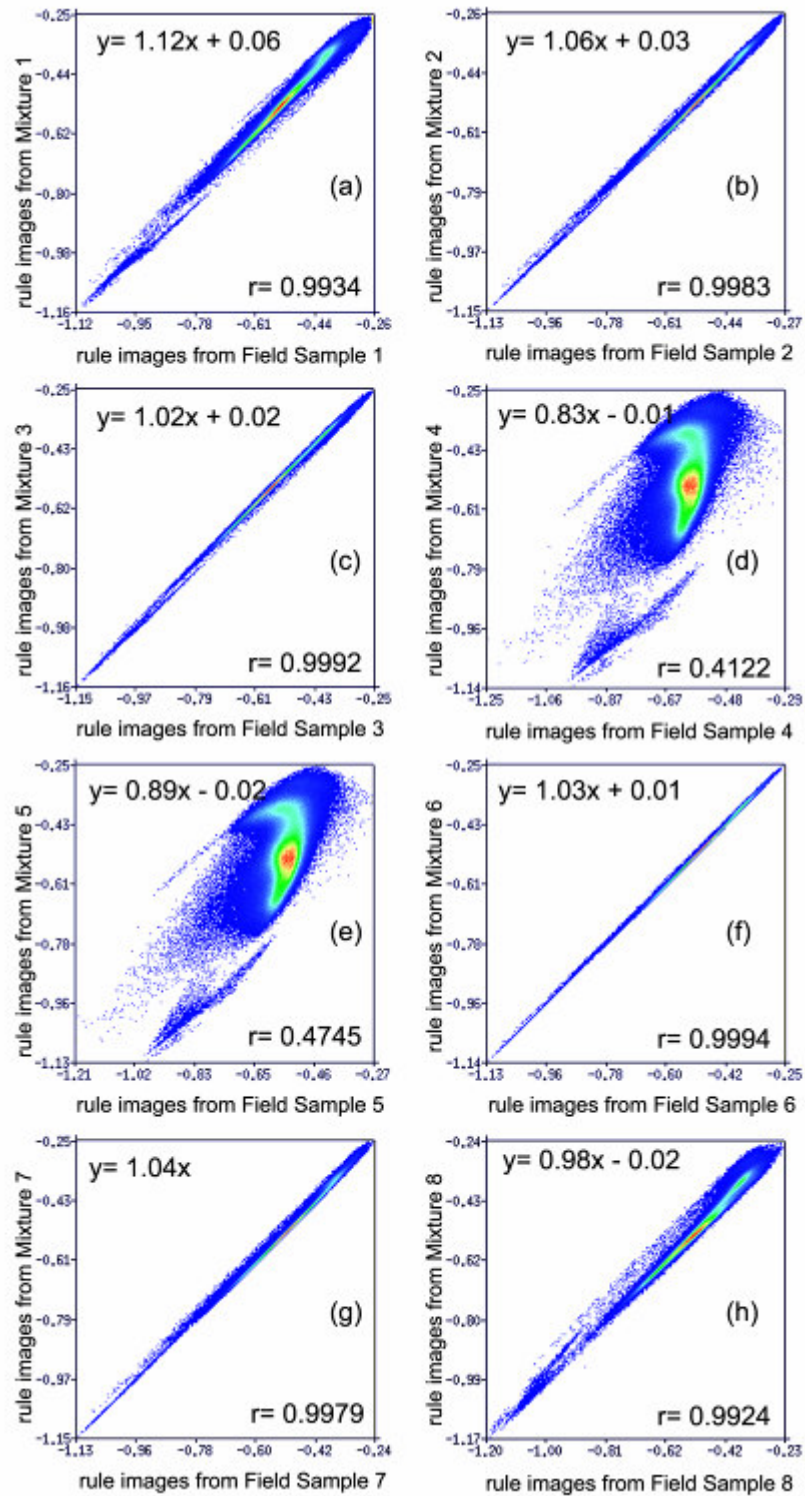


Figure 6. 17. Correlations between SAM rule images of Field Spectra (x axis) and SAM rule images of corresponding mixture spectra (y axis) from XRD analysis results. Figure (a) to (h) stands for mixture 1 to 8. (r stands for the correlation coefficient).

6. 8. Discussion

In this study, lithological and mineralogical discrimination using Hyperion data are evaluated in two different test sites with the measurement of spectral samples. The study shows that hyperspectral image processing is not an automatic process as it seems and presented in theory. Each processing step has some problems due to atmospheric effect, cross track illumination of data, physical and environmental restrictions of the mass amount of image channels, characteristics of target area, vegetation cover, and user experience and etc.

Even though, atmosphere is the main source of noise in hyperspectral imaging, there is no any perfect model or solution to remove this effect. In the first stage of the study, different atmospheric correction techniques are compared in detail to obtain the proper one. If more than one atmospheric correction modules are available, then it is better to compare them before starting to use in the analysis, as atmospheric correction is highly case and location dependent. Although, basically most of the atmospheric correction techniques are derived from MODTRAN radiative transfer code, obtained results of them are not same. In order to decide appropriate atmospheric correction technique, comparison of the corrected image spectra with the corresponding field samples should be carried out. In addition to spectral correlation of the atmospheric correction results, specific absorption wavelengths are compared with the reference spectra from field samples.

Although ACORN atmospheric correction modules has no capability of displaying image data, the cross correlation results and comparison of specific wavelength absorption features between reference spectra and atmospherically corrected data reveal that ACORN is more successful correction technique than the other correction techniques applied on Ekecek test site.

Except for the atmospheric effect, topographical variation is another environmental factor which affects the hyperspectral image processing. This variation changes the real reflection values of the rock or mineralogical units. ATCOR3 is the only one atmospheric correction algorithm considering the topographical changes.. Nevertheless, DEM and hyperspectral image data should be geometrically corrected to each other with the nearest neighbor resampling method for keeping the original reflectance value to use ATCOR3 before starting to processing stage. Even if one pixel geometric shift exists between the image and DEM data, the resultant image is affected. Therefore, if DEM data is not available on the study area, then other atmospheric correction technique should be selected for correction.

Nonetheless, atmospheric correction of Hyperion data is not enough to use for image processing. Before starting to process, un-calibrated channels should be eliminated. In addition, water vapor absorption bands should be eliminated to remove the un-corrected and/or unpredicted noise. And also there exists cross track illumination (smile) effect on Hyperion data which is caused by change of dispersion angle. Smile effect can be recognized by using MNF transformation of whole image data. This is another parameter to be removed or minimized to obtain successful results. In two test sites, images with and without removal of smile effect are compared. These comparisons are performed for both the lithological and mineralogical discriminations. The results show that Hyperion data has a definite smile effect and before starting any image processing it should be removed to acquire better results. However, the degree of the smile effect is varying from image to image. Therefore, the degree of smile effect should be investigated, stated, and removed in the preprocessing stage of Hyperion image processing. According to the study, smile effect is mainly observed on VNIR image bands. If the user does not have any chance to minimize or remove this effect, then only SWIR channels can be used for the further analyses.

Finally, some spectral mixture analyses are introduced in the Biga test site to extract some mineral assemblages. Collected field spectra and corresponding mixtures created using SMA were compared. SMAs were completed with the two different mineral groups and these results were also compared with the reference data. This analysis illustrates the possibilities of mixture generation. As a result of performed two different SMAs, in order to generate a mixture, better way is to select minerals from spectral library with the related absorbance channels. The proportions of minerals can be produced using SMA or vice versa. However, SMA is a broad concept in imaging spectroscopy. In this study, only aerial mixture model are investigated and the mixtures are generated linearly. In nature, especially in lithological discriminations, mixture is based on intimate. However, in practice it is difficult to model for intimate mixtures.

For lithological mapping, it is important to find key mineral(s) which is directly related about the priory knowledge of the geology / lithology about the investigated site in processing of Hyperion data. Similarly, which type of minerals exists or occur in the same unit should be known for successful SMA. Intense knowledge of lithology about the units on the investigated site is required for detail applications of hyperspectral imaging.

CHAPTER 7

CONCLUSIONS AND RECOMMENDATIONS

In this chapter, the conclusions that were reached during this research and the success of proposed approach are presented. Then, the recommendations concerning further studies are given.

In hyperspectral image processing, there are no unique routine techniques for lithological and mineralogical discriminations. During this research, an approach is developed and proposed for geological remote sensing using Hyperion image data. This algorithm is mainly based on evaluation of pre-processing and evaluation of Hyperion data. According to the proposed approach, Hyperion data is atmospherically corrected using proper correction method which can be determined with the comparison between the available correction algorithm and the reference data.

During the study, the proposed approach is applied and tested at two unique condition study sites. In first site, Ekecek test site, the algorithm is used for lithological discrimination with ACORN atmospheric correction with minimal vegetation cover. On the other hand, the second site, Biga test site, is mainly employed for mineral discrimination and spectral mixture analysis with ATCOR2 atmospheric correction technique with severe vegetation cover.

This study demonstrates a proposed procedure to be followed for lithological and mineralogical mapping using Hyperion image data. Throughout this research CTIC is recommended as a standard process for Hyperion image processing. According to the obtained results for CTIC applied data, third order and second order CTIC is utilized for correction of Ekecek and Biga test sites, respectively. It is concluded that CTIC should be applied before geometric correction and after atmospheric correction stages.

After the whole processes of Ekecek image, granites and gabbro were successfully differentiated from each other. In addition to that some granite types which have different mineral assemblages (like altered granites) are successfully identified. In the Biga test site, kaolinite minerals were effectively determined from the other mineral assemblages. In addition to this, spectral mixture analysis was carried out to estimate detailed mineralogical content.

For recommendations, not only the hyperspectral data is full of errors but field and hand spectrometers do also have significant errors hence they have to be calibrated rigorously. On the other hand the CTIC could only be applied on raw image data, which creates numerous back and forth analysis as some atmospheric correction techniques require coordinates. In further studies, it should be expected that any kind of automatic image artifact finding and removal algorithms would make a great leap in preprocessing of geological hyperspectral remote sensing.

REFERENCES

Abrams, J. M., (1983), Remote Sensing for Porphyry Copper Deposits in Southern Arizona. *Economic Geology*, 78, pp. 591-604.

ACORN 5.0 Tutorial, (2004), ImSpec LLC.

Atabey, E., 1989, 1:100 000 ölçekli Açın-sama Nitelikli Türkiye Jeoloji Haritaları Serisi, Aksaray – H 18 Paftası, Maden Tetkik ve Arama Genel Müdürlüğü, Jeoloji Etütleri Dairesi, Ankara.

Beck, R., (2003), EO-1 User Guide, Version 2. 3., 74 p., University of Cincinnati.

Benediktsson, J.A., Sveinsson, R., Kolbeinn A., (1995), Classification and Feature Extraction of AVIRIS Data, *IEEE Transactions on Geoscience and Remote Sensing*, 33 (5), 1194 – 1205.

Bell, F.G., (1993), *Engineering Geology*, Blackwell Scientific Publications, Oxford, 359 pp.

Boardman, J. W., Kruse, F. A., and Green, R. O., (1995), Mapping Target Signatures via Partial Unmixing of AVIRIS Data: in Summaries, Fifth JPL Airborne Earth Science Workshop, JPL Publication 95-1, v. 1, 23-26.

Borengasser, M, Hungate, W., and Watkins, R, (2008), Hyperspectral Remote Sensing: Principles and Applications, Taylor and Francis Series in Remote Sensing Applications, 6000 Broken Sound Parkway, NW, Suite 300, 119p.

Cetin, H. and Levandowski, D.W., (1991), Interactive classification and mapping of multi-dimensional remotely sensed data using ndimensional probability density function (nPDF), Photogrammetric Engineering and Remote Sensing, 57, 1579 –1587.

Cetin, H., Warner, T.A. and Levandowski, D.W., (1993), Data classification, visualization, and enhancement using n-dimensional probability density functions (nPDF): AVIRIS, TIMS, TM, and Geophysical Applications, Photogrammetric Engineering and Remote Sensing, 59, 1755–1764.

Chang, C., (1999), Interference and Noise-Adjusted Principle Components Analysis, IEEE Transactions on Geoscience and Remote Sensing, 37 (5), 2387 – 2396.

Chang, C., (2003), hyperspectral Imaging: Techniques for Spectral Detection and Classification, Kluwer Academic / Plenum Publishers, 370p.

Chang, C., (2006), A Fast Iterative Algorithm for Implementation of Pixel Purity Index, IEEE Geoscience and remote sensing Letters, 3(1), 63 – 67.

Chen, J. and Wang, R., (2007), A Pairwise Decision Tree Framework for Hyperspectral Classification, *International Journal of Remote Sensing*, 28(12), 2821 – 2830.

Clark, R. N, (1999), Spectroscopy of Rock and Minerals, and Principles of Spectroscopy (chapter 1), *Remote Sensing for Earth Sciences: Manual of Remote Sensing*, 3.ed., Vol. 3, edited by Andrew N. Rencz, 251 – 306.

Clark, R. N., and Swayze, G. A., (1995), Automated Spectral Analysis: Mapping Minerals, Amorphous materials, Environmental Materials, Vegetation, Water, Ice and Snow, and Other Materials: USGS Tricorder Algorithm (abstract), *Lunar and Planetary Science XXVI*, 255 – 256.

Crosta, A. P., and Moore, J. M., (1986), Enhancement of Landsat Thematic Mapper Imagery for Residual Soil Mapping in SW Minas Gerais State Brazil: A Prospecting Case History in Greenstone Belt Terrain, *Proceedings of the 9th Thematic Conference on Remote Sensing for Exploration Geology*, Calgary, 1173 – 1187.

Cudahy, T. J., Rodger, A. P., Barry, P. S. , Mason, P., Quigley, M., Folkman, M., and Pearlman, J., (2002), Assessment of the stability of the Hyperion SWIR module for hyperspectral mineral mapping using multi-date images from Mount Fitton, Australia, *IEEE*, 3504 – 3506.

Datt, B., McVicar, T. R., Van Niel, T. G., Jupp, D. L. B., and Pearlmann, J. S., (2003), Processing EO-1 Hyperion Hyperspectral Data to Support the Application of Agricultural Indexes, *IEEE Transactions on Geoscience and Remote Sensing*, 41 (6), 1246 – 1259.

De Jong, S. M., and Van Der Meer, F., (2004), Remote Sensing Image Analysis: Including the Spatial Domain, Kluwer Academic Publishers, 359p.

Deering D. W., Rouse, J. W., Haas, R. H., and Schell, J. A., (1975), Measuring Forage Production of Grazing Using from Landsat MSS Data, Proceedings, Tenth International Symposium on Remote Sensing of Environment, Ann Arbor: ERIM, 2: 1169 – 1178.

Dennison, P. E., and Robersts, D. A., (2003), Endmember Selection for Multiple Endmember Spectral Mixture Analysis Using Endmember Average RMSE, Remote Sensing of Environment, 87, 123 – 135.

Echtler, H., Segl, K., Dickerhof, C., Chabrilat, S., Kaufmann, H., (2003), Isograde Mapping and Mineral Identification on the Island of Naxos (Greece) Using DAIS 7915, Hyperspectral Data, Proceedings of SPIE, Algorithms and Technologies for Multispectral, Hyperspectral, and Ultraspectral Imagery IX., vol. 5093, 440 – 451.

ENVI Manual, (2005), Flash Module User's Guide, Research Systems Inc.

ENVI User's Guide (2001), Research Systems Inc., 948p.

Farrand, W.H. and Harsanyi, J.C., (1997), Mapping the distribution of mine tailings in the Coeur d'Alene River valley, Idaho, through the use of a Constrained Energy Minimization Technique, Remote Sensing of Environment, 59, 64–76.

Farrell, M. D., (2005), On the Impact of PCA Dimension Reduction for Hyperspectral Detection of Difficult Targets, *IEEE Geoscience and Remote Sensing Letters*, 2(2), 192 – 195.

Felde, G. W., Anderson, G. P., Cooley, T. W., Matthew, M. W., Adler-Golden, S. M., Berk, A., and Lee, J., (2003), Analysis of Hyperion Data with the FLAASH Atmospheric Correction Algorithm, *IEEE Transactions on Geoscience and Remote Sensing*, 90 – 92.

Glenn, N. F., Mundt, J. T., Weber, K., T., Prather, T. S., Lass, L. W., and Pettingill, J., (2005), Hyperspectral Data Processing for Repeat Detection of Small Infestations of Leafy Spurge, *Remote Sensing of Environment*, 95, 399 – 412.

Goetz, A., Ferri, M., Kindel, B., and Qu, Z., (2002), Atmospheric Correction of Hyperion Data and Techniques for Dynamic Scene Correction, *IEEE*, 1408 – 1410.

Goodenough, D. G., Dyk, A., Niemann, K. O., Pearlman, J. S., Chen, H., Murdoch, M., and West, C., (2003), Processing Hyperion and ALI for Forest Classification, *IEEE Transactions on Geoscience and Remote Sensing*, 41 (6), 1321 – 1331.

Green, A. A., Berman, M., Switzer, P., and Craig, M. D., (1988), A Transformation for Ordering Multispectral Data in Terms of Image Quality with Implications for Noise Removal, *IEEE Transactions on Geoscience and Remote Sensing*, 26 (1), 65 – 74.

Green, A. A. and Craig, M. D., (1985), Analysis of Aircraft Spectrometer Data With Logarithmic Residuals, Proceedings of the Airborne Imaging Spectrometer Data Analysis Workshop, JPL Publ. 85 – 41, Jet Propulsion Laboratory, California Institute of Technology, Pasadena, California, 111 – 119.

Grima, A. M., (2000)., Neuro-Fuzzy Modeling in Engineering Geology. A.A. Balkema, Rotterdam. 244 pp.

Haboudane, D., Bonn, F., Royer, A., Sommer, S., and Mehl, W., (2002). Land degradation and erosion risk mapping by fusion of spectrally-based information and digital geomorphometric attributes. *International Journal of Remote Sensing*, 23, 3795–3820.

Hubbard, B. E., Crowley, J. K., and Zimbelman, D. R., (2003), Comparative Alteration Mineral Mapping Using Visible to Shortwave Infrared (0.4-2.4 m) Hyperion, ALI, and ASTER Imagery, *IEEE Transactions on Geoscience and Remote Sensing*, 41 (6), 1401 – 1410.

Hutsinpillar, A., (1988), Discrimination of Hydrothermal Alteration Mineral Assemblages at Virginia City, Nevada, Using the Airborne Imaging Spectrometer, *Remote Sensing of Environment*, 24, 53 – 66.

Jensen, R. J., (1996), *Introductory Digital Image Processing, Second Edition*, Prentice-Hall, Inc., 152p.

Jensen, R. J., (2000), *Remote Sensing of the Environment: An Earth Resource Perspective*, Prentice-Hall, Inc., 544p.

Kameyama, S., Yamagata, Y., Nakamura, F., and Kaneko, M., (2001). Development of WTI and turbidity estimation model using SMA—application to Kushiro Mire, eastern Hokkaido, Japan. *Remote Sensing of Environment*, 77, 1–9.

Kara, H., 1991, 1:100 000 ölçekli Açın-sama Nitelikli Türkiye Jeoloji Haritaları Serisi No: 37, Kırşehir – G 18 Paftası, Maden Tetkik ve Arama Genel Müdürlüğü, Jeoloji Etütleri Dairesi, Ankara.

Keshava, N., (2003), Angle-Based Band Selection for Material Identification in Hyperspectral Processing, *Proceedings of SPIE, Algorithms and Technologies for Multispectral, Hyperspectral, and Ultraspectral Imagery IX.*, vol. 5093, 440 – 451.

Kruse, F. A., (1988), Use of Airborne Imaging Spectrometer Data to Map Minerals Associated with Hydrothermally Altered Rocks in the Northern Grapevine Mountains, Nevada and California, *Remote Sensing of Environment*, 24, 31 – 51.

Kruse, F. A., Kierein-Young, K. S., and Boardman, J. W., (1990), Mineral Mapping at Cuprite, Nevada with a 63-Channel Imaging Spectrometer, *Photogrammetric Engineering and Remote Sensing*, 56, No. 1, 83 – 92.

Kruse, F. A., Lefkoff, A. B., and Dietz, J. B., (1993.a.), Expert System-Based Mineral Mapping in Northern Death Valley, California/Nevada, Using the Airborne Visible/Infrared Imaging Spectrometer (AVIRIS), *Remote Sensing of Environment*, 44, 309 – 336.

Kruse, F. A., Lefkoff, A. B., Boardman, J. W., Heidebrecht, K. B., Shapiro, A. T., Barloon, P. J., and Goetz, A. F. H., (1993.b.), The Spectral Image Processing System (SIPS) – Interactive Visualization and Analysis of Imaging Spectrometer Data, *Remote Sensing of Environment*, 44, 145 – 163.

Kruse, F. A., Boardman, J. W., and Huntington, J. F., (2003), Comparison of Airborne Hyperspectral Data and EO-1 Hyperion for Mineral Mapping, *IEEE Transactions on Geoscience and Remote Sensing*, 41 (6), 1388 – 1400.

Kumar, S., Ghosh, J., and Crawford, M. M., (2001), Best-Bases Feature Extraction Algorithms for Classification of Hyperspectral Data, *IEEE Transactions on Geoscience and Remote Sensing*, 31(7), 1368 – 1379.

Lee, C. and Landgrebe, D.A., (1993), Analyzing High-Dimensional Multispectral Data, *IEEE Transactions on Geoscience and Remote Sensing*, 31, 792 – 800.

Liang, S., (2004), An Improved Atmospheric Correction Algorithm for Hyperspectral Remotely Sensed Imagery, *IEEE Geoscience and Remote Sensing Letters*, 1(2), 112 – 117.

Lillesand, T. M., and Kiefer, R. W., (2000), *Principal and Canonical Components, Remote Sensing and Image Interpretation, Fourth Edition*, John Wiley & Sons, Inc. 518p.

Marion, R., Michel, R., and Faye, C., (2006), Atmospheric Correction of Hyperspectral Data Over Dark Surface via Simulated Annealing, *IEEE Transactions on Geoscience and Remote Sensing*, 44(6), 1566 – 1574.

Mazer, A. S., Martin, M., Lee, M., and Solomon, J. E., (1988), Image Processing Software for Imaging Spectrometry Data Analysis, *Remote Sensing of Environment*, 24, 201 – 210.

Mustard, J. F., and Sunshine, J. M., (1999), Spectral Analysis for Earth Science: Investigations Using Remote Sensing Data (chapter 5), remote sensing for Earth Sciences: Manual of remote sensing, 3.ed., Vol. 3, edited by Andrew N. Rencz, 251 – 306.

Okada, K., & A. Iwashita, (1992) Hyper-multispectral image analysis based on waveform characteristics of spectral curve – *Adv. Space Res.* 12: 433–442.

PCI Geomatica Help, (2003), Using Atmospheric Correction, ATCOR 2 and ATCOR 3.

Pearlman, J., Segal, C., Liao, L., Carman, S., Folkman, M., Browne, B., Ong, L., and Ungar, S., (2000), Development and Operations of the EO-1 Hyperion Imaging Spectrometer, HYP.00.600.009.

Pieters, C. M., and Mustard, J. F., (1988), Exploration of Crustal/Mantle Material for the Earth and Moon Using Reflectance Spectroscopy, *Remote Sensing of Environment*, 24, No. 1 – 3, 151 – 178.

Richter, R., (1996), Atmospheric Correction of DAIS Hyperspectral Image Data, *Computer and Geosciences*, Vol. 22, No. 7, 785 – 793.

Roberts, D. A., Yamaguchi, Y., and Lyon, R. J. P., (1985), Calibration of Airborne Imaging Spectrometer Data to Percent Reflectance Using Field spectral Measurements, the Nineteenth International Symposium on Remote Sensing of Environment, Michigan, October 21 - 25, Ann Arbor, U.S.A., 679 – 688..

Robila, S. A., (2005), Using Spectral Distance for Speedup in Hyperspectra Image Processing, International Journal of Remote Sensing, 26 (24), 5629 – 5650.

Rowan, L. and Mars, J., (2002), Lithological mapping in the Mountain Pass, California area using Advanced Spaceborne Thermal Emission and Reflection Radiometer (ASTER) data. Remote Sensing of Environment, 84, 350-366.

Sabins, Floyd, F., 1997, "Remote Sensing: Principles and Interpretation", W. H. Freeman and Company, New York.

San, B. T., Sumer E. O., and Gurcay B., (2004), Comparison of Band Ratioing and Spectral Indices Methods for detecting Alunite and Kaolinite Minerals Using Aster Data in Biga Region, Turkey, XXth ISPRS Congress, 12-23 July 2004 Istanbul, Turkey, Commission 7, 77 - 82.

San, B. T. and Suzen, M. L., (2007), Comparison of Atmospheric Correction Techniques for Hyperion Data, ISPRS COMMISSION VII, WG2 & WG7, Conference on Information Extraction from SAR and Optical Data, with Emphasis on Developing Countries, Technical Session II: Optical Remote Sensing: High Resolution and Hyperspectral, 16 - 18 May 2007, ITU, Istanbul.

Sanders, L. C., Schott, J. R., Raqueno, R., (2001), A VNIR/SWIR Atmospheric Correction Algorithm for Hyperspectral Imagery with adjacent effect, *Remote Sensing of Environment*, 78, 252 – 263.

Simon, K., and Beckman, T., (2006), Hyperion Level 1G (L1GST) Product Output Files Data Format Control Book (DFCB), Earth Observing-1 (EO-1), version 1.0, USGS Center for Earth Resource Observation and Science (EROS), Sioux Falls, South Dakota.

Sohn, Y. and Rebello, N. S., (2002), Supervised and Unsupervised Spectral Angle Classifiers, *Photogrammetric Engineering and Remote Sensing*, 68 (12), 1271 – 1280.

Staenz, K., Secker, J., Gao, B. C., Davis, C., Nadeau, C., (2002), Radiative Transfer Codes Applied to Hyperspectral Data for the Retrieval of Surface Reflectance, *ISPRS Journal of Photogrammetry and Remote Sensing*, 57, 194 – 203.

Tutmez, B., Hatipoğlu, Z., Kaymak, U., (2006), Modelling electrical conductivity of groundwater using an adaptive neuro-fuzzy inference system, *Computers and Geosciences*, 32, 421 – 433.

URL1, USGS web site for Hyperion Data Product, June 2006, http://eo1.usgs.gov/Hyperion_Spectral_Coverage.htm.

Van Der Meer, F. (1999), Imaging Spectrometry for Geological Remote Sensing, *Geologie en Mijnbouw*, 77, 137 – 151.

Van Der Meer, F. (2001), Short Technical Note, Spectral matching using pixel cross-correlograms for the analysis of LANDSAT TM data, JAG 3 (2), 197 – 202.

Van Der Meer, F. (2004), Analysis of spectral absorption features in hyperspectral imagery, International Journal of Applied Earth Observation and Geoinformation 5, 55 – 68.

Van der Meer, F. and Bakker, W., (1997), CCSM: Cross Correlogram Spectral Matching – International Journal of Remote Sensing, 18, 1197–1201.

Van Der Meer, F. and De Jong, S.M. (2001), Imaging Spectrometry: Basic Principles and Prospective Applications, Kluwer Academic Publishers, 403p.

Vane, G., Goetz, A.F.H., (1988), Terrestrial Imaging Spectroscopy, Remote Sensing of Environment, 24, 1 – 29.

Yesilnacar, E. and Suzen, M. L., 2006, A Land-Cover Classification For Landslide Susceptibility Mapping By Using Feature Components, International Journal of Remote Sensing, Vol:27 (2), 253-275.

Yu, X., Reed, I., S., and Stocker, A. D., (1993), Comparative Performance Analysis of Adaptive Multispectral Detectors, IEEE Transactions on Geoscience and Remote Sensing, 41 (8), 2639 – 2656.

APPENDIX A

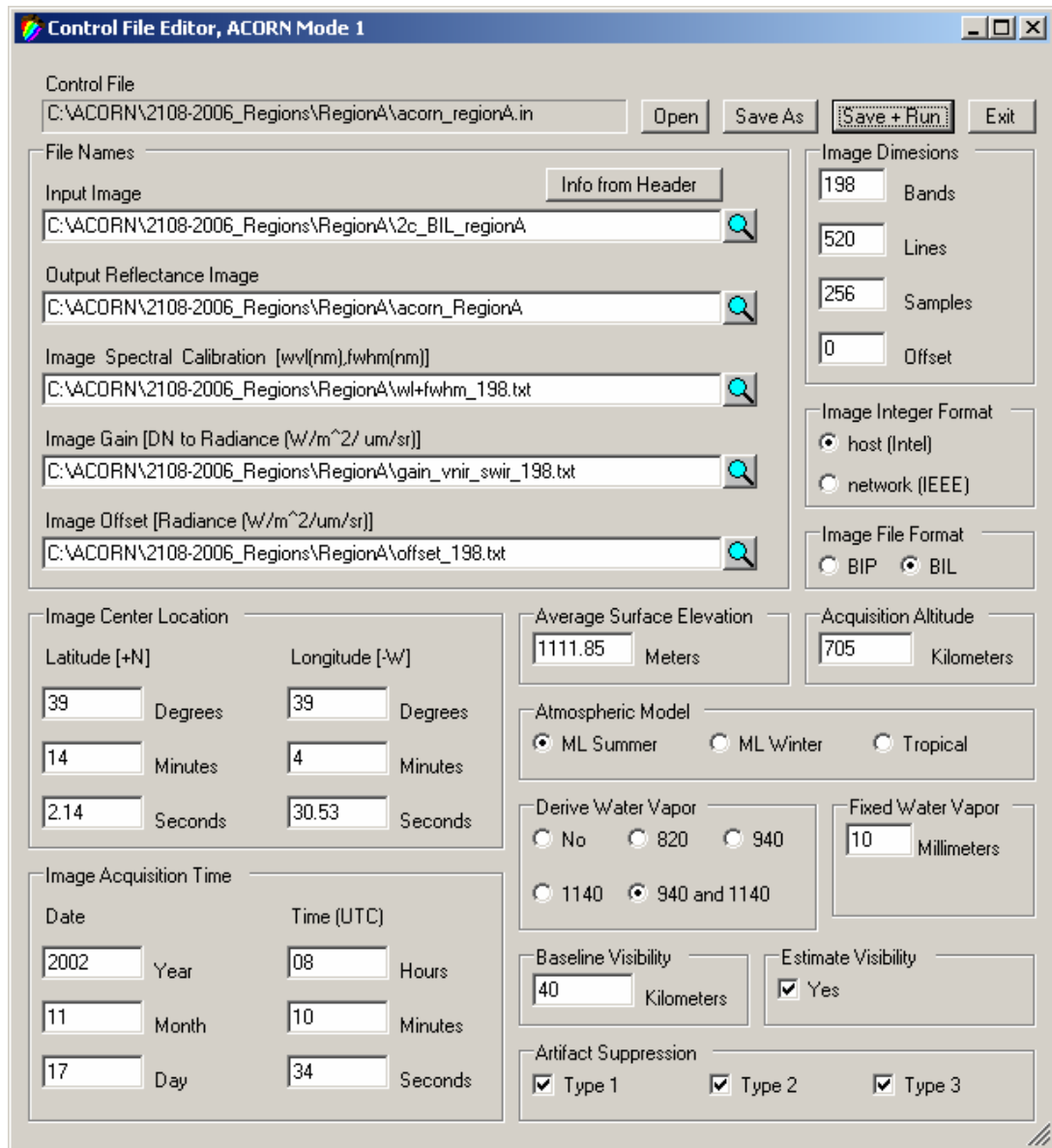


Figure A.1. ACORN software interface and input parameters for Ekecek Study Area

APPENDIX B

The screenshot displays the 'Atmospheric Correction Configuration' dialog box with the following settings:

- Input:** Image file: C:\NSPRS-2007-paper\Raw_Data_Geo.pix
- Elevation Information Setup:**
 - Constant(ATCOR2) is selected.
 - Height: 1.1
 - File: (empty)
 - Layer: (empty)
 - Units: Kilometers
- Sensor Information:**
 - Sensor type: HYPERION
 - Pixel size: 30.00000 m
 - Date: November 17, 2002
 - Calibration file: C:\NSPRS-2007-paper\hyperion196.cal
- Atmospheric Information:**
 - Atmospheric definition area: Rural
 - Condition: Mid-Latitude winter
 - Thermal atmospheric definition: Std
- Correction Parameter:**
 - Solar zenith: 60.669262 dec deg
 - Solar azimuth: 158.50863 dec deg
 - Visibility: 40.0 kilometers
 - Adjacency: 1.0 kilometers
 - Offset to surface temperature: 0.0 Kelvin

Buttons at the bottom include a help icon, OK, Cancel, and Apply.

Figure B.1. ATCOR2 software interface and input parameters for Ekecek Study Area

APPENDIX C

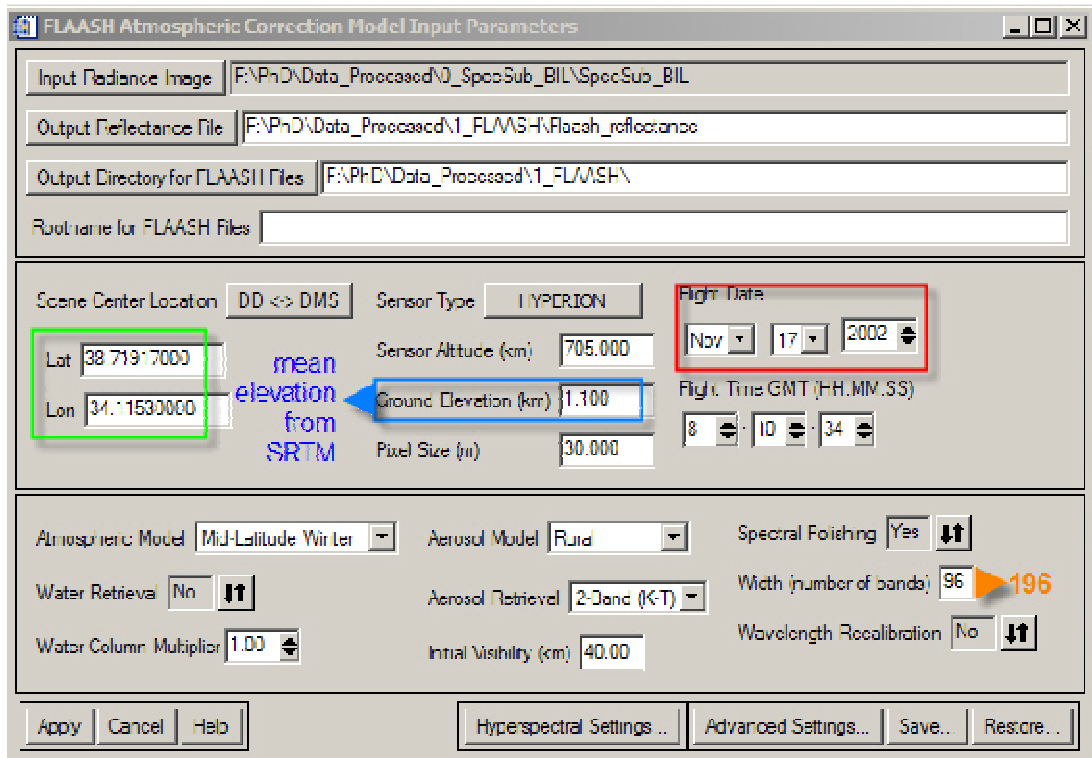


Figure C.1. FLAASH software interface and input parameters for Ekecek Study Area

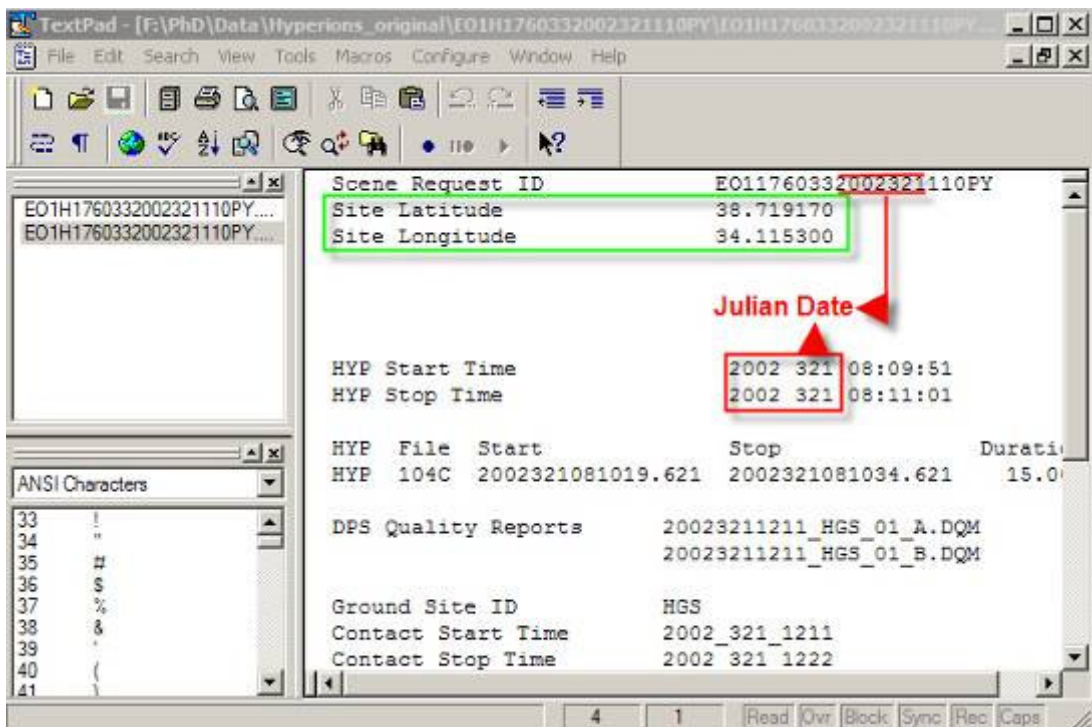


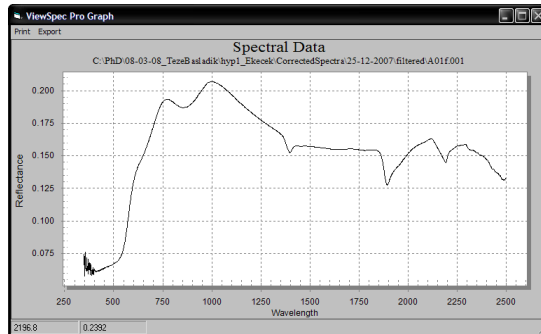
Figure C.2. Acquired header information from Hyperion data

APPENDIX D

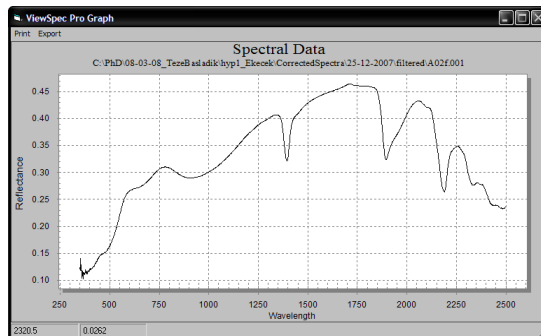
Sample No.
A1



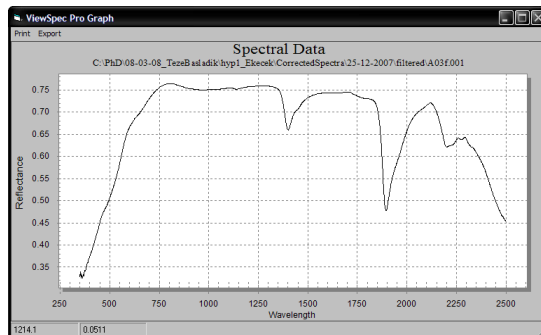
Spectral Signature



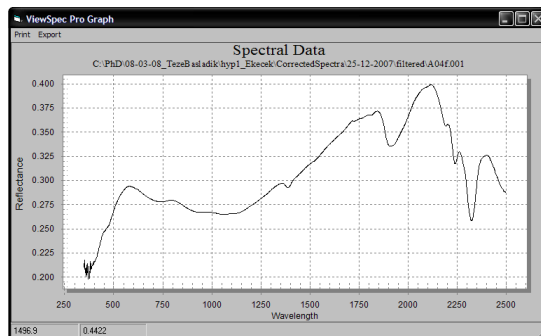
A3



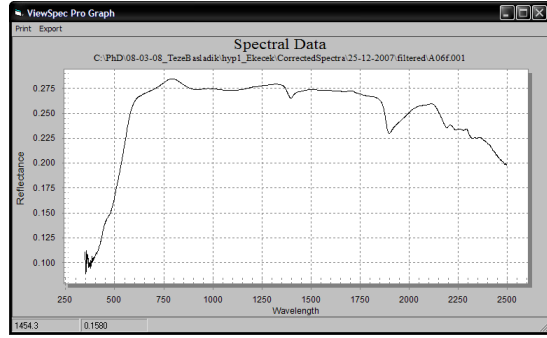
A3



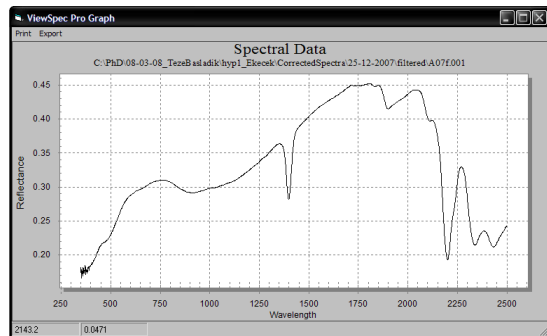
A4



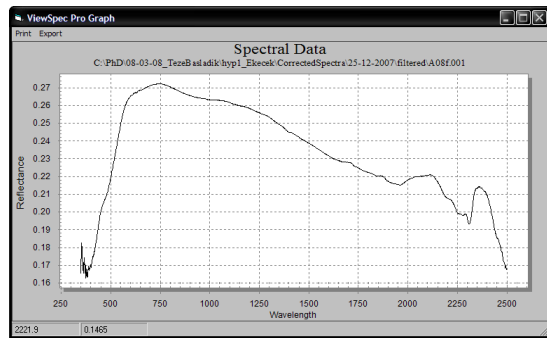
A6



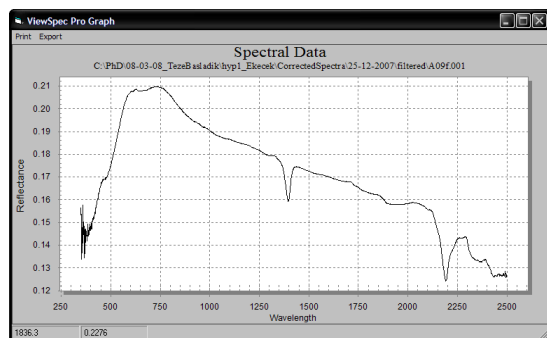
A7



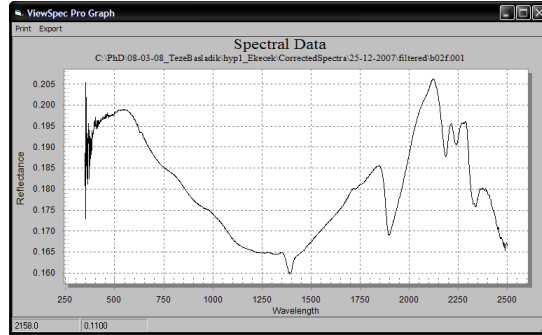
A8



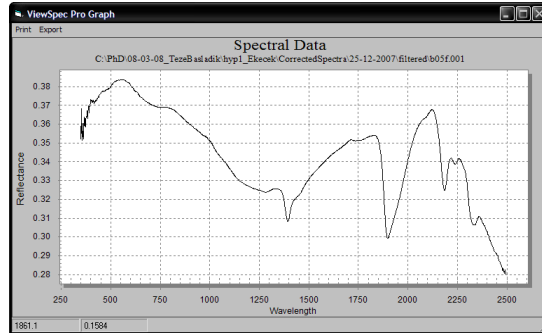
A9



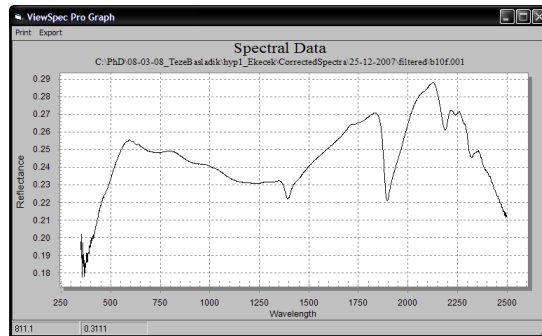
B02



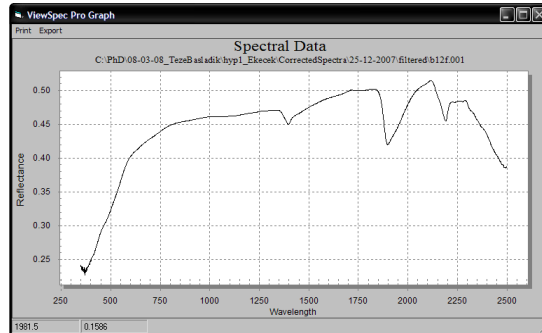
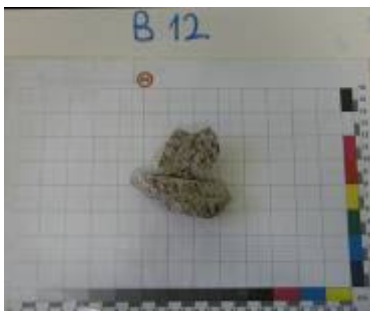
B05



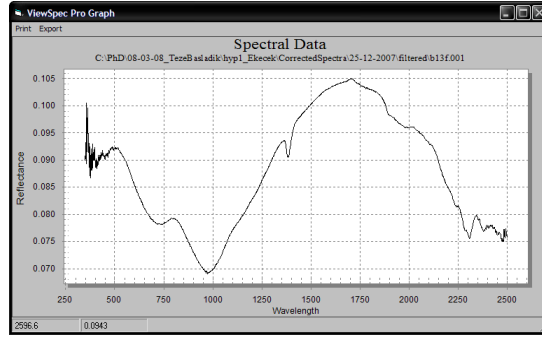
B10



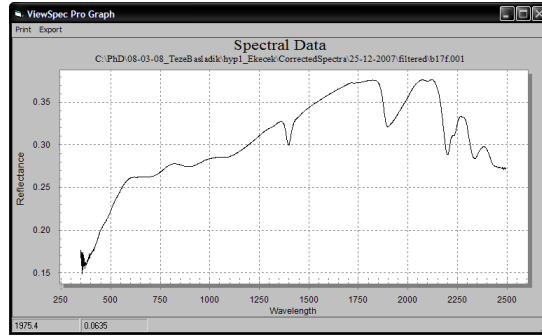
B12



B13



B17



B20

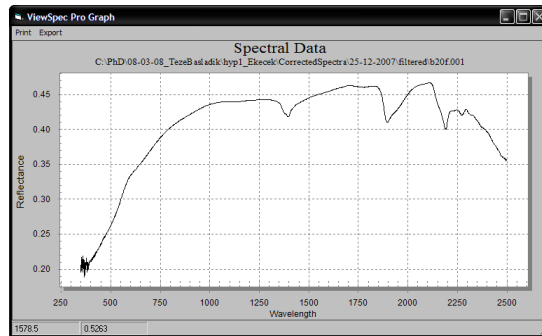


Figure D.1. Samples A and B are collected from Ekecek and Biga test sites, respectively

APPENDIX E

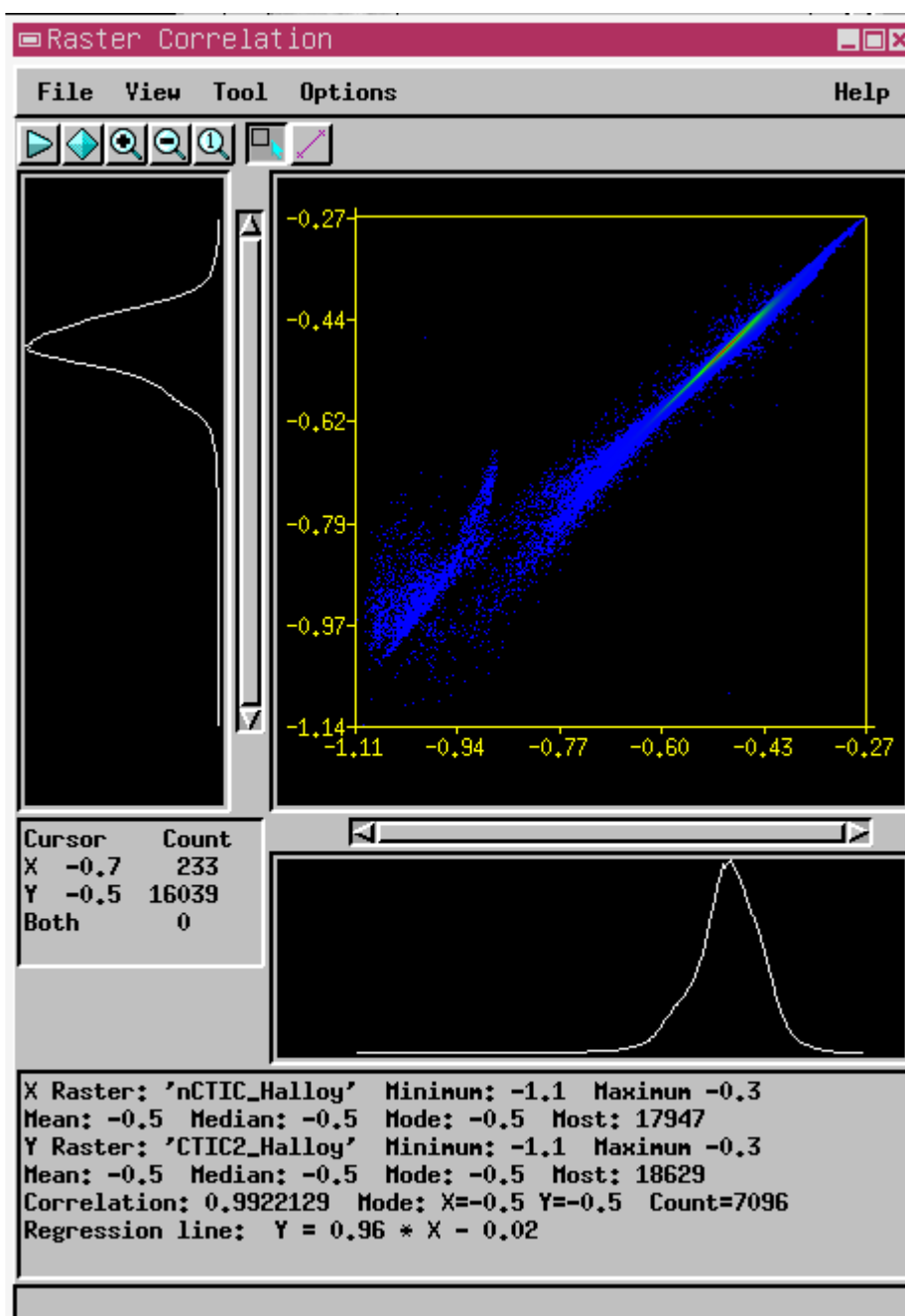


Figure E.1. Cross correlation between rule image of no CTIC and rule image of second order CTIC applied data for Halloysite mineral form USGS spectral library.

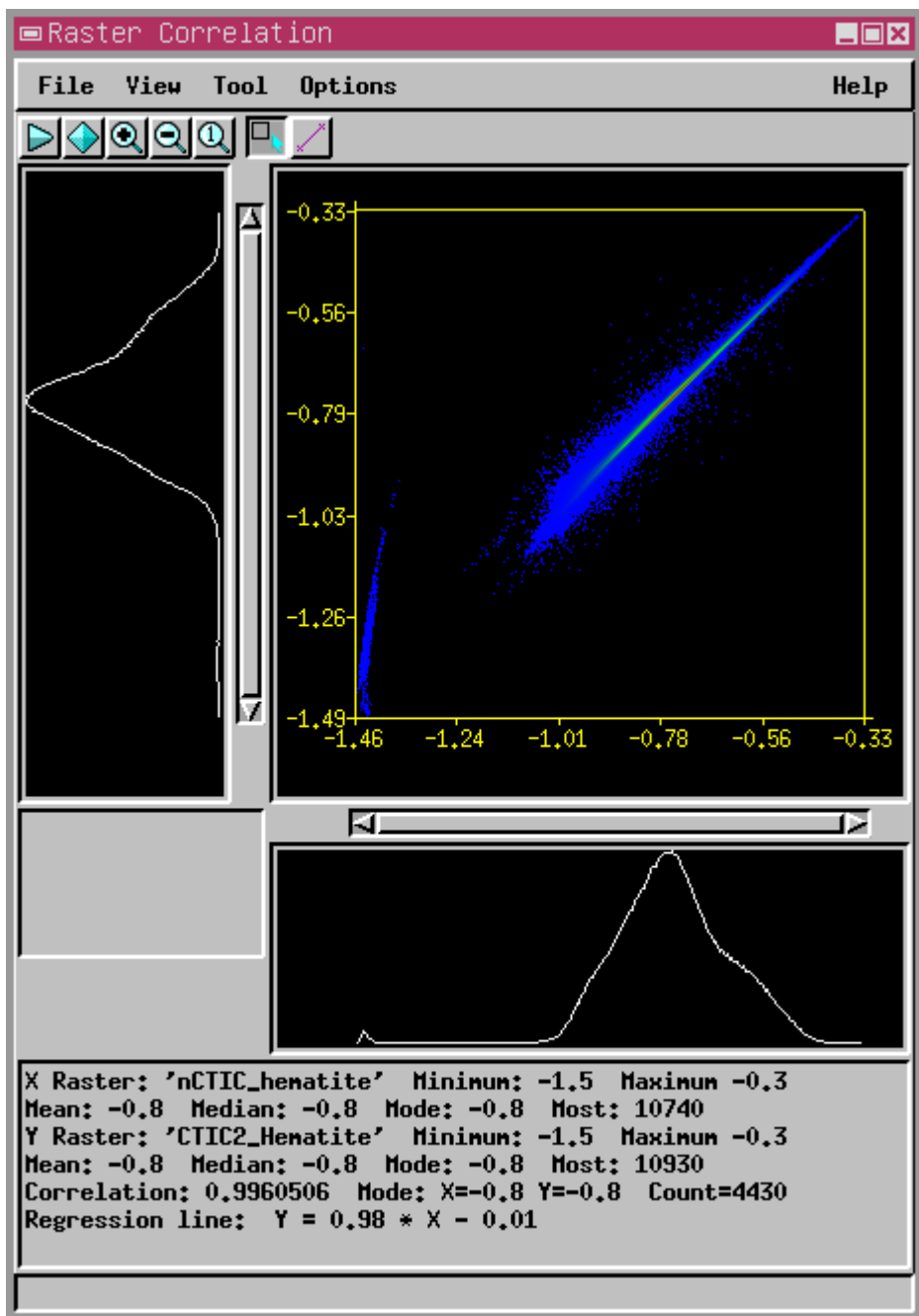


Figure E.2. Cross correlation between rule image of no CTIC and rule image of second order CTIC applied data for Hematite mineral form USGS spectral library.

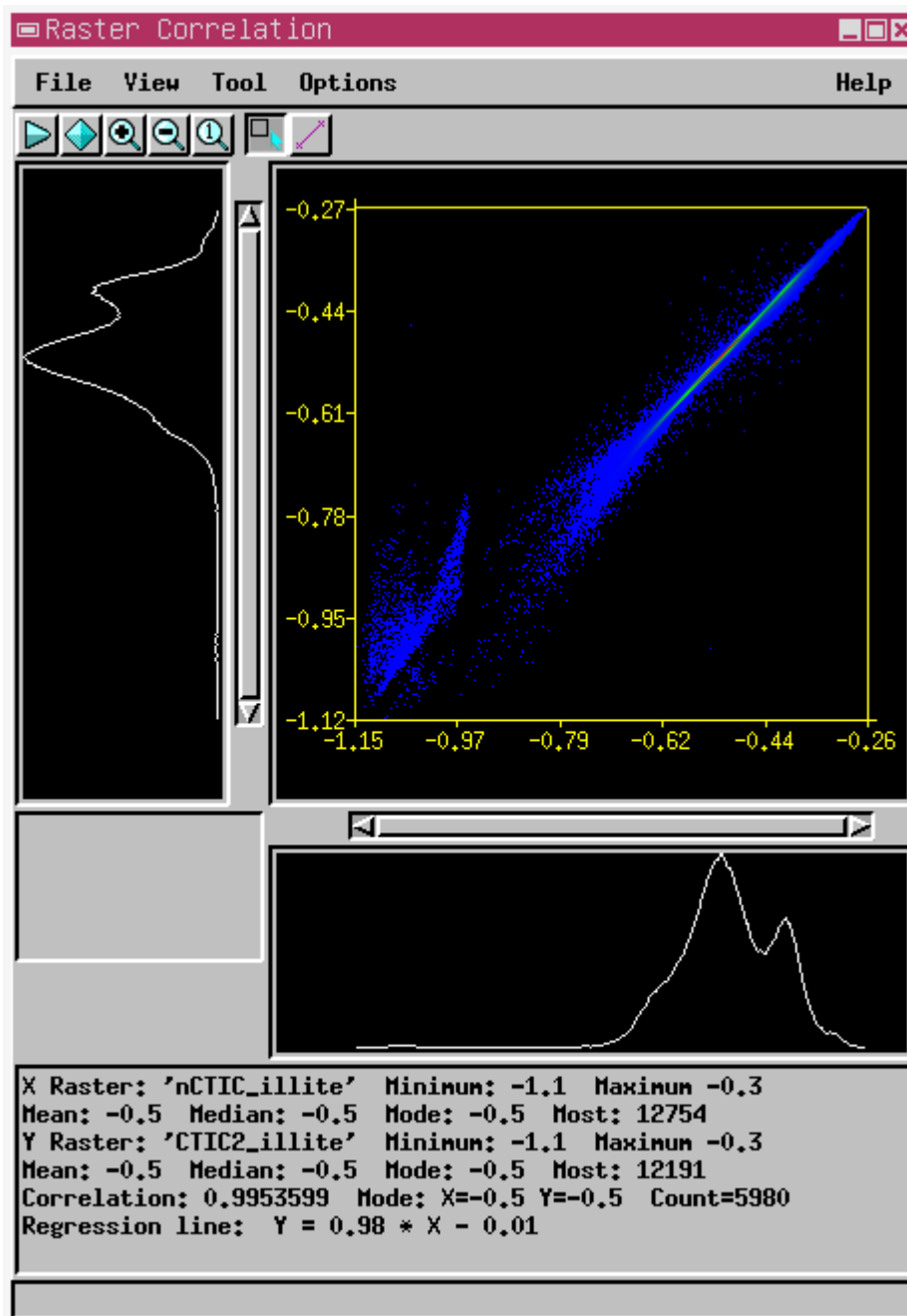


Figure E.3. Cross correlation between rule image of no CTIC and rule image of second order CTIC applied data for Illite mineral form USGS spectral library.

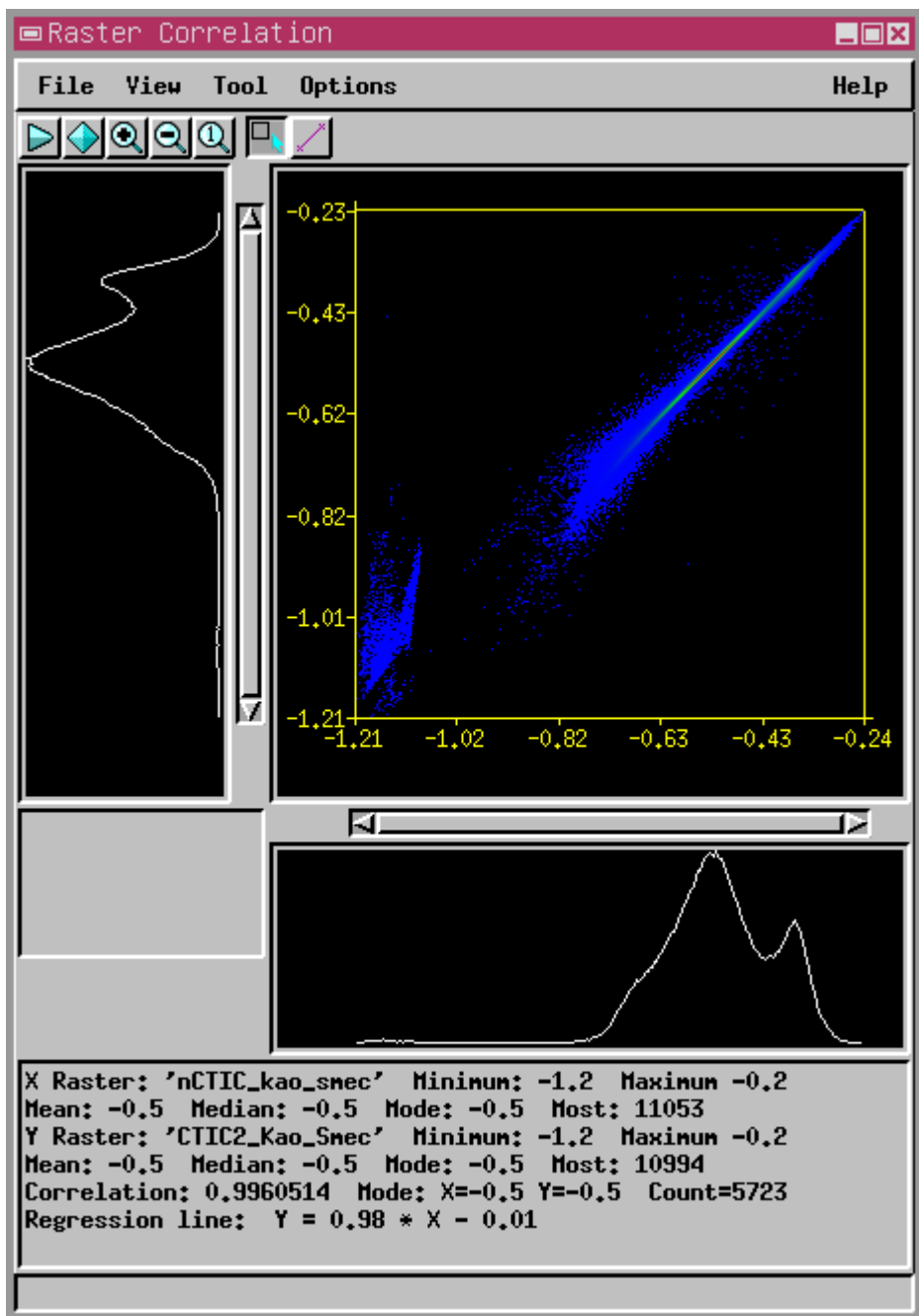


Figure E.4. Cross correlation between rule image of no CTIC and rule image of second order CTIC applied data for Kaolinite + Smectite mineral form USGS spectral library.

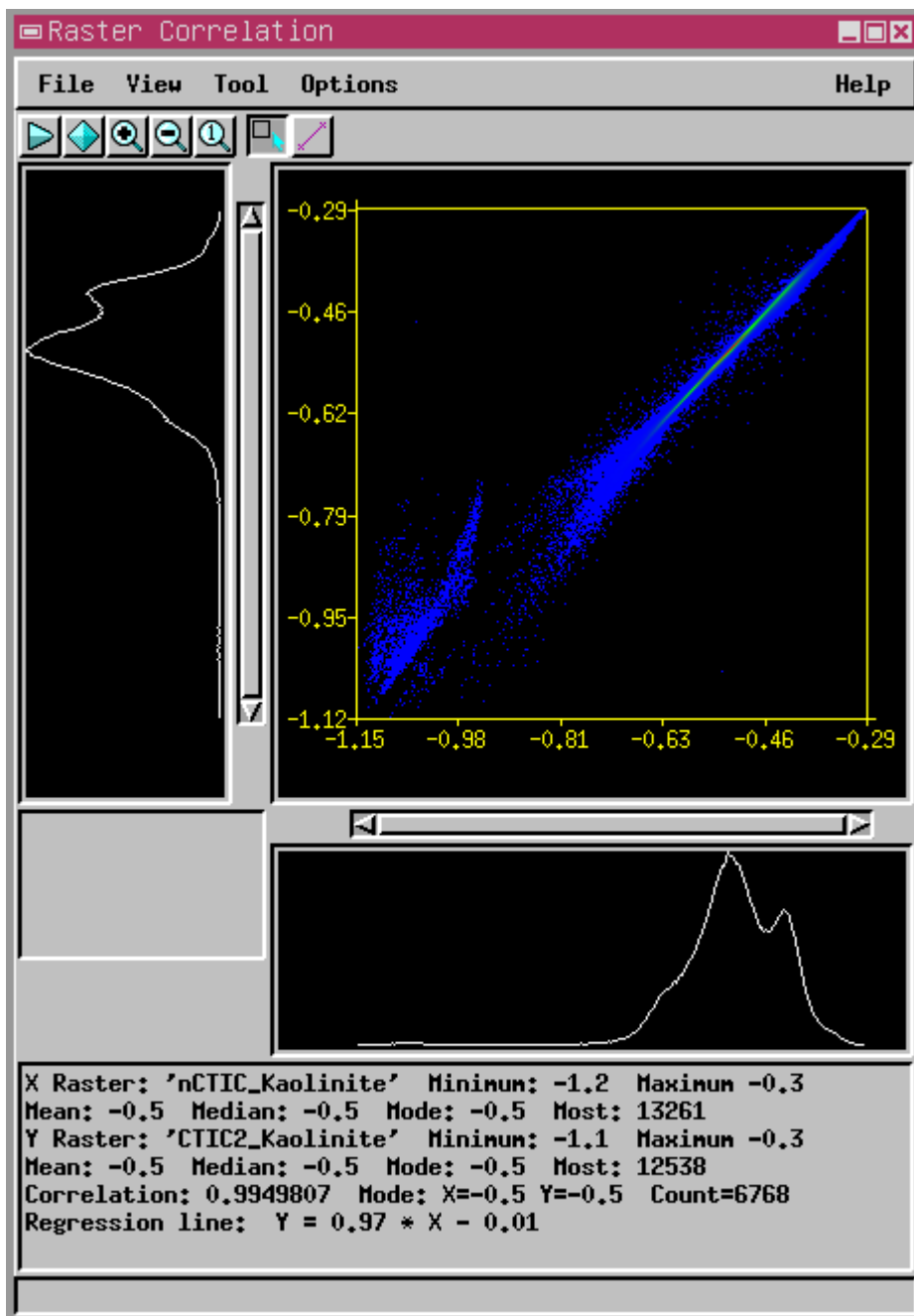


Figure E.5. Cross correlation between rule image of no CTIC and rule image of second order CTIC applied data for Kaolinite mineral form USGS spectral library.

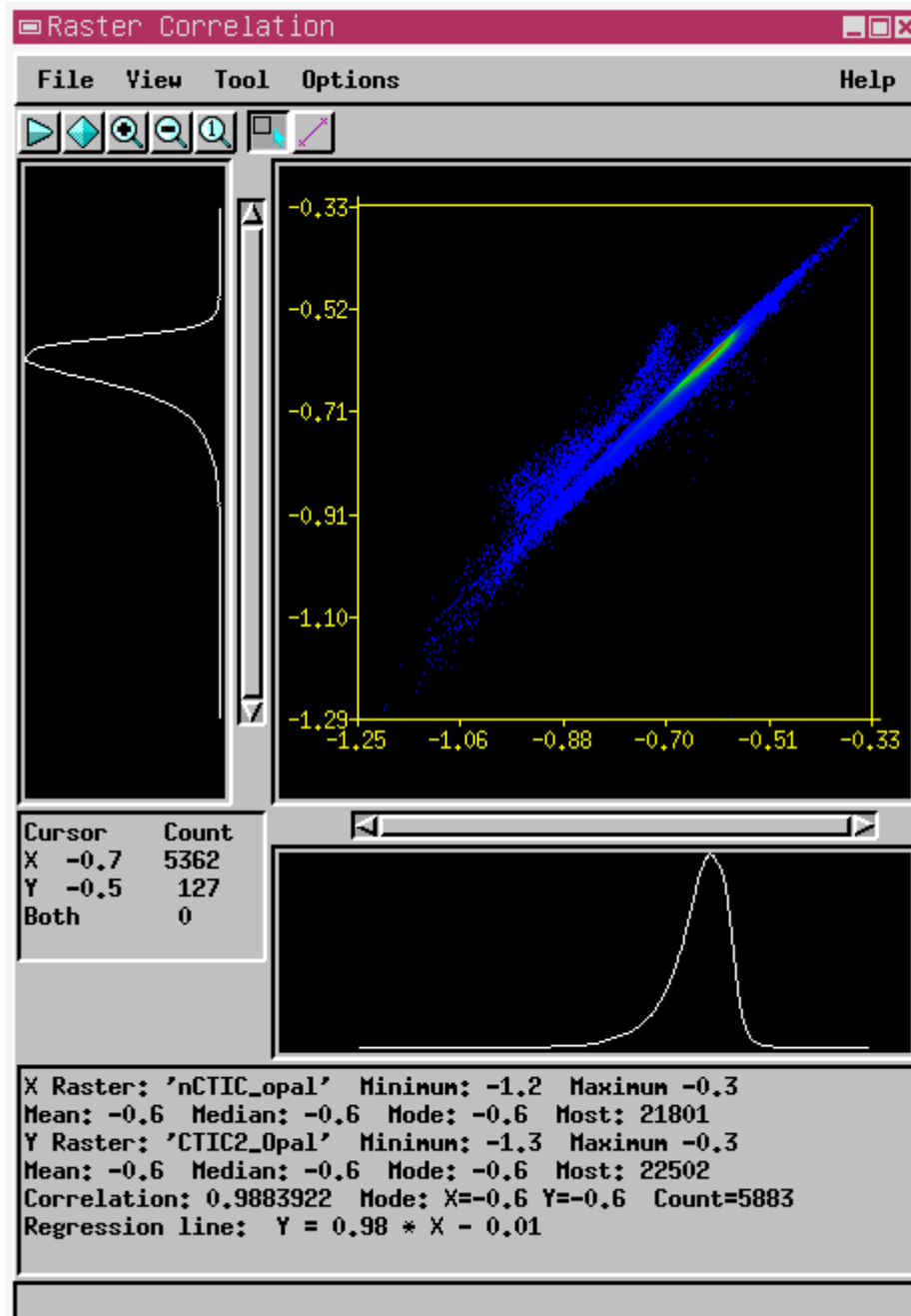


Figure E.6. Cross correlation between rule image of no CTIC and rule image of second order CTIC applied data for Opal mineral form USGS spectral library.

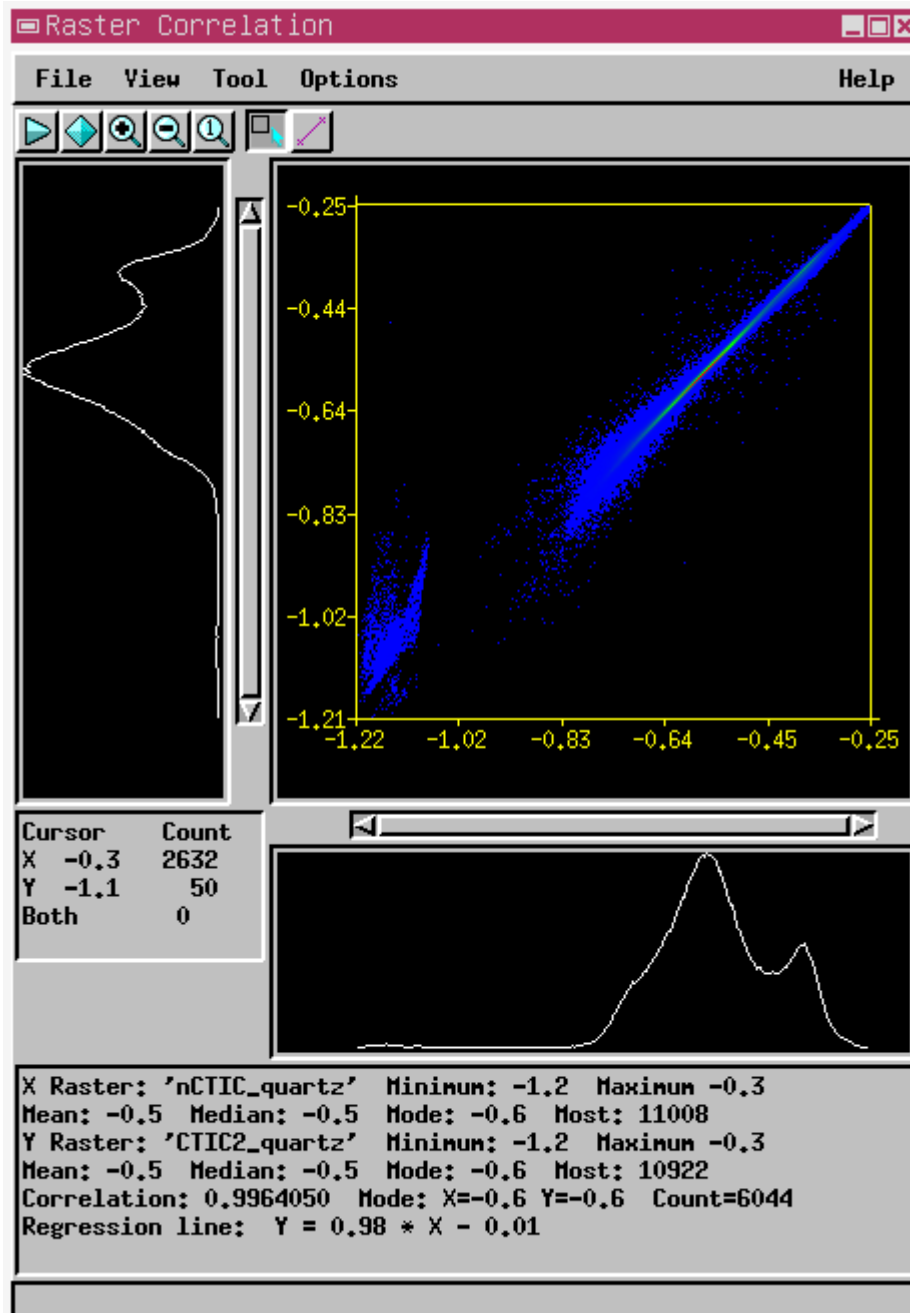


Figure E.7. Cross correlation between rule image of no CTIC and rule image of second order CTIC applied data for Quartz mineral form USGS spectral library.

APPENDIX F

Table F.1. Used Minerals Spectra from USGS Spectral Library
(<http://speclab.cr.usgs.gov/spectral.lib04/spectral-lib.desc+plots.html>)

Mineral Name in Spectral Library	Descriptions	
Albite 2	Title Sample ID Mineral Formula Collection Location Sample Description	Albite HS324 Plagioclase DESCRIPT HS324 Albite (Plagioclase, Na end member)(Feldspar group) NaAlSi3O8 South Dakota This is the sodium end member of the albite-anorthite series and is composed of 90 to 100% albite. Its spectrum shows weak features near 0.65 μ (very broad) and near 1.0 μ , suggesting the presense of small amounts of both Fe ⁺³ and Fe ⁺² . The Fe ⁺³ substitutes for aluminum, and the Fe ⁺² substitutes for the calcium, the latter in whatever anorthite is present. Hydroxyl and water bands are seen near 1.4 and 1.9 μ , and the AlOH bend OH combination feature near 2.2 μ is evident. The strength of this last band suggests incipient alteration of the sample, which is not apparent in hand specimen.
Halloysite 1	Title Sample ID Mineral Formula Collection Location Sample Description	Halloysite NMNH106236 DESCRIPT NMNH106236 Halloysite (Kaolinite-Serpentine group) Al2Si2O5(OH)4 Utah (probably Eureka) Polymorphous with Dickite, Kaolinite, and Nacrite.
Halloysite 3	Title Sample ID Mineral Formula Collection Location Sample Description	Halloysite CM13 DESCRIPT CM13 Halloysite (Kaolinite-Serpentine group) Al2Si2O5(OH)4 Dragon Iron Mine, Eureka, Utah Polymorphous with Dickite, Kaolinite, and Nacrite.
Halloysite 4	Title Sample ID Mineral Formula Collection Location Sample Description	Halloysite K LH503 DESCRIPT K LH503 Halloysite (Kaolinite-Serpentine group) Al2Si2O5(OH)4 Tintic, UT Polymorphous with Dickite, Kaolinite, and Nacrite.
Halloysite 5	Title Sample ID Mineral Formula Collection Location Sample Description	Halloysite+Kaolinite CM29 DESCRIPT CM29 Halloysite + Kaolinite (Kaolinite-Serpentine group) Al2Si2O5(OH)4 Wagon Wheel Gap, Colorado Polymorphous with Dickite, Kaolinite, and Nacrite.
Hematite 1	Title Sample ID Mineral Formula	Hematite=2%+98%Qtz GDS76 GDS76 Hematite (2%) + Quartz (98%) (Hematite group) alpha-Fe2O3 + SiO2

	Collection Location	Laboratory mixture
	Sample Description	Hematite GDS27 2 wt% + 98 wt% Pure crystal quartz (<250 µm grain sizes)
Illite 4	Title	Illite IL101 DESCRIPT
	Sample ID	IL101
	Mineral	Illite, a group of hydrated mica-clay minerals
	Formula	(K,H3O)(Al,Mg,Fe)2(Si,Al)4O10[(OH)2,H2O]
	Collection Location	Shakanai Mine, Akita Prefecture, Japan
	Sample Description	-
Illite 5	Title	Illite IL105 DESCRIPT
	Sample ID	IL105
	Mineral	Illite, a group of hydrated mica-clay minerals
	Formula	(K,H3O)(Al,Mg,Fe)2(Si,Al)4O10[(OH)2,H2O]
	Collection Location	Fithian, IL
	Sample Description	-
Kaolinite 4	Title	Kaolinite KL502 DESCRIPT
	Sample ID	KL502
	Mineral	Kaolinite (Kaolinite-Serpentine group)
	Formula	Al2Si2O5(OH)4
	Collection Location	Cripple Creek, CO
	Sample Description	-
Kaolinite 6	Title	Kaolinite CM3 DESCRIPT
	Sample ID	CM3
	Mineral	Kaolinite (Kaolinite-Serpentine group)
	Formula	Al2Si2O5(OH)4
	Collection Location	Macon, GA
	Sample Description	Polymorphous with Dickite, Halloysite, and Nacrite.
Montmorillonite 2	Title	Montmorillonite SAz-1 DESCRIPT
	Sample ID	SAz-1
	Mineral	Montmorillonite (Montmorillonite group)
	Formula	(Na,Ca)0.33(Al,Mg)2Si4O10(OH)2*nH2O
	Collection Location	Apache County, Arizona
	Sample Description	it was spectrally pure
Muscovite 4	Title	Muscovite GDS113 DESCRIPT
	Sample ID	GDS113
	Mineral	Muscovite (Mica group)
	Formula	KAl2Si3O10(OH)2
	Collection Location	Brazil
	Sample Description	-
Oligoclase 2	Title	Orthoclase NMNH142137 DESCRIPT
	Sample ID	NMNH142137
	Mineral	Orthoclase (Ferrian) (Feldspar group)
	Formula	KAlSi3O8
	Collection Location	Unknown
	Sample Description	Forms series with celsian. Dimorphous with Microcline. Ferrian orthoclase.
Kaolinite+Smectite 5	Title	Kaolin/Smectite KLF511 DESCRIPT
	Sample ID	KLF511
	Mineral	Kaolinite/Smectite (12% Kaol.) (Montmorillonite group)
	Formula	Al2Si2O5(OH)4 + (Na,Ca)0.33(Al,Mg)2Si4O10*nH2O
	Collection Location	Paris Basin, France
	Sample Description	Kaolinite/smectite clays are produced as transitional phases as smectite weathers to kaolinite. This sample is from the Argiles Plastique Formation of the Paris Basin. This formation contains a paragenetic sequence from smectite to kaolinite.
Opal 2	Title	Opal (Hyalite) TM8896 DESCRIPT
	Sample ID	TM8896
	Mineral	Opal

	Formula	SiO ₂ *nH ₂ O
	Collection Location	Beaver Co., UT.
	Sample	-
Quartz 2	Title	Quartz GDS31 DESCRIPT
	Sample ID	GDS31
	Mineral	Quartz
	Formula	SiO ₂
	Collection Location	Brazil
	Sample Description	Polymorphous with Tridymite, Cristobalite, Coesite and Stishovite. Quartz (SiO ₂) is an important constituent of igneous rocks which have an excess of silica, such as granite, rhyolite or pegmatite. Because it is extremely resistant to both mechanical and chemical attack, it usually survives the weathering process. Quartz is an extremely difficult mineral to grind without contamination, because of its hardness. "Results of petrographic examination: Hand sample appears entirely pure, being a clear and transparent fragment of a single crystal. Under petrographic microscope, sample also pure and clear."

VITA

Bekir Taner SAN

Date and Place of Birth: 1975, Ankara
Marital Status: Married
e-mail: tanersan@gmail.com

EDUCATION

Degree	Institution	Year of Graduation
PhD	METU, Geological Engineering	2008
MS	METU, Geodetic and Geographical Information Technologies	2002
BS	METU, Geological Engineering	1998
Technical High School	Yenimahalle Teknik Lisesi, Electronic Dept.	1993

WORK EXPERIENCE

Year	Place	Enrollment
2005 – Present	General Directorate of Mineral Research and Exploration (MTA), Remote Sensing and GIS Div.	Coordinator
2000 – 2005	General Directorate of Mineral Research and Exploration (MTA), Remote Sensing and GIS Div.	Geological Engineer

PUBLICATIONS

BOOKS

SUMER, E. Ö., **SAN, B. T.**, GURCAY, B., PEKESIN, F.B., AVCI, M. K., KORUYUCU, M., DAĞLIYAR, A., TEOMAN, S., TOPÇU, T., and ÖZGÜNER, C., (2006), Applications of ASTER Data; Examples From Turkey, MTA Special Publication Series-5, Ankara-2006, ISBN: 975-8964-41-0 , 71 p.

INTERNATIONAL JOURNALS

SAN, B. T. and SUZEN, M. L., (2005), "Digital elevation model (DEM) generation and accuracy assessment from ASTER stereo data", INT. J. REMOTE SENSING, VOL. 26, NO. 22, pp.5013 - 5027

TURKER, M. and **SAN, B. T.**, (2004), "Detection of collapsed buildings caused by the 1999 Izmit, Turkey earthquake through digital analysis of post-event aerial photographs", INT. J. REMOTE SENSING, VOL. 25, NO. 21, 4701 - 4714.

TURKER, M. and SAN, B. T., (2003), "SPOT HRV data analysis for detecting earthquake-induced changes in Izmit, Turkey", INT. J. REMOTE SENSING, VOL. 24, NO. 12, pp.2439 - 2450

INTERNATIONAL PROCEEDINGS

MURAOKA, H., NEFESLIOGLU, H. A., **SAN, B. T.**, and ARAKI, T., (2006) , " Applying data mining method for detecting landslide susceptible area by using ASTER (2) ", The 40th Conference of the Remote Sensing Society of Japan, May 18 - 19, 2006, Chiba University of Science, Chiba, Japan, pp. 169 - 170.

MURAOKA, H., MIURA, H., NEFESLIOGLU, H. A., **SAN, B. T.**, and ARAKI, T., (2005) , " Applying data mining method for detecting landslide susceptible area by using ASTER ", The 38th Conference of the

Remote Sensing Society of Japan, May 20, 2005, Tokyo University of Science, Noda-City, Chiba, Japan

AVCI, K.M., ERKAL, T., and **SAN , B. T.**, (2004), "Practical Detection of Coastline Changes of Yeşilırmak Delta Using Remote Sensing and GIS Techniques, Northern Turkey", Proceedings of International Symposium on Earth System Sciences, Istanbul - Turkey, September, 8 - 10, 2004, pp. 363 - 370

SAN, B. T., SUMER, E. O., and GURCAY, B., (2004), "Comparison of Band Ratioing and Spectral Indices Methods for detecting Alunite and Kaolinite Minerals Using Aster Data in Biga Region, Turkey", XXth ISPRS Congress, 12-23 July 2004 Istanbul, Turkey, Commission 7, pp. 77 - 82.

SAN, B. T. and TURKER, M., (2002), "Earthquake Damage Assessment of Buildings from Aerial Photographs" Proceedings of the 3rd International Symposium Remote Sensing of Urban Areas, Vol. 2, Istanbul, June 11-13, pp. 633 - 640

TURKER, M. and **SAN, B. T.**, (2002), "Multi-Level Analysis of Space and Aerial Images for Detecting Earthquake Induced Changes in Golcuk, Turkey" Proceedings of the International Symposium on GIS, Istanbul, Turkey, September 23 - 26.

NATIONAL PROCEEDINGS

SAN, B. T., NEFESLİOĞLU, H. A., DUMAN, T. Y., and MURAOKA, H., (2008), Güneydoğu Marmara Bölgesi, 1:100.000 Ölçekli Heyelan Duyarlılık Haritaları, I.Ulusal Jeolojik Uzaktan Algılama Sempozyumu (First National Geologic Remote Sensing Symposium of Turkey), p 15 – 16, 22 - 23 Mayıs 2008, Cumhuriyet Üniversitesi, Jeoloji Mühendisliği Bölümü, SİVAS.

SAN, B. T. and SUZEN, M. L., (2008), Hyperion görüntülerinde CTIC (Uçuş Yönüne Dik Aydınlanma Düzeltmesi) tespit edilmesi ve değerlendirmesi, I.Ulusal Jeolojik Uzaktan Algılama Sempozyumu (First National Geologic Remote Sensing Symposium of Turkey), p 17 – 18, 22 - 23 Mayıs 2008, Cumhuriyet Üniversitesi, Jeoloji Mühendisliği Bölümü, SİVAS.

NEFESLİOĞLU, H.A., **SAN, B. T.**, DUMAN T.Y., MURAOKA H., MIURA H., ARAKI, T., (2007). Uzaktan algılama verilerinin heyelan duyarlılık haritalarının üretilmesindeki kullanım potansiyeli: Kelemen ve Merer Havzaları. VI. Türkiye Kuvaterner Sempozyumu, Avrasya Yer Bilimleri Enstitüsü, ITU, İstanbul .

GURLER, G and **SAN, B. T.**, (2007), "Türkiye Jeoloji Bilgi Bankası", TMMOB Coğrafi Bilgi Sistemleri 2007 Kongresi, 30 Ekim - 02 Kasım 2007, KTÜ, Trabzon.

SAN, B. T., NEFESLİOĞLU, H. A. and DUMAN, T.Y., (2006), "The Use of ASTER L3A Data in Producing of Landslide Susceptibility Maps: Kelemen Catchment Area", Proceedings of The Symposium on Recent Applications in Engineering Geology, pp. 73-80, May 25-27,

2006, Denizli-Turkey, Edited by Kumsar H., Tasdelen, S. and Celik, S.B., Organized by Pamukkale Univ., Geological Eng. Dept., Int. Assoc. of Engineering Geology and Environment, Turkish National Comm., and Suleyman Demirel Univ. Geological Eng. Dept.

SAN, B. T., (2006), "Application of Hyperspectral Satellite on Earth Sciences", invited papers, 59th Geological Congress of Turkey, March 20-24, 2006, UCTEA The Chamber of Geological Engineers of Turkey, pp.441 - 442.

SAN, B. T., NEFESLIOGLU, H. A. and SUZEN, M. L., (2006), "An approach to evaluate the accuracy of satellite derived digital elevation models (DEM) for environmental geoscience ", 59th Geological Congress of Turkey, March 20-24, 2006, UCTEA The Chamber of Geological Engineers of Turkey, pp.443 - 444.

SAN, B. T . , GÜRÇAY, O. B., KORUYUCU, M., PEKESİN, B. ve SÜMER, E. Ö., (2006), "Pınarbaşı, Bünyan, Akkışla Bölgesinin ASTER Uydu Verisi Yardımıyla Mineral Haritalaması", 30. Yıl Fikret Kutman Jeoloji Sempozyumu, 23 - 23 Eylül 2006, Selçuk Üniv., Konya

GURCAY, B., **SAN, B. T.**, SUMER, E. O., and KORUYUCU, M., **(2005)**, "Determining Alunite and Kaolinite Minerals with ASTER Data", 57th Geological Congress of Turkey, 11-17 April 2005, UCTEA The Chamber of Geological Engineers of Turkey, p.206.

SAN, B. T. and SUZEN, M. L., **(2005)**, "Accuracy Assessment of Digital Elevation Models Produced from ASTER Data", 57th Geological Congress of Turkey, 11-17 April 2005, UCTEA The Chamber of Geological Engineers, pp.212.

RESEARCH AND APPLICATION PROJECT REPORTS

Nefesliođlu, H.A., **SAN, B. T.**, Duman, T.Y., (2007). Uzaktan algılama verilerinin heyelan duyarlılık haritalarının üretilmesindeki kullanım potansiyeli: Kelemen ve Merer Havzaları. MTA, Geotechnos (Japonya) ve ERSDAC (Japonya) Ortaklığında Gerçekleştirilen Uluslararası Projeye İlişkin Final Raporu, Rapor No. 10896, 68 s.

SAN, B. T., Nefesliođlu, H.A., Duman, T.Y., Muraoka, H., (2008). Güney–Dođu Marmara bölgesinin heyelan duyarlılığı. MTA, Geotechnos (Japonya) ve ERSDAC (Japonya) Ortaklığında Gerçekleştirilen Uluslararası Projeye İlişkin Final Raporu, Rapor No. 11018, 69 s.

AVCI, K.M., ERKAL, T., and **SAN , B. T.**, (2003), "Yeşilirmak Deltası Kıyı Çizgisi Deđişiminin Uzaktan Algılama ve Cođrafi Bilgi Sistemleri Yöntemi ile incelenmesi", MTA Rapor, No: 10612, MTA Genel Müdürlüğü

THESIS

SAN, B. T., (2002), "Detecting Earthquake Induced Changes From Space and Aerial Images" Unpublished Copy of Master Thesis, METU, Department of Geodetic and Geographic information Technologies.